



Gisele Góes Cintra

**Local Buckling Behavior of Pultruded
Glass-Fiber Reinforced Polymer (pGFRP)
I-Section Columns**

Dissertação de Mestrado

Dissertation presented to the Programa de Pós-graduação em Engenharia Civil of PUC-Rio in partial fulfillment of the requirements for the degree of Mestre em Engenharia Civil.

Advisor: Prof. Daniel Carlos Taissum Cardoso

Co-advisor: Prof^a. Janine Domingos Vieira

Rio de Janeiro
August 2017



Gisele Góes Cintra

**Local Buckling Behavior of Pultruded
Glass-Fiber Reinforced Polymer (pGFRP) I-
Section Columns**

Dissertation presented to the Programa de Pós-graduação em Engenharia Civil of PUC-Rio in partial fulfillment of the requirements for the degree of Mestre em Engenharia Civil. Approved by the undersigned Examination Committee.

Prof. Daniel Carlos Taissum Cardoso

Advisor

Departamento de Engenharia Civil e Ambiental – PUC-Rio

Prof^a. Janine Domingos Vieira

Co-Advisor

Universidade Federal Fluminense

Prof. Flávio de Andrade Silva

Departamento de Engenharia Civil e Ambiental – PUC-Rio

Prof^a. Ana Maria Abreu Jorge Teixeira

Instituto Militar de Engenharia

Prof. Kent A. Harries

University of Pittsburgh

Prof. Márcio da Silveira Carvalho

Vice Dean of Graduate Studies

Centro Técnico Científico – PUC-Rio

Rio de Janeiro, August 11th, 2017

All rights reserved.

Gisele Góes Cintra

Bachelor in civil engineering at Universidade Federal Fluminense, in 2013. Worked with planning and management of projects, as well as retrofit and design of structures. Her area of interest encompasses the instability of structures and experimental researches.

Bibliographic data

Cintra, Gisele Góes

Local buckling behavior of pultruded Glass-Fiber Reinforced Polymer (pGFRP) I-Section columns / Gisele Góes Cintra ; advisor: Daniel Carlos Taissum Cardoso ; co-advisor: Janine Domingos Vieira. – 2017.

171 f. : il. color. ; 30 cm

Dissertação (mestrado)–Pontifícia Universidade Católica do Rio de Janeiro, Departamento de Engenharia Civil, 2017.

Inclui bibliografia

1. Engenharia civil – Teses. 2. Polímero reforçado com fibra de vidro (GFRP). 3. Flambagem local. 4. Colunas. 5. Condições de contorno. I. Cardoso, Daniel Carlos Taissum. II. Vieira, Janine Domingos. III. Pontifícia Universidade Católica do Rio de Janeiro. Departamento de Engenharia Civil. IV. Título.

CDD: 624

Acknowledgment

Above all, I thank God for guiding me and for helping me to never lose my faith.

To Pontifícia Universidade Católica do Rio de Janeiro, for the amazing opportunity of making part of its history.

To CAPES, for the financial support.

To all my professors of the Master's Program, for all the knowledge acquired over these two years.

To the best advisor I could ever have Prof. Daniel Cardoso. Thank you for the daily motivations, all your dedication and patience. And especially, for showing me how important it is to believe in myself.

To my co-advisor Prof^a Janine Vieira, with whom it was a pleasure to work. My sincere thanks for all your competence, motivation and patience in analyzing even the smallest details.

To the staff of the Structures and Material Laboratory (LEMDEC) of PUC-Rio. To Rogério, José Nilson, Carlos, Bruno, Patrícia and especially to the ones that have taught me everything they could: Euclides and Marques. You have made my days lighter and I could not have done it without you. Thank you so much, for everything. More than a team, you are my friends!

To my dear friends, who have walked along with me and who have sincerely wished me the best. I have no words to thank you for having made these two years easier and happier. And for helping me so many times with little things that made all the difference in the end. I will keep in my heart all the greatness of each one of you.

To the most wonderful family, for giving me all the support I need to accomplish anything in this life. Thank you for being unique and for always believing in me. Thank you for showing me the importance of studying more and more. To my uncles, aunts and cousins. To the best brothers and parents in the world. All I am, I owe it to you. Thank you for all.

And finally, a special thanks to the most incredible person I know: my mother, Corina. There will never be enough words to thank you for everything you have done for me. Even in face of all difficulties, you have continued to guide me and offer me everything you could. Thank you for teaching me to be a better person every day of my life. I love you.

Abstract

Cintra, Gisele Góes; Cardoso, Daniel Carlos Taissum (Advisor); Vieira, Janine Domingos (Co-Advisor). **Local Buckling Behavior of Pultruded Glass-Fiber Reinforced Polymer (pGFRP) I-Section Columns**. Rio de Janeiro, 2017. 171 p. Dissertação de Mestrado – Departamento de Engenharia Civil e Ambiental. Pontifícia Universidade Católica do Rio de Janeiro.

This work aims to investigate the performance of pultruded glass fiber reinforced polymer (pGFRP) I-section columns subject to short term concentric compression. A review of existing theories is presented, including the instability concepts, global and local buckling theories, perfect columns failure modes and the behavior of real columns. An experimental program including material characterization was conducted. Twenty-nine stubs – with three different I-sections geometries, having distinct flange width-to-section depth ratios ($bf/d = 0.5; 0.75$ and 1.0), mechanical properties, overall lengths and matrices – were tested. In a global point of view, the columns were fixed at both ends. The constituent plates, on the other hand, were tested with different end-conditions: clamped (CC), simply supported (SS) and simply in contact with base plates of the universal machine (CB). The third analyzed boundary condition, which is the most adopted in previous studies, was concluded to be closer to a clamped end-condition. The non-linear elastic strains distribution throughout the cross-section was also investigated. Finally, guideline recommendations for successful local buckling tests were proposed.

Keywords

Glass fiber reinforced polymer (GFRP); local buckling; column; end-condition.

Resumo

Cintra, Gisele Góes; Cardoso, Daniel Carlos Taisum (Orientador); Vieira, Janine Domingos (Co-orientadora). **Flambagem Local de Colunas Pultrudadas em Polímero Reforçado com Fibra de Vidro (pGFRP) com Seção I**. Rio de Janeiro, 2017. 171 p. Dissertação de Mestrado – Departamento de Engenharia Civil e Ambiental. Pontifícia Universidade Católica do Rio de Janeiro.

Este trabalho tem como objetivo investigar o desempenho de colunas com seção I em polímeros reforçados com fibra de vidro (pGFRP) submetidas a cargas de compressão concêntricas de curta duração. Uma revisão bibliográfica acerca das teorias existentes é apresentada, incluindo os conceitos básicos de instabilidade, teoria de flambagem global e local, modos de falha de colunas perfeitas, bem como o comportamento de colunas reais. Um programa experimental foi conduzido, incluindo a caracterização dos materiais. Vinte e nove colunas – com três diferentes seções I e diferentes tipos de resina, propriedades mecânicas, bem como comprimentos – foram testadas. Do ponto de vista global, as colunas foram biengastadas. As placas constituintes, por sua vez, foram testadas com três diferentes condições de contorno: biengastadas (CC), biapoiadas (SS) e simplesmente em contato com as chapas de base da máquina de compressão (CB). Foi observado que a condição de contorno CB – a mais adotada em estudos anteriores –, se aproxima mais de um engaste do que de uma condição simplesmente apoiada. A distribuição não linear de deformações elásticas ao longo da seção também foi investigada. Finalmente, recomendações para um ensaio de flambagem local apropriado foram propostas.

Palavras-chave

Polímero reforçado com fibra de vidro (GFRP); flambagem local; colunas; condições de contorno.

Table of contents

1. Introduction	22
1.1. Overview	22
1.2. Motivation	25
1.3. Objectives	26
1.4. Organization of the dissertation.....	27
2. Literature Review	29
2.1. Pultruded GFRP	29
2.2. Pultrusion Process	30
2.3. Mechanical Properties	34
2.3.1. Theoretical Prediction of Elastic Properties.....	35
2.4. Columns and Plates Behavior	39
2.5. Perfect Members	40
2.5.1. Global Buckling.....	42
2.5.2. Local Buckling.....	44
2.5.3. Signature Curve.....	46
2.6. Real Columns and Plates	49
2.6.1. Initial Geometric Imperfections	50
2.6.2. Failure Modes of Real Columns.....	50
2.7. Post-Buckling Behavior of Plates	52
2.8. Strength Curve	54
2.9. Previous Experimental Researches on Local Buckling of I-Sections	56
3. Experimental Program: Local Buckling of I-Sections	64

3.1.	Overview	64
3.1.	Studied I-sections.....	64
3.2.	Material Characterization	67
3.2.1.	Fiber Volume Fraction	68
3.2.2.	Longitudinal Bending Modulus and Strength ($E_{L,f}$ and $F_{L,f}$) ...	74
3.2.3.	Transverse bending ($E_{T,f}$)	78
3.2.4.	Shear Modulus (G_{LT}).....	82
3.2.5.	Compressive Modulus ($E_{L,c}$) and Strength ($F_{L,c}$)	92
3.2.6.	Summary of Material Properties	97
3.3.	Stub Column Tests.....	99
3.3.1.	Columns with Clamped Edges.....	102
3.3.1.	Columns with Simply Supported Edges.....	106
3.3.2.	Columns Directly in Contact with Base Plates	110
4.	Results Analyzes	112
4.1.	Overview	112
4.2.	Columns with Clamped Edges	113
4.3.	Simply-supported Plates	120
4.4.	Simply in contact with base plate	124
4.4.1.	Comparison between the three boundary conditions	125
4.5.	Strength curve and Slenderness map	130
4.6.	Guidelines Recommendations	132
5.	Conclusions	133
5.1.	Final Considerations.....	133
5.2.	Future Works.....	134
6.	References	135
7.	Appendix A – Column Tests Reports	144
7.1.	Clamped Plates.....	144

7.2.	Simply-supported Plates	162
7.3.	Plates simply in contact with base plates	168

List of figures

Figure 1.1 - Applications in structural systems (<i>Sources: (a) FIBERLINE Composites, 2017; KELLER et al., 2015; (b) COGUMELO, 2017; (c) KELLER et al., 2015; (d) Pultrusão do Brasil (2017); (e) COGUMELO, 2017; (f) FIBERLINE Composites, 2017a)</i>)	25
Figure 2.1 - Pultrusion process (LANDESMANN <i>et al.</i> , 2015).....	31
Figure 2.2 - Final product of pultrusion process (STRATUS Industries)...	31
Figure 2.3 - Fiberglass: Roving, mat and veil: (a) Scheme adapted from AMERICAN EDGE, 2017; (b) Picture taken at STRATUS Industries	32
Figure 2.4 - Composition of a typical pultruded plate (CREATIVE, 2017)	33
Figure 2.5 - Versatility in pultrusion process (STRONGWELL, 2017a)	33
Figure 2.6 - Representative volume element.....	35
Figure 2.7 – Simplifying assumptions (JONES, 1999): (a) longitudinal normal stress; (b) transverse normal stress; (c) in-plane shear stress	36
Figure 2.8 - Self-consistent doubly embedded model (CLARKE, 1996) ...	37
Figure 2.9 - Equilibrium configurations: (a) stable; (b) unstable; (c) neutral	39
Figure 2.10 – (a) Compressed plate (Adapted from REIS and CAMOTIM, 2001) ; (b) Representative curves of load versus transverse displacement (Adapted from LEISSA, 1985)	41
Figure 2.11 - Failure modes on axial compression: (a) crushing; (b) global buckling; (c) local buckling (LAU, SAID and YAAKOB, 2012) ..	41
Figure 2.12 – Flexural Global Buckling.....	42
Figure 2.13 - Effective lengths of columns (Adapted from REIS and CAMOTIM, 2001)	43
Figure 2.14 - Local buckling of a short I-section column	45
Figure 2.15 - Columns and plates end-conditions for an I-section: (a) columns end-condition; (b) plates end-condition.....	47
Figure 2.16 - Illustrative signature curve for given cross section, material	

properties and different boundary conditions.....	47
Figure 2.17 – Perfect and real columns behavior	49
Figure 2.18 - Initial geometric imperfections in columns and plates (CARDOSO, 2014): (a) out-of-straightness in columns; (b) out-of-straightness in plates	50
Figure 2.19 – Reduction of ultimate load caused by interaction mode (ESDEP, 2017).....	51
Figure 2.20 – Plates behavior (Adapted from BAZANT and CEDOLIN, 2010)	53
Figure 2.21 - Southwell plots: (a) for Euler columns (Adapted from BAZANT and CEDOLIN, 2010); (b) for plates (Adapted from SPENCER and WALKER, 1975)	54
Figure 2.22 - Normalized strength curve	56
Figure 2.23 - Restoring eccentricity caused by end conditions (CARDOSO <i>et al.</i> , 2015)	59
Figure 2.24 - local <i>versus</i> global slenderness map of previous studies....	62
Figure 3.1 – Studied I-Sections nominal dimensions: (a) I_1 ; (b) I_2 ; (c) I_3 ...	65
Figure 3.2 - I_2 -section profiles obtained by cutting parts of the flange of I_3 profiles.....	66
Figure 3.3 - Layers of I_1 profiles: (a) web layers; (b) flange layers.....	66
Figure 3.4 - Layers of I_2 profiles: (a) web layers; (b) flange layers.....	67
Figure 3.5 - Alphanumeric code for specimens' identification.....	68
Figure 3.6 - Burnout test: (a) samples; (b) crucible with samples extracted from I_1 and I_2	69
Figure 3.7 - Weighing: (a) Samples, (b) Crucibles.....	69
Figure 3.8 – (a) and (b): Desiccator with 9 of 12 crucibles containing the samples before being placed into the furnace; (c) muffle furnace	69
Figure 3.9 – Post-burn: (a) Crucible containing the post-burned samples; (b): Reweighing	70
Figure 3.10 (a) and (b) - Separation of roving from mat	70
Figure 3.11 - Three-point bending test scheme.....	74
Figure 3.12 - Coupons for bending test: (a) from I_1 ; (b) from I_2	75
Figure 3.13 - Bending test fixture	75
Figure 3.14 – Failure modes obtained: (a) interlaminar shear fracture	

(b) tensile fracture of fiber	76
Figure 3.15 - Stress-Strain Curve: (a) specimens from I_1 profiles;	
(b) specimens from I_2 profiles	77
Figure 3.16 – Extraction of T-shaped coupons from profile	79
Figure 3.17 - Specimens for the transverse bending test: (a) I_1 ; (b) I_2	79
Figure 3.18 - Transversal bending test: (a) test set-up; (b) strain	
gages position	80
Figure 3.19 - Bending Test Scheme and corresponding moment and	
axial force diagrams	81
Figure 3.20 - Curve $M \times 1/r$: (a) Coupons from I_1 ; (b) Coupons from I_2	81
Figure 3.21 – Specimen geometry adopted for torsion tests	83
Figure 3.22 - Non-standard torsion test fixture (Adapted from	
TOGASHI, 2017)	84
Figure 3.23 - Torsion test: (a) overview; (b) specimen twisted	85
Figure 3.24 – Portable Strain Indicator	85
Figure 3.25 - T versus $2J\epsilon_{45}/t$: (a) Specimens extracted from I_1 ;	
(b) Specimens extracted from I_2	87
Figure 3.26 - Adapted Iosipescu test fixture	88
Figure 3.27 – Tabbed specimens: (a) before being tested; (b) after	
being tested with failure between the V-notches; (c) third 45 deg strain	
gage positioned in the back of the specimen.....	89
Figure 3.28 – Iosipescu test: (a) alignment with load applied axis;	
(b) failure in pure shear stress region; (c) test fixture's overview.....	90
Figure 3.29 - Shear diagram based on test fixture's dimensions.....	91
Figure 3.30 - τ versus γ plot.....	91
Figure 3.31 - Untabbed Specimens: (a) extracted from I_1 ; (b) extracted	
from I_2	93
Figure 3.32 - Tabbed Specimens: (a) extracted from I_1 ; (b) extracted	
from I_2	93
Figure 3.33 - CLC Test Scheme (dimensions in mm).....	94
Figure 3.34 – CLC test: (a) test fixture; (b) detail of gage length;	
(c) failure within the gage length.....	94
Figure 3.35 - Strains measurements to ensure that buckling would	
not occur: (a) Strains measurements of specimen $I_{1.05.Co.AL}$;	

(b) Strains measurements of specimen I ₂ .06.Co.MI	95
Figure 3.36 - Stress-strain curves: (a) Coupons extracted from I ₁ ;	
(b) Coupons extracted from I ₂	96
Figure 3.37 - Alphanumeric code for stub identification	100
Figure 3.388 – Displacements transducers: (a) transducers 1 to 3;	
(b) transducers 1,2 and 4; (c) transducers' location (mm)	101
Figure 3.399 – Equipment required for the tests	102
Figure 3.40- Set-up used to avoid plates edges rotation:	
(a) Test fixture scheme for I ₁ (on the left) and I ₂ (on the right);	
(b) steel plates fixed on the base plate; (c) profile being regularized	
with filler material; (d) clamped wall end-condition	104
Figure 3.41 – Numbering and gages positions: (a) gages 1 to 5;	
(b) gages 6 to 9; (c) gages 9 to 12; (d) strain gages positions	
(dimensions in mm)	105
Figure 3.42 – Set-up for simply-supported plates: (a) scheme of the	
set-up; (b) simply supported plates; (c) column sliding off the roller	
axis	108
Figure 3.43 - Final set-up for simply supported plates: (a) Lateral view;	
(b) Frontal view; (c) Overview	109
Figure 3.44 – Slippage of long columns off the rollers: (a) Before;	
(b) After	109
Figure 3.45 – Plates simply in contact with base plate	111
Figure 4.1 - Representative Southwell plot of I3.ES.04.550	112
Figure 4.2 - Overviews of the shorter tested stubs:	
(a) Failure of I1.03.300 (bf/d=0.5); (b) I2.ES.03.250 (bf/d=0.75);	
(c) I3.ES.01.300 (bf/d=1.0)	113
Figure 4.3 - Displacement growth of the tested stub I1.PO.06.600	
(bf/d=0.5)	113
Figure 4.4 – Displacement growth of the tested stub	
I2.ES.06.550 (bf/d=0.75)	114
Figure 4.5 - Displacement growth of the tested stub	
I3.ES.06.550 (bf/d=1.00)	114
Figure 4.6 - P versus δ curves: (a) for shorter stubs:	
I1.PO.03.300, I2.ES.03.300, I3.ES.03.300; (b) for longer	

stubs: I1.PO.04.600, I2.ES.05.550, I3.ES.04.550	115
Figure 4.7 – Comparison between theoretical signature curve and experimental results	117
Figure 4.8 - Displacement growth of the tested stub I3.ES.07.495.....	118
Figure 4.9 – Non-linear strain distribution across flange according to load level	119
Figure 4.10 - Load P versus curvatura $1/r$	119
Figure 4.11 - Southwell Plot	120
Figure 4.12 – Displacement growth of the tested stub I3.ES.01.300 (bf/d=1.00)	121
Figure 4.13 – Displacement growth of the tested stub I3.ES.05.550 (bf/d=1.00)	121
Figure 4.14 – End crushing of I_2 sections profiles	122
Figure 4.15 - Stresses distribution through the thickness in the loading region.....	122
Figure 4.16 - P versus δ curves of shorter and longer stubs: I3.ES.02.300; I3.ES.05.550	122
Figure 4.17 - Theoretical signature curve and experimental results	123
Figure 4.18 – Displacement growth of the tested stub I3.ES.01.300 (bf/d=1.00)	124
Figure 4.19 – Displacement growth of the tested stub I3.ES.04.550 (bf/d=1.00)	124
Figure 4.20 – End of an I_3 stub tested on a direct contact condition	125
Figure 4.21 – End crushing of the tested stub I2.ES.06.550: (a) broom-like failure	125
Figure 4.22 - Ratio of experimental results and theoretical predictions	126
Figure 4.23 - Load P versus deflections δ plots: (a) shorter stubs: I3.03 (CC), I3.02 (SS), I3.02 (CB); (b) longer stubs: I3.04 (CC), I3.05 (SS), I3.03 (CB)	127
Figure 4.24 - Theoretical signature curves and experimental results for I_3 stubs.....	129
Figure 4.25 – (a) Strength curve; (b) zoom in the experimental points.....	130

Figure 4.26 - local <i>versus</i> global slenderness map	131
--	-----

List of tables

Table 2.1 - Properties of glass fibers (BANK, 2006)	29
Table 2.2 - Properties of thermosetting resins (Adapted from BANK, 2006)	30
Table 2.3 - Reported mechanical properties of pultruded GFRP	34
Table 2.4 - Coefficients for Halpin-Tsai equation (CLARKE, 1996)	38
Table 2.5 - Shear form factors for I-sections	44
Table 2.6 - Classification of columns and plates with their expected failure modes (CARDOSO <i>et al.</i> , 2014).....	52
Table 2.7 - Summary of I-section local buckling tests conducted in previous works	61
Table 2.8 - Length, flange-to-depth ratio and end-conditions adopted on previous studies.....	63
Table 3.1 - Specifications of studied profiles	65
Table 3.2 – Characterization tests and respective properties obtained	67
Table 3.3 - Weight w_1 , w_2 and w_3	71
Table 3.4 - Specific masses	71
Table 3.5 - Fibers contents by weight and volume for I1 sections	72
Table 3.6 - Fibers contents by weight and volume for I2 section.....	73
Table 3.7 – Specimens dimensions.....	74
Table 3.8 - Flexural Modulus of I_1	77
Table 3.9 - Flexural Modulus of I_2	77
Table 3.10 - Flexural Strength of I_1	78
Table 3.11 - Flexural Strength of I_2	78
Table 3.12 – Adopted dimensions	80
Table 3.13 - Transverse Bending Modulus of I_1	82
Table 3.14 - Transverse Bending Modulus of I_2	82
Table 3.15 - Specimens dimensions	84

Table 3.16 Shear moduli of I_1 sections	87
Table 3.17 - Shear moduli of I_2 sections	87
Table 3.18 – Specimens dimensions	89
Table 3.19 - Shear modulus of specimens from I_2	91
Table 3.20 - Specimens' Dimensions - Compression Test	92
Table 3.21 - Compressive Modulus of I_2	96
Table 3.22 - Compressive Modulus of I_1	96
Table 3.23 - Compressive Strength of I_1	97
Table 3.24 - Elastic properties of fibers and resins	98
Table 3.25 – Summary of material properties obtained experimentally and comparison with theoretical prediction	98
Table 3.26 - Local Buckling Tests Summary	99
Table 3.27 - Average cross-section dimensions, lengths and calculated areas.	103
Table 3.28 – Ratio of average measured and nominal dimensions	103
Table 3.29 - Average dimensions of I3.ES.07.495 and ratio of measured and nominal dimensions	105
Table 3.30 - Attempts to reproduce a column with simply supported plates edges	107
Table 3.31 - Average dimensions and cross-sectional area of simply supported stubs	110
Table 3.32 - Ratio of average measured dimensions and nominal dimensions	110
Table 3.33 – Average stubs dimensions, cross-sectional areas and lengths	111
Table 3.34 - Ratio of average measured dimensions and nominal dimensions	111
Table 4.1 - Ratio of theoretical predictions and experimental results	116
Table 4.2 - Ratio of experimental results and theoretical predictions	123
Table 4.3 - Experimental critical load for CB columns	128
Table 4.4 - Ratio of experimental CB and CC/SS critical loads	128
Table 4.5 – Ratio of experimental CB and theoretical CC/SS critical loads	128

List of symbols

Lowercase Roman Letters

b	plate width
c	coefficient
b_f	flange width
b_w	web height; center to center of the flanges
d	section depth; distance
d_v	distance between V-notches
e	distance between applied load and coupon's centroid
k_{cr}	critical plate buckling coefficient
n_s	shear form factor
r	radius of gyration
s	deflection
t	thickness
t_f	flange thickness
t_w	web thickness
w	plate out-of-plane deflection
w_1	weight of the porcelain crucible
w_2	weight of the porcelain crucible containing the sample
w_3	weight of the porcelain crucible containing the post-burned sample
x	in-plane longitudinal axis
y	in-plane transverse axis
z	out-of-plane transverse axis

Uppercase Roman Letters

A	cross-section area
$E_{L,c}$	compressive modulus of elasticity in the longitudinal direction

E_{Lf}	flexural modulus of elasticity in the longitudinal direction
E_{Tf}	flexural modulus of elasticity in the transverse direction
F_e	Euler buckling critical stress
F_{cr}	local buckling critical stress
$F_{L,c}$	compressive strength in the longitudinal direction
F_{Lf}	flexural strength in the longitudinal direction
F_u	ultimate stress
G_{LT}	in-plane shear modulus
G_{TT}	through-thickness shear modulus
J	Saint-Venant torsion constant
L	column/plate length
K_e	buckling coefficient for flexure
M	bending moment
P	load
$P_{L,c}$	compressive maximum load in the longitudinal direction
P_{cr}	critical load
$P_{cr,e}$	experimental critical load
$P_{cr,t}$	theoretical critical load
P_u	ultimate experimental load
Q	elastic property
T	Torque
V_f	fiber content, in volume
W	fiber content by weight

Lowercase Greek Letters

α	column imperfection factor
β	coefficient
γ_{LT}	shear strain
δ	deflection
ε	strains
ε_x	axial strain
ε_y	transverse strain

η	ratio of flange-to-web widths
θ	angle of rotation
λ_g	column relative slenderness
λ_l	plate relative slenderness
ν_{LT}	major Poisson's ratio
ν_{TL}	minor Poisson's ratio
σ	stress
σ_x	stress in the longitudinal direction
σ_y	stress in the transverse direction
τ_{LT}	shear stress
χ_c	column relative strength
χ_l	plate relative strength

Uppercase Greek Letters

Σ	summation
----------	-----------

1. Introduction

1.1. Overview

Fiber reinforced polymers are composite materials constituted of high strength fibers embedded in a resin matrix. The combination of the two chemically distinct materials allows achieving particular properties that cannot be individually obtained by the constituents. In general, the fibers act as the reinforcement, providing load-carrying capacity and stiffness, whereas the polymeric matrix is responsible for bonding the fibers together, transferring the applied external loads to them. The matrix also protects the reinforcement against deterioration and contributes to increase bending and shear strengths (MALLICK, 2007). In this work, glass fiber reinforced polymer (GFRP) composite is studied, which consist in a polymeric matrix reinforced by glass fibers

The earliest applications of GFRP products date to 1940's, in marine and aerospace industries. Because of its lightweight, corrosion resistance and high strength, this composite proved to be very suitable for military applications. During the Cold War, the evolution in the defense and the challenges of space exploration had demanded an intensive use of these composites (ACI Committee, 2001). Nevertheless, beyond these niche markets, the high manufacturing costs were an obstacle to make these products attractive and competitive (BAKIS *et al.*, 2002). This scenario began to change in 1951, when an automate continuous molding process called pultrusion was invented, offering a fast and economical method of producing GFRP profiles. The significant number of researches and demonstration projects funded by governments and industries worldwide contributed to a better comprehension of the material and, since the 1990's, the use of GFRP in primary load-bearing structural systems has increased (BAKIS *et al.*, 2002).

In addition to the advantages mentioned previously, other features such as resistance to a broad range of chemicals, electromagnetic transparency, low

thermal and electrical conductivity, fatigue resistance, low maintenance costs and easy installation, make pultruded GFRP (pGFRP) an interesting alternative to traditional construction materials. Among the applications, one may cite its use in pedestrian bridges, cooling towers, bridges decks, buildings, *off-shore* structures, as well as in the rehabilitation and transformation of existing buildings. (STRONGWELL, 2017, CORREIA, BAI and KELLER, 2015). Figure 1.1 shows some applications in structural systems:

- The *Pontresina* Bridge (a) is a pedestrian bridge, constructed in 1997. The structure consists in two truss girders – composed of pultruded GFRP profiles – that work as the main load-carrying elements of the bridge. Every year, the bridge is only used during the winter of Switzerland. Because of its low self-weight, it can be easily removed during the spring for durability inspection in laboratory (KELLER, 2002).
- The façade of *Fasano* Hotel (b) at Rio de Janeiro, Brazil is made with pultruded GFRP profiles. The choice of the composite was due to its corrosion resistance in aggressive sea coastal environment.
- The *Eyecatcher* Building (c) was constructed in Switzerland in 1999. It was conceived as a reusable temporary structure and it's the tallest FRP building in the world. Three parallel multilayer GFRP frames connected by timber slabs compose the primary load-bearing structure (KELLER *et al.*, 2015).
- The salt storage unit of *Tortuga* (d) was built in São Paulo, Brazil, in 2014. It is one of the biggest structures made of pGFRP in the country. All the roof and the cladding, such as the roof trusses, purlins and bracings were made of pultruded GFRP.
- The figure (e) shows a staircase tower entirely made of pultruded profiles;
- The *Kolding* Bridge (f) is a pedestrian and cyclist bridge constructed in Denmark in 1997. The full bridge was installed during 18 hours over three nights.

During last three decades, researchers and industry have dedicated significant efforts worldwide to develop standard provisions to spread use of material and allow for safe structural design. Among these documents, it is important to cite the *American Society of Civil Engineers (ASCE) - Structural Plastic Design Manual*

(GRAY, 1984), the *EUROCOMP Design Code and Handbook* (CLARKE, 1996), the *Italian Guide for the Design and Construction of Structures Made of FRP Pultruded Elements* (CNR, 2008), the *ASCE Pre-Standard for Load and Resistance Factor Design (LRFD) of Pultruded Fiber Reinforced Polymer (FRP) Structures (Final)* (ASCE, 2010) and the *Prospect for new guidance in the design of FRP: Support to the implementation, harmonization and further development of the Eurocodes* (ASCIONE *et al.*, 2016). In Brazil, NBR 15708 (2011) specifies minimum mechanical properties for pGFRP profiles test methods for quality assurance.



(a) Pontresina Bridge, Switzerland (1997)



(b) Fasano Hotel, Brazil (2007)



(c) Eyecatcher Building, (1999)



(d) Salt Storage Unit of *Tortuga*, Brazil (2014)



(e) Staircase Tower



(f) *Kolding* Bridge, Denmark (1997)

Figure 1.1 - Applications in structural systems (*Sources: (a) FIBERLINE Composites, 2017; KELLER et al., 2015; (b) COGUMELO, 2017; (c) KELLER et al., 2015; (d) Pultrusão do Brasil (2017); (e) COGUMELO, 2017; (f) FIBERLINE Composites, 2017a*)

1.2. Motivation

Pultruded GFRPs are materials with high compressive strength and low longitudinal modulus. The former ranges from 200 to 500 MPa – being similar to mild structural steel, whereas the latter varies from 17 to 35 MPa – approximately 1/12 to 1/6 that of steel. The high strength-to-modulus ratio, in addition to the use

of slender sections under compression leads to important instability problems that may reduce the load capacity of the structural member (CARDOSO, 2014).

In the last decades, a considerable number of studies – including experimental tests, numerical analyzes and analytical solutions – have been carried out to develop concise and solid standard provisions. Nevertheless, there remain important gaps in the understanding of the behavior of these structures, especially about local buckling of columns.

The first motivation for this work revolves around the experimental procedures adopted in previous works. In order to avoid global buckling, most of previous tests have been conducted considering column base rotation restrained at both ends. However, local buckling is associated to plate bending and the end conditions for the cross-section constituent *plates* need to be taken into consideration. To simplify test set-up, previous studies have adopted the edges simply in contact with base plates, without reproducing neither clamped nor simply supported end- conditions. Further, the columns' lengths adopted in tests reported in literature vary widely. This lack of consensus on the most appropriate columns' length, added to end-conditions not well defined may lead to a wide range of results and interpretations.

A second motivation for this work arises from the fact that most of previous works have focused on I-sections with flange width equal to section depth ($b_f/d=1.0$) leading to lack of information about sections with different b_f/d ratios.

Finally, there is still little information about the non-linear strain distributions throughout the cross-section during the loading. This effect is responsible for the stiffening of the system and have influence on the structure behavior until failure, leading to apparently greater experimental critical loads than those theoretically predicted.

1.3. Objectives

The main objective of this work is to investigate the influence of column length and *plates* end-conditions on the local buckling critical load. In order to accomplish this task, a review on available previous studies and existing theory is

presented, including the instability concepts applied to perfect members, along with real columns and plates theory, addressing the effect of initial imperfections on the structures behavior. Global and local buckling theories are also presented, as well as the expected failure modes depending on columns and plates slenderness. Useful tools, such as the signature curve and the slenderness map, are presented in order to provide right directions for a well-controlled local buckling test.

With the purpose of gathering information on local buckling behavior of pGFRP columns, an experimental program addressing stub columns subject to concentric compression was carried out. Three different I-sections columns having distinct flange width-to-section depth ratios ($b_f/d = 0.5; 0.75$ and 1.0), mechanical properties, overall lengths and polymers matrices (polyester and vinyl ester) were tested. Different *plates* end-conditions were analyzed, while *column* bases rotations remained restrained at both ends. One of these stubs ($b_f/d = 1.0$) was instrumented with strain gages across the section in order to capture non-linear elastic strain distributions during loading and to investigate its influence on the experimental critical loads. Additionally, guideline recommendations for successful buckling tests are proposed, in view of the previously mentioned lack of consensus on these experimental procedures.

A secondary objective of this work is to study the applicability of available methods to experimentally determined material properties – proposed by American Society for Testing and Materials (ASTM) and International Organization for Standardization (ISO) –, as well as its respective correlation with theoretical methods. In this work, relevant material properties were obtained through standard and non-standard tests.

1.4. Organization of the dissertation

This work is organized as follows:

- Chapter 2 addresses literature review from the physical and mechanical properties of the composite constituents until instability concepts and previous experimental works about local buckling. The behavior of perfect and real columns and plates is also addressed. The general concept of

signature curve and the influence of length and boundary conditions in critical loads are discussed. Failure modes and factors affecting the real column behavior and strength are also presented.

- Chapter 3 describes the experimental program, which includes I-section stub column tests, as well as the material characterization tests.
- Chapter 4 presents the results analysis from the experimental program, comparisons and discussions related to the observed behavior of the tested columns. Further, guideline recommendations for pGFRP local buckling column tests are proposed.
- Chapter 5 presents the relevant conclusions and suggestions for future works.

2. Literature Review

2.1. Pultruded GFRP

Glass fiber reinforced polymer composites may be constituted of different types of glass-fiber and resins, depending on the desired application. The grades of glass fibers are identified by letter nomenclature: *E-glass (electrical glass)* is a borosilicate glass with high electrical resistivity used in the vast majority of FRP products for structural engineering; *A-glass (window glass)* and *C-glass (corrosion resistant glass)* – also called *AR-glass (alkali-resistant glass)* – are used in specialized applications that demand high chemical resistance; and *S-glass (structural or high-strength glass)* is used to enhance the strength and stiffness (BANK, 2006). Table 2.1 presents the physical and mechanical properties of glass fibers.

Table 2.1 - Properties of glass fibers (BANK, 2006)

Glass Fiber	Density (g/cm³)	Tensile Modulus (MPa)	Tensile Strength (MPa)	Max. Elongation (%)
<i>E</i>	2.57	72.5	3400	2.5
<i>A</i>	2.46	73	2760	2.5
<i>C</i>	2.46	74	2350	2.5
<i>S</i>	2.47	88	4600	3.0

Glass fibers are particularly sensitive to moisture and alkaline environment and therefore need to be protected by the matrix (BANK, 2006). Resins can be selected to obtain particular mechanical properties, such as chemical resistance, fire retardation and temperature resistance. The polymer resins can be classified in two primary groups: *thermosetting* and *thermoplastic* polymers. The former cures during the polymerization process and cannot be re-shaped once hardened,

although it deteriorates when exposed to elevated temperatures. Pultruded GFRP are usually made of thermosetting polymers such as polyester, epoxy, vinylester and phenolic. Thermoplastic polymers, on the other hand, liquefy when heated and solidifies when cooled and polyethylene, polyvinyl chloride and polyimide (nylon) are representative polymers of this group (BANK, 2006, SERUTI, 2013). Table 2.2 presents the physical and mechanical properties of some of the most commons thermosetting matrices.

Table 2.2 - Properties of thermosetting resins (Adapted from BANK, 2006)

<i>Resins</i>	<i>Density</i> (g/cm ³)	<i>Tensile</i> <i>Modulus (MPa)</i>	<i>Tensile</i> <i>Strength (MPa)</i>	<i>Max.</i> <i>Elongation (%)</i>
<i>Polyester</i>	1.2	4.0	65	2.5
<i>Epoxy</i>	1.2	3.0	90	8.0
<i>Vinylester</i>	1.12	3.5	82	6.0
<i>Phenolic</i>	1.24	2.5	40	1.8

2.2. Pultrusion Process

Pultrusion is an automate continuous molding process of fiber reinforcement composites. The process consists in pull reinforcement materials, such as fiberglass roving, mat or veil (Figure 2.3) through a resin bath, impregnating all the fiber with a liquid thermosetting resin. The wet fiber is drawn to a heated steel die, where the resin is cured at elevated temperatures. When solidified, the profile has the exact cavity shape of the die, as it is continuously pulled by the pultrusion machine (CREATIVE, 2017). Figure 2.1 presents a scheme of pultrusion process, while Figure 2.2 presents a picture of the manufacturing process, taken at Stratus Industries, at São Paulo, Brazil.

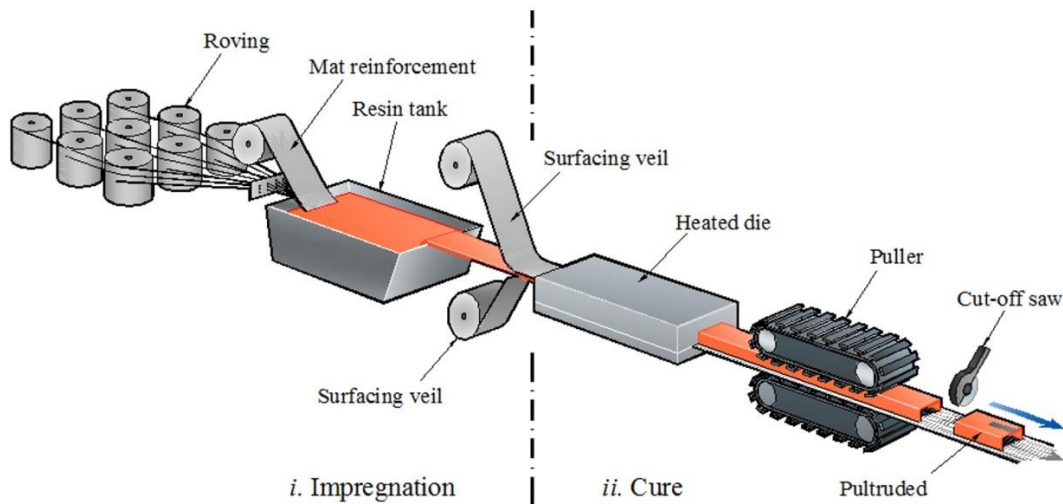


Figure 2.1 - Pultrusion process (LANDESMANN *et al.*, 2015)



Figure 2.2 - Final product of pultrusion process (STRATUS Industries)

As mentioned previously, the reinforcement of pultruded GFRP are divided in three components: i) *rovings* are bundles of fibers aligned in pultrusion direction that provide the high longitudinal strength of pultruded products and the necessary tensile strength to pull the other fibers through the heated die; ii) *continuous strand mats (CSM)* are bidirectional mats made of randomly orientated strands responsible for the transverse mechanical properties of the composite; iii) *surface veils* –made of polyester or A-glass – are usually added to the external surfaces to improve corrosion resistance and protect the composite against ultraviolet (UV) degradation, as well as to provide better surface finishing. (CREATIVE, 2017). Figure 2.3a illustrates the typical reinforcement layers in a pultruded GFRP and Figure 2.3b

shows a picture taken from a real pultruded GFRP member during a technical visit at Stratus Industries.

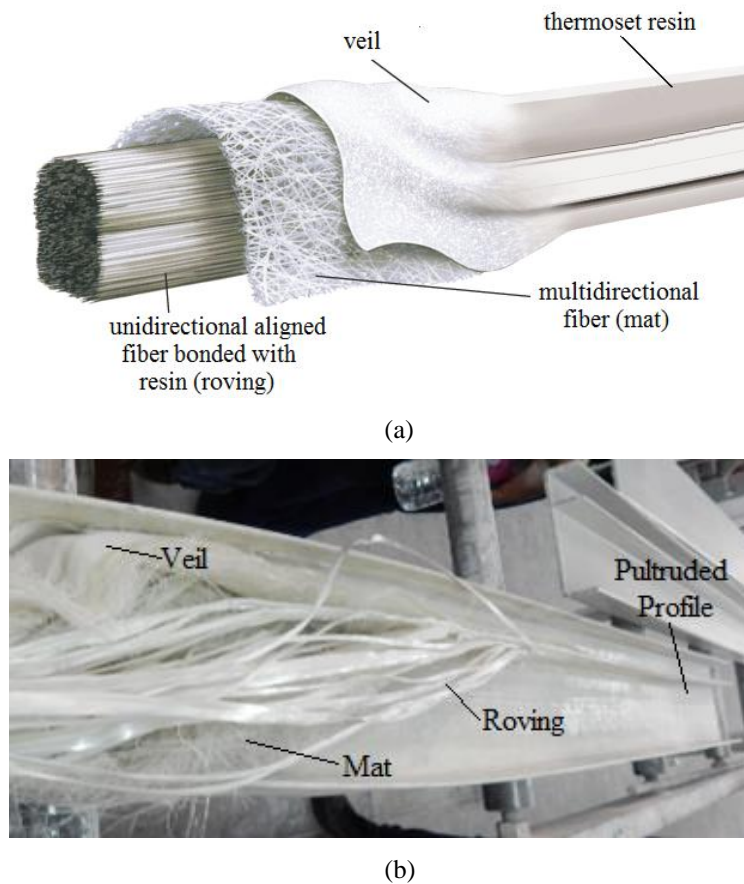


Figure 2.3 - Fiberglass: Roving, mat and veil: (a) Scheme adapted from AMERICAN EDGE, 2017; (b) Picture taken at STRATUS Industries

Usually, the performance of a fiber reinforced composite improves as the fiber volume ratio (V_f) increases, as long as the fibers are completely embedded by the matrix (SERUTI, 2013). In practice, V_f ranges from 0.30 to 0.60, with rovings corresponding to about 50-70% of this volume. According to McCARTHY and BANK (2011), the cross-sections of pultruded profiles are intentionally non-homogeneous, with different fiber contents for each wall: flanges are constituted of larger fractions of rovings (for bending), whereas webs contains larger fractions of mats (for shear). This difference is not always acknowledged by manufacturers and only mean moduli and strengths are reported. Additionally, the number of roving layers vary within the wall, ranging from one to four in typical pultruded profiles, depending on the wall thickness (CARDOSO, 2014). Figure 2.4 shows the composition of a typical pultruded plate.

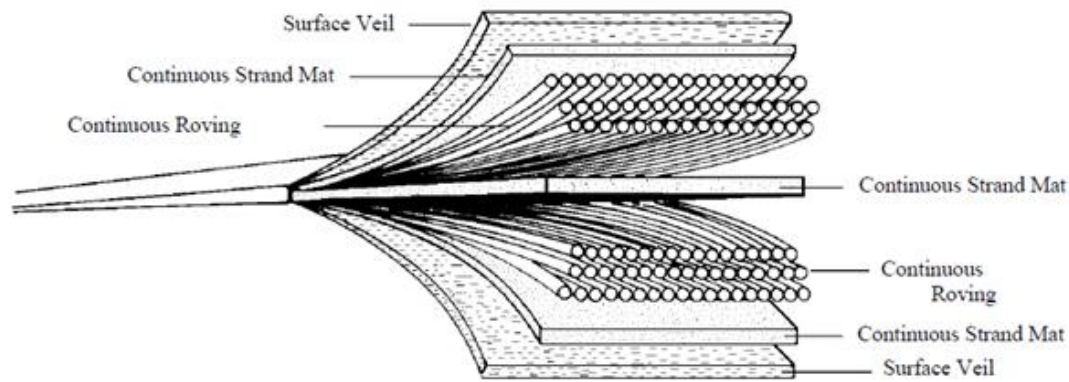


Figure 2.4 - Composition of a typical pultruded plate (CREATIVE, 2017)

An important advantage of pultrusion process is the versatility in section geometry, as shown in Figure 2.5, allowing manufacturing a wide variety of shapes such as angles, channels and I-sections. In most of commercially available sections, thicknesses of flanges and web are the same.

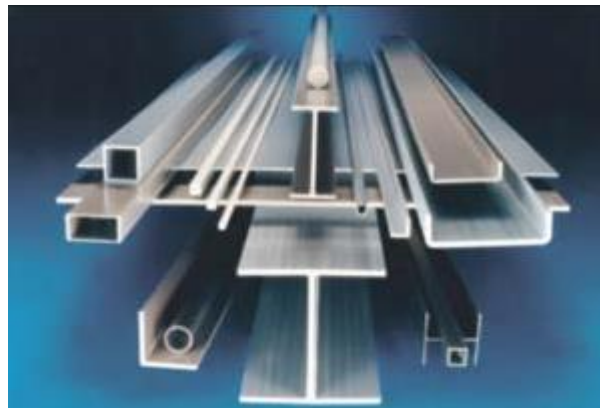


Figure 2.5 - Versatility in pultrusion process (STRONGWELL, 2017a)

Mechanical properties can also vary depending on the number of layers of each reinforcement type (fiber architecture) and fiber content adopted by each manufacturer. Table 2.3 presents typical mechanical properties reported by three different manufacturers – two from U.S. (Strongwell and Creative Pultrusion) and one from Brazil (Cogumelo) –, as well as the properties, obtained experimentally, of the two profiles studied in this work.

Table 2.3 - Reported mechanical properties of pultruded GFRP

<i>Properties</i>		<i>Cogumelo</i> ⁽¹⁾	<i>Strongwell</i> ⁽²⁾	<i>Creative</i> ⁽³⁾	<i>I₁</i> ⁽⁴⁾	<i>I₂</i> ⁽⁵⁾
<i>Longitudinal</i>	<i>Tensile Strength (MPa)</i>	210 – 260	207	279	-	-
	<i>Tensile Modulus (GPa)</i>	17.5 – 21	17.9	25	-	-
	<i>Compressive Strength (MPa)</i>	210 – 260	207	329	214.3	283.7
	<i>Compressive Modulus (GPa)</i>	17.5	17.9	22.9	24.3	33.7
	<i>Flexural Strength (MPa)</i>	210 – 260	207	341	265.7	384.2
	<i>Flexural Modulus (GPa)</i>	11.2 – 14	11.0	13.4	14.7	15.6
<i>Transversal</i>	<i>Tensile Strength (MPa)</i>	49 – 70	48,3	133	-	-
	<i>Tensile Modulus (GPa)</i>	5.6 – 7	5,5	9.4	-	-
	<i>Compressive Strength (MPa)</i>	105 – 140	110	126.6	-	-
	<i>Compressive Modulus (GPa)</i>	7 – 8.4	5,5	13.1	-	-
	<i>Flexural Strength (MPa)</i>	70 – 98	68.9	137.	-	-
	<i>Flexural Modulus (GPa)</i>	5.6 – 7	5,5	12.06	5.8	7.8
<i>Shear Modulus (GPa)</i>		-	2.9	3.4	2.3	3.1

(1) (*apud* ALMEIDA, 2004)

(2) (STRONGWELL, 2016)

(3) (CREATIVE, 2017)

(4) e (5) Experimental data

It is important to remember that pultruded GFRP are orthotropic materials and have a linear-elastic behavior in the longitudinal direction, exhibiting brittle rupture. According to BANK (2013), thermosetting polymer matrices have a considerably large strain to failure ($\epsilon_{fu} \approx 5\%$), but they are also brittle materials like the high-strength fibers ($\epsilon_{fu} < 1,5\%$). At higher strains, the typical behavior is found to be nonlinear in the shear and transverse direction. Nevertheless, for design properties, they are commonly assumed as linear elastic. GFRP also exhibits large deformation with time under sustained loads and is susceptible to creep rupture (BANK *et al.*, 1995, BANK, 2006). However, it is important to say that this phenomenon is not usually observed on the fiber's direction in profiles with high fiber volume fraction.

2.3. Mechanical Properties

The mechanical properties in each direction can be determined experimentally or by theoretical predictions. The former allows better correlations

between theory and actual behavior, once the latter is based on micromechanics analysis and have some limitations (JONES, 1999). In this work, the properties were obtained experimentally through characterization tests and were compared with the theoretical predictions presented in the following section.

2.3.1. Theoretical Prediction of Elastic Properties

As mentioned previously, FRP mechanical properties are affected by fiber content and architecture. Therefore, it is important to understand how the constituents can be combined to obtain desired properties in design (CLARKE, 1996).

There are several theoretical methods available in literature to predict the elastic properties of a unidirectional composite, separated in two main groups (JONES, 1999): i) through the mechanics of materials models or ii) through the theory of elasticity. The main difference between these two mentioned approaches is that the former assumes compatibility of strains in a representative volume element, whereas the latter is based on the variational energy principles. In mechanics of materials approach, also called *Rule of Mixtures* (ROM), fiber geometry and distribution is not relevant. On the other hand, in the theory of elasticity, numerical solutions are usually required to analyze the complex geometries of the representative volume elements (MALLICK, 1997, JONES, 1999).

The Rule of Mixtures approach assumes the total applied force in the composite be equal to the sum of the forces in the fiber and in the matrix in a simplified representative volume (MALLICK, 1997), shown in Figure 2.6.

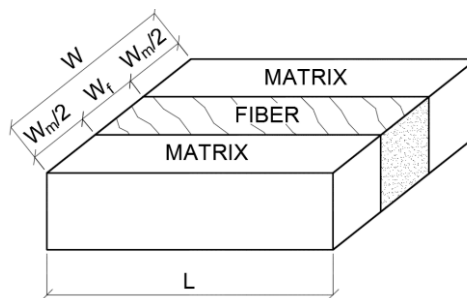


Figure 2.6 - Representative volume element

Figure 2.7 presents simplifying assumptions in order to determine the elastic properties of a unidirectional fiber reinforced composite. The most standout assumption is that strains in the longitudinal direction are the same in fibers and matrix and therefore, the sections remain plane after stressing. The longitudinal composite modulus (E_L) is dominated by the fiber modulus and is obtained through the stress state illustrated in Fig. 2.7a. On the other hand, in the transverse modulus (E_T) prediction, given by loading shown in Figure 2.7b, only stresses are assumed to be the same both in fiber and matrix, once no assumptions about the strains can be made. In the same way, the in-plane shear modulus (G_{LT}) is predicted by presuming that the shear stresses applied on fibers and matrix are the same, whereas the deformations are not. Because of its lower shear modulus, the matrix deforms more than the fiber, as shown in Figure 2.7c. In this method, the shear-stress strain behavior is considered linear, which is not reported as true in literature, as mentioned previously. The major Poisson's ratio is obtained by presuming a similar approach used to determine the longitudinal modulus (JONES, 1999).

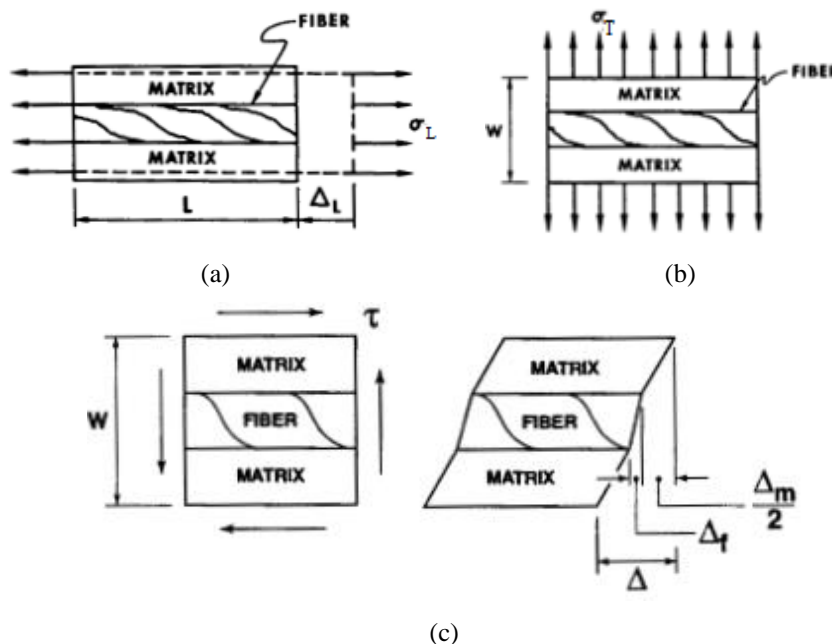


Figure 2.7 – Simplifying assumptions (JONES, 1999): (a) longitudinal normal stress; (b) transverse normal stress; (c) in-plane shear stress

The rule of mixtures does not account for the degree of bonding, fiber spacing, fiber shape, packing geometry and other factors that can influence transverse properties. Nevertheless, it is considered conservative and therefore, the

actual properties are usually higher than those predicted by Eq. 2.1 to 2.4 (CLARKE, 1996).

$$E_L = E_f V_f + E_m V_m \quad (2.1)$$

$$E_T = \frac{E_f E_m}{E_f (1 - V_f) + E_m V_f} \quad (2.2)$$

$$G_{LT} = \frac{G_f G_m}{G_f (1 - V_f) + G_m V_f} \quad (2.3)$$

$$\nu_{LT} = V_f \nu_f + V_m \nu_m \quad (2.4)$$

where E_L , E_T , G_{LT} are the longitudinal, transverse and shear moduli for the composite, respectively; ν_{LT} is the major Poisson's ratios for the composite. The subscribed letters m and f correspond to properties of matrix and fibers, respectively. The letters E , G and V indicates the elasticity moduli, shear moduli and the constituent volumetric fraction, whereas ν represents the Poisson's ratio.

In the elasticity approach, the *self-consistent method* has been studied by many authors (*e.g.* HASHIN and ROSEN, 1965, WHITNEY and RILEY, 1966, HILL, 1965, HERMANS, 1967, WHITNEY, 1967). *The Eurocomp Handbook* (CLARKE, 1996) recommends the *self-consistent doubly embedded method*, based on the transverse isotropy. The method assumes a single fiber embedded in a micro-region of the matrix, which is embedded itself in a homogeneous medium (Fig. 2.8).

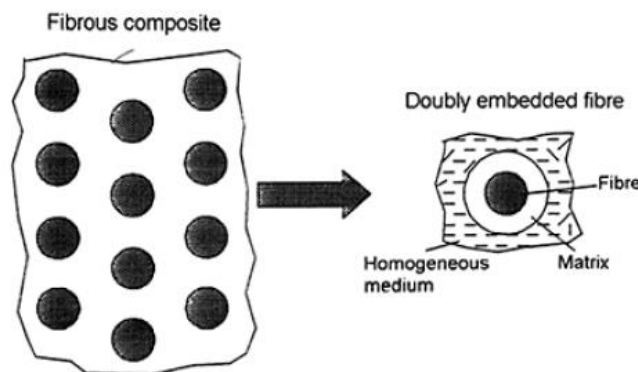


Figure 2.8 - Self-consistent doubly embedded model (CLARKE, 1996)

In this model, the composite material has the identical effective properties of the mentioned homogeneous material, which is a transversely isotropic material. These geometrical simplifications “*mask the extent to which neighboring fibers mutually influence their response characteristics*” (CLARKE, 1996) and tend to underestimate properties in composites with high fiber volume ratio. However, the method provides useful approximations for the elastic properties of unidirectional composites. By applying a uniform strain field in the longitudinal direction of the fibers, a set of Equations, showed by CLARKE (1996), results in the *Halpin-Tsai equation* given in Eq. 2.5:

$$Q = \frac{Q_m [Q_f + \xi Q_m + \xi V_f (Q_f - Q_m)]}{[Q_f + \xi Q_m - V_f (Q_f - Q_m)]} \quad (2.5)$$

where Q_m and Q_f are the matrix and fiber properties, respectively, and ξ , given in Table 2.4, is the property coefficient associated with the elastic property Q .

Table 2.4 - Coefficients for Halpin-Tsai equation (CLARKE, 1996)

<i>Elastic Property Q</i>	ξ
E_L	∞
ν_{LT}	∞
$E_T (V_f < 0.65)$	2.0
$E_T (V_f \geq 0.65)$	$2.0 + 40 V_f^{10}$
$G_{LT} (V_f < 0.65)$	1.0
$G_{LT} (V_f \geq 0.65)$	$1.0 + 40 V_f^{10}$

The equations presented previously can be successfully used to determine the properties of a unidirectional composite (or lamina), but do not apply for layers reinforced with continuous strand mat (CSM), for which fibers are randomly oriented. NIELSEN and CHEN (1968) proposed an integral considering the two-dimensional random fiber orientation, assuming the planar isotropy (*apud* MALLICK, 1997). An approximate solution was presented by HULL (1996), as reproduced in Eq. 2.6 and 2.7.

$$E_{csm} = \frac{3}{8} E_L + \frac{5}{8} E_T \quad (2.6)$$

$$G_{csm} = \frac{1}{8}E_L + \frac{1}{4}E_T \quad (2.7)$$

NAUGHTON (1985) conducted tensile and shear tests on chopped strand mats and woven rovings to investigate Hull's equations. It was found a difference of approximately 18% between the longitudinal and transverse moduli of the CSM, showing that the general assumption of planar isotropy is not true. The experimental values of G_{LT} were in good agreement with the predicted ones.

2.4. Columns and Plates Behavior

Buckling can be defined as the loss of original shape of a structural member associated with the change in the state of equilibrium. Theories of stability are required for its analyzes. In a conservative system, the stability concept is related to the minimum potential energy, which can be illustrated by the classical example of a ball on a curved surface. If the system is stable (Figure 2.9a), the ball will begin to oscillate when disturbed, but will remain in the close neighborhood of its equilibrium state. On the other hand, the equilibrium is unstable (Figure 2.9b) if the system is not in a configuration of minimum potential energy and, in this case, the ball will experience significant motions and increasing velocity until a new stable equilibrium configuration is found. Finally, the equilibrium is called neutral (Figure 2.9c) if the ball rests on a flat plane. The stiffness is defined as the slope of the surface in the ball example and is found through the derivative of the potential energy with respect to displacement.

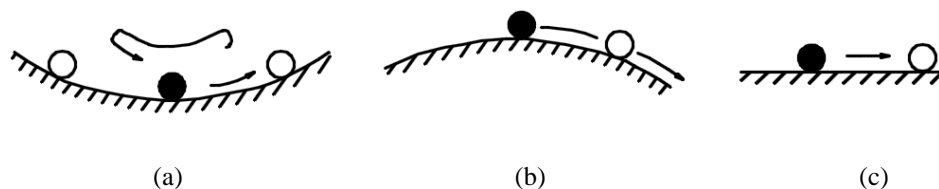


Figure 2.9 - Equilibrium configurations: (a) stable; (b) unstable; (c) neutral

Buckling analysis is particularly important in Pultruded GFRP members due to the association between low elastic properties of material and slender thin-walled

members usually adopted. Further, as mentioned previously, pultruded GFRP behaves in linear-elastic manner for large deflections and strains and, therefore, buckling is the governing failure mode for columns, especially those with wide flange (WF) sections (TOMBLIN and BARBERO, 1994). Slender members tend to exhibit overall buckling before experiencing any other instability failure. On the other hand, local buckling occurs first for short columns. The interaction between these two modes is an important phenomenon that may occur for intermediate lengths (TOMBLIN and BARBERO, 1994, ZUREICK and SCOTT, 1997).

2.5. Perfect Members

Perfect columns are defined as initially perfectly straight members subject to concentric compression force P (TIMOSHENKO and GERE, 1961). In this case, the structural member, initially in a stable equilibrium, remains in this condition for low compression loads. As P increases, the member stiffness reduces gradually until vanishing when P reaches certain value, called ‘critical load’. This one is “*directly related to the load carrying capacity of the member*” (BARBERO and TOMBLIN, 1993) and represents a stability limit (bifurcation point). Beyond this point, the straight configuration corresponds to unstable state of equilibrium and a slight disturbance produces large lateral deflections displacements, changing the original shape (buckling).

Similarly, this concept can be extended to plates. According to LEISSA (1985), plate buckling behavior may be discussed in terms of a plot P (load) *versus* w (out-of-plane displacement measured at a representative point on the plate), presented in Figure 2.10b. The curve *I* illustrate the fundamental path and is analogue to the column buckling problem discussed in the previous paragraph, *i.e.*, a perfectly flat plate will remain flat in a stable equilibrium configuration while the load P increases from zero to the critical load (P_{cr}). After this value, the plate may theoretically continue the fundamental path defined by curve *II* in an unstable equilibrium condition, or may follow an alternative stable post-buckling path given by curve *IV*, in which the plate experiences large deflections with increasing loads. Typically, plates are able to carry loads beyond the P_{cr} due to their ability in

redistributing stress towards stiffer regions (nonlinear analysis). If the stress redistribution is neglected (linear analysis), the post-buckling path is described nearly as the horizontal plateau III.

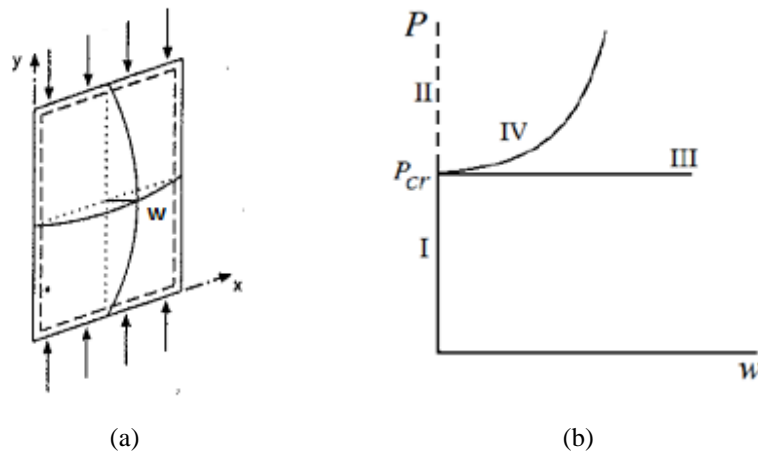


Figure 2.10 – (a) Compressed plate (Adapted from REIS and CAMOTIM, 2001) ; (b) Representative curves of load versus transverse displacement (Adapted from LEISSA, 1985)

A perfect column subject to concentric compression may, therefore, exhibit the following failure modes: *crushing* (Figure 2.11a), *Euler buckling (global buckling)* (Figure 2.11b) or *local buckling* (Figure 2.11c). The first corresponds to any failure that may occur at the constituent material level (CARDOSO, 2014), whereas the other two correspond to the instability limit states and are described in the following sections.

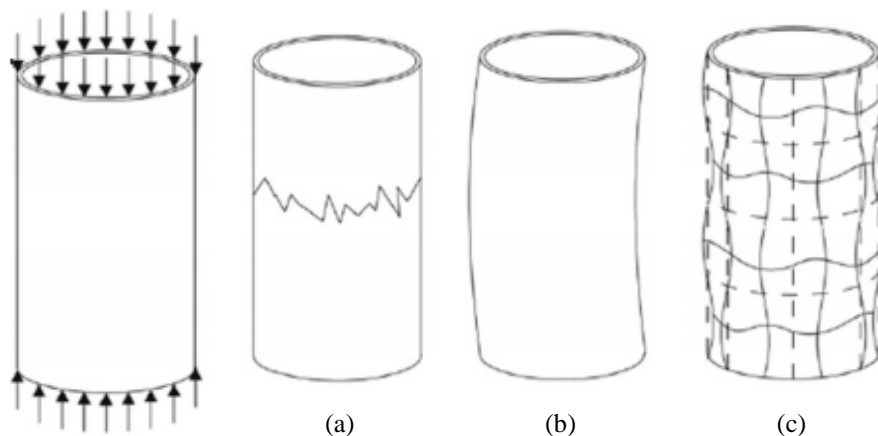


Figure 2.11 - Failure modes on axial compression: (a) crushing; (b) global buckling; (c) local buckling (LAU, SAID and YAAKOB, 2012)

2.5.1. Global Buckling

Global buckling is likely to occur for long columns and is characterized by a single half-wavelength overall mode shape (MOTTRAM, 2004) while the cross section remains unchanged, as shown in Figure 2.12. The most important global buckling modes of I-section columns are *flexural* and *torsional* buckling. According to ZIEMIAN (2010), the flexural buckling mode is the dominant mode experienced by doubly symmetric sections, which are the subject of this work.

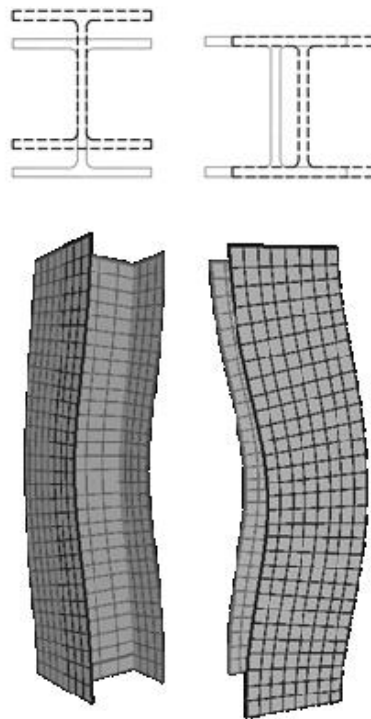


Figure 2.12 – Flexural Global Buckling

The flexural buckling mode corresponds to the classical problem investigated by Euler, in which a column assumes a bent deflected shape during buckling. The Euler's critical stress can be determined after solving the differential equilibrium equation for the deformed column and is given according to Eq. 2.8:

$$F_e = \frac{\pi^2 E_L}{(K_e L/r)^2} \quad (2.8)$$

where L is the column length, r is the radius of gyration with respect to the minor axis, E_L is the flexural modulus of elasticity, and K_e is the effective length factor for

centrally columns depending on the idealized end conditions, as presented in Figure 2.13.

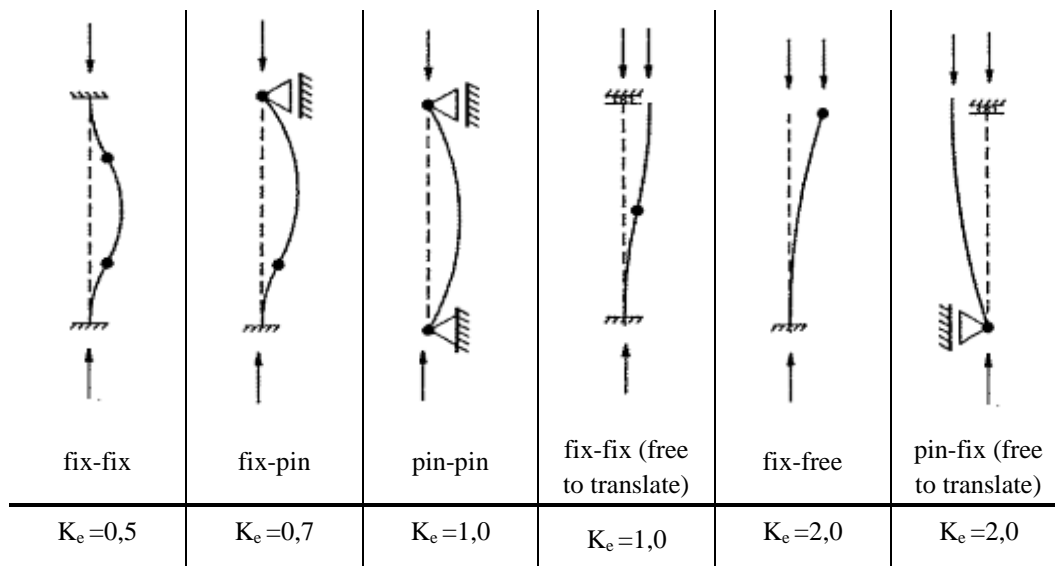


Figure 2.13 - Effective lengths of columns (Adapted from REIS and CAMOTIM, 2001)



Nevertheless, polymer composites generally have a very low shear modulus with respect to the longitudinal one and the influence of transverse shear deformation needs to be considered (ZUREICK and SCOTT, 1997). Two different flexural buckling formulae accounting for shearing effects have been independently derived by ENGESSER (1889) and, then, by HARINGX (1942) (*apud* BAZANT, 2003), respectively reproduced in Eqs. 2.9 and 2.10. According to TIMOSHENKO and GERE (1961), Eq. 2.10 is more accurate, although Eq. 2.9 is more often considered for pGFRP columns.

$$F_{cr} = \frac{F_e}{1 + n_s F_e / G_{LT}} \quad (2.9)$$

$$F_{cr} = \frac{\sqrt{1 + 4n_s F_e / G_{LT}} - 1}{2 n_s / G_{LT}} \quad (2.10)$$

where G_{LT} is the in-plane shear modulus, n_s is the form factor for shear that varies with cross section and F_e is the Euler's stress given by Eq. 2.8. The values for n_s for I-sections are shown in Table 2.5 (ZUREICK and SCOTT, 1997).

Table 2.5 - Shear form factors for I-sections

	
Bending about 1-1 axis	Bending about 2- 2 axis
$n_s = A_g/A_w$	$n_s = 1,2 A_g/A_f$

A_g - gross cross sectional area

A_f - area of flanges

A_w - area of web

Many authors have investigated global buckling and have shown that Eq. 2.8 is appropriate for pGFRP long columns (defined according their slenderness and presented in section 2.6.2). ZUREICK and SCOTT (1997) compared experimental results from tests conducted on long columns with those theoretically obtained with Eqs 2.8 and 2.9. The authors concluded that Euler's buckling load equation is quite suitable to predict results, finding average differences of 8% for loads predicted by Eq. 2.8 and 6% for the ones predicted by Eq. 2.9. BARBERO and TOMBLIN (1993) also found a maximum difference of 6.2% between Euler's equation prediction and experiments. BARBERO and DeVIVO (1999) conducted tests and have shown that the shear correction does not cause a significant reduction (less than 4% for WF sections) for weak-axis buckling critical loads even for intermediate lengths (also defined in section 2.6.2). CARDOSO *et al.* (2014), on the other hand, conducted tests on square tube columns having different lengths and concluded that shear may affect significantly the prediction for short to intermediate columns.

2.5.2. Local Buckling

Local buckling is characterized by the loss of the original cross section shape (Figure 2.14) and is more likely to occur in short columns. In this mode, the lines defined by the intersection of constituent plates remain straight during buckling and half-wave length is the same order of magnitude as the cross-section dimensions.

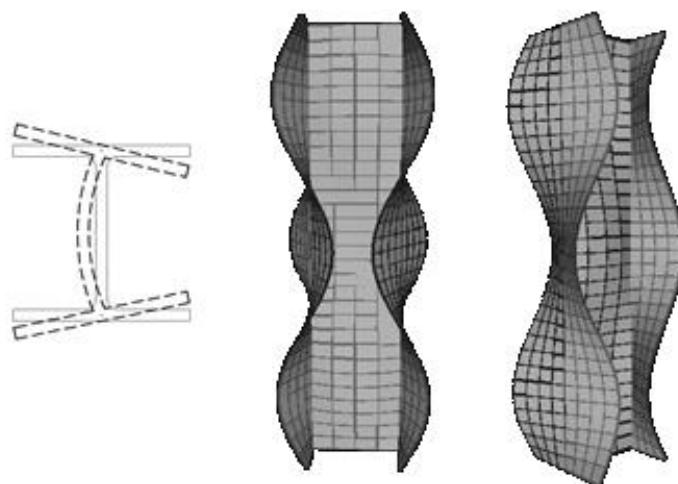


Figure 2.14 - Local buckling of a short I-section column

Local buckling of plates comprised of orthotropic material has been studied by many authors in order to obtain closed-form equations for the problem. The equations derived by LEKHNITSKII (1968) for plates having different end conditions have been, for long time, adopted to study local buckling of FRP sections. Under the conservative assumption that plates are hinged at section junctions, these equations are still incorporated in many standards and guidelines, such as the *EUROCOMP Design Code and Handbook* (CLARKE, 1996), the *ASCE Pre-Standard for Load and Resistance Factor Design (LRFD) of Pultruded Fiber Reinforced Polymer (FRP) Structures (Final)* (ASCE, 2010) and the *Prospect for new guidance in the design of FRP: Support to the implementation, harmonization and further development of the Eurocodes* (ASCIONE *et al.*, 2016). More recently, different approaches considering interaction between constituent plates have been used by authors to derive explicit equations (*e.g.* KOLLAR, 2013). CARDOSO *et al.* (2015) assumed an approximate buckled shape to derive an equation for the local buckling critical stress of I-section members (F_{cr}), reproduced in Eq. 2.11. The authors compared the prediction of this equation with those obtained using finite strip method (FSM) and obtained a maximum difference up to 6% for typical FRP properties and cross-section dimensions. It is important to mention that this equation was obtained for relatively long columns, in which end-conditions do not play an important role.

$$F_{cr} = k_{cr} \frac{\pi^2 E_{L,f}}{12(1 - \nu_{LT}\nu_{TL})} \left(\frac{1}{b_w}\right)^2 \quad (2.11)$$

$$k_{cr} = \frac{2}{\sqrt{1 + \pi^2 \eta^3 / 3}} \sqrt{\frac{E_{T,f}}{E_{L,f}}} + \frac{2 \nu_{LT} \frac{E_{T,f}}{E_{L,f}} + 4(1 + 4\eta)(1 - \nu_{LT}\nu_{TL}) \frac{G_{LT}}{E_{L,f}}}{(1 + \pi^2 \eta^3 / 3)} \quad (2.12)$$

in which k_{cr} is critical buckling coefficient, $E_{L,f}$ and $E_{T,f}$ are the longitudinal and transverse flexural moduli, G_{LT} is the shear modulus, t is the plate thickness, η is the flange-to-web width ratio b_f/b_w , b_w is the section depth, ν_{LT} is the major in-plane Poisson's ratio and ν_{TL} is the minor in-plane Poisson's ratio.

A review of previous experimental studies on local buckling is presented in section 2.9.

2.5.3. Signature Curve

The signature curve consists in a plot of the critical load *versus* member length. It is unique for each structural member and provides the 'distance' between local (LB) and global buckling (GB) modes. In Figure 2.16, an illustrative example is presented for an I-section column (101.6x101.6x6.4-mm) with typical pGFRP properties and different boundary conditions for *columns* (pinned and fixed at both ends – Figure 2.15a and for *plates* (clamped and simply-supported at both ends – Figure 2.15b).

In Figure 2.16, it can be noticed that length and end-conditions have strong influence on the critical load P_{cr} . For shorter columns, local buckling (solid lines) dominates the behavior whereas global buckling (dashed lines) is the governing buckling mode for longer members. It is important to note that the local buckling portion of the curve is related to plate bending and therefore depends on the *flexural modulus* and *plates* end conditions, while global buckling is influenced by *compressive modulus* and *column* ends.

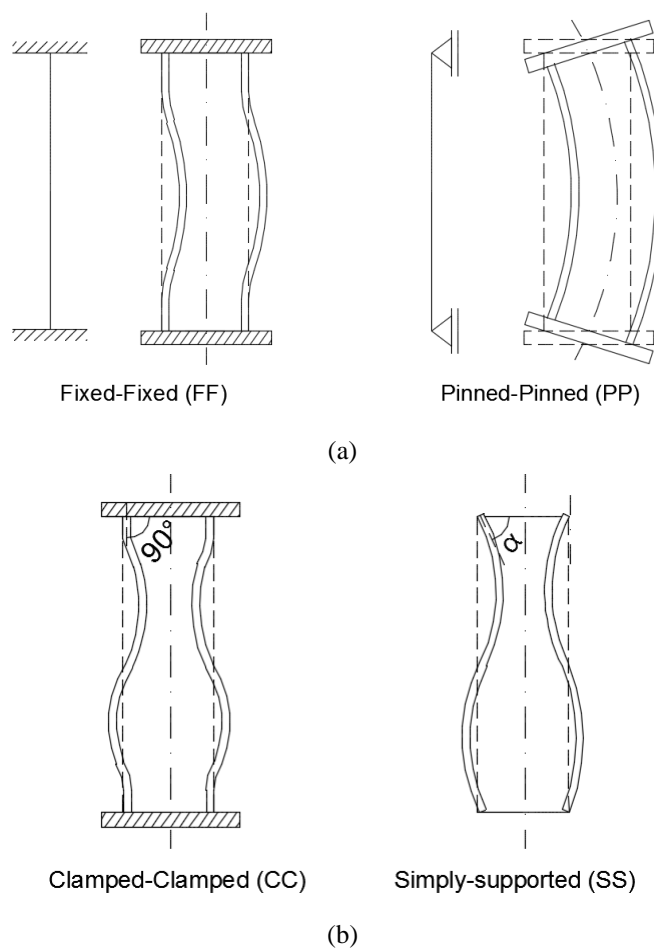


Figure 2.15 - Columns and plates end-conditions for an I-section: (a) columns end-condition; (b) plates end-condition

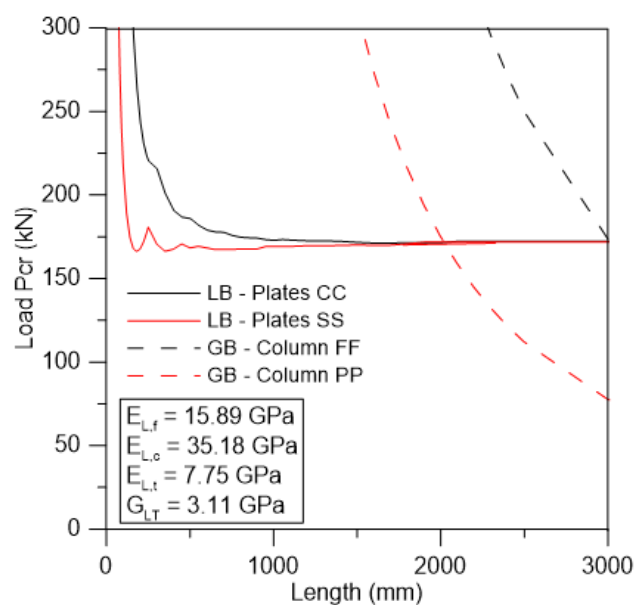


Figure 2.16 - Illustrative signature curve for given cross section, material properties and different boundary conditions.

By analyzing the local buckling curves in the example of Figure 2.16, it can be noticed that columns with clamped edges (CC) tend to exhibit greater critical loads than those with simply-supported plates (SS). As length increases, multiple half-waves are formed and the influence of end-conditions reduces until a certain length for which critical loads for SS or CC plates become similar. This can be easily observed by comparing different columns length: for short columns with 400 mm, the LB critical loads for CC and SS columns are 190.4 kN and 170.4 kN, respectively. Whereas for long columns with 1200 mm, the LB critical loads for both end-conditions are much closer, being 172.6 kN for CC plates and 168.5 kN for SS ones.

The global buckling curves show that critical loads are lower for pin-ended columns (PP) than for fixed-ended ones (FF). As will be discussed in the next sections, columns with base rotations restrained (FF) are preferred in order to provide appropriate distance between LB and GB critical loads and, thus, to avoid buckling interaction.

The signature curve can be obtained analytically or by using numerical methods such as Finite Strip Method (FSM) or Generalized Beam Theory (GBT) (SCHARDT, 1994). Both have been widely used to investigate the buckling behavior of cold-formed steel members. The conventional FSM employs only SS boundary conditions, but LI and SCHAFER (2010) has extended it to general ones, by implementing shape functions and deriving the elastic and geometric stiffness matrices. In GBT, SCHARDT derived an equation where plate element contribution is considered within beam geometric stiffness. To do so, buckling mode is decomposed into a linear combination of cross-section deformation modes, offering the possibility to obtain the contribution of each one into the final buckling mode.

In this work, GBT is used to accurately predict critical loads for each length, through software *GBTUL 2.0*.

2.6. Real Columns and Plates

Real columns are not initially perfectly straight, due to geometric and material imperfections. As shown in Figure 2.17, real columns experience lateral deflections since the beginning, growing more quickly as the applied load P approaches the critical load P_{cr} . Therefore, a sudden bifurcation buckling studied for perfect members cannot be seen in this case. In fact, a column subjected to compression forces undergoes continuous displacements, originated from second order bending moments, reducing the load carrying capacity of the member in comparison with perfect columns. In this case, a strict stability limit does not exist and the stiffness reduction is a gradual process. The smaller the initial imperfections, closer from theoretical perfect column is the actual behavior.

The behavior of real (or perfect) plates is analogous to the columns, but there are dissimilarities with respect to the post-critical path, which is addressed in section 2.7.

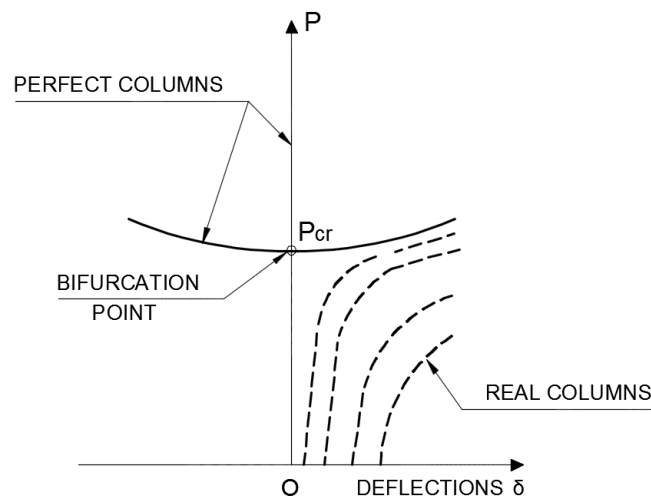


Figure 2.17 – Perfect and real columns behavior

In metallic materials, imperfections such as residual stresses and plasticity, when combined, may also affect the actual behavior, leading to yielding that reduces the apparent member stiffness or to premature failure. Therefore, real column problems require non-linear analysis in order to evaluate the effects of the imperfections on the member strength and behavior. It is not the case of GFRP composites, which exhibit elastic-linear behavior and no material non-linearity needs to be taken in account.

2.6.1. Initial Geometric Imperfections

As any other production process, pultrusion produces inevitable imperfections in the final composite profile. According to TOMBLIN and BARBERO (1994), these imperfections are very difficult to control and will have a considerable influence on any buckling test. According to CARDOSO (2014), the geometric imperfections of columns may be associated to the member length or to the size of the cross-section. The former is called *initial out-of-straightness* or *crookedness* and may be estimated as a fraction of the column length L (usually $\delta_0 < L/500$). Whereas the latter is called *initial eccentricity* and can be estimated as a fraction of section size. This eccentricity can be associated with a shift in the geometric center due to non-uniform fiber distribution throughout cross section, as well as loading eccentricity. Plates also present analogous imperfections and the manufacturers estimate the *out-of-straightness* as $\Delta_0 < b/125$, in which b is the plate width. Plates may also present *intrinsic imperfections*, that are usually related with its thickness variation or misalignment of fibers. Figure 2.18 illustrates initial imperfections in columns and plates.

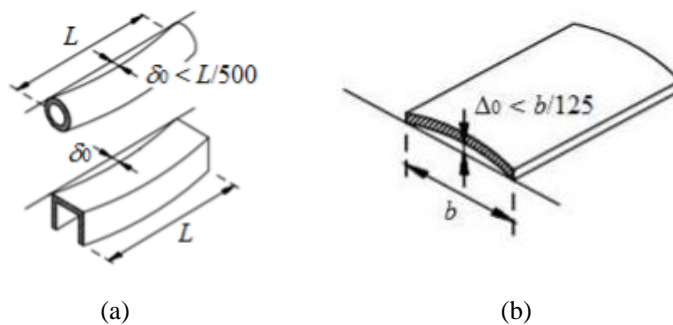


Figure 2.18 - Initial geometric imperfections in columns and plates (CARDOSO, 2014): (a) out-of-straightness in columns; (b) out-of-straightness in plates

2.6.2. Failure Modes of Real Columns

In real columns, the interaction between buckling modes and crushing may occur, depending on the 'distance' between their respective isolated limit values. In such case, there is a significant reduction in the ultimate load if compared to perfect columns or real ones that are governed by single modes. This occurs due to

additional bending stresses in plates in the column bent configuration, leading to premature occurrence of local buckling and, therefore, to a reduction in stiffness that affects the overall behavior. Figure 2.19 presents the expected behavior for a thin-walled column failing by coupled buckling mode (global and local buckling). From the graph shown in the Figure, the reduction of the load-carrying capacity of the real column with respect to the prediction for perfect members can be observed.

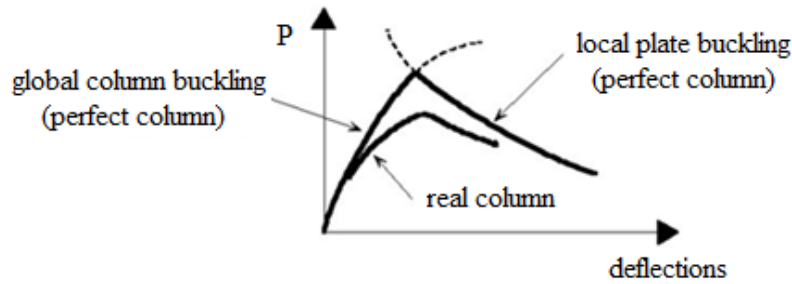


Figure 2.19 – Reduction of ultimate load caused by interaction mode (ESDEP, 2017)

When studying local buckling behavior, column lengths must be selected in a way that local buckling critical loads are ‘far enough’ (lower) from crushing load to allow sufficient out-of-plane deflections, as well as from global buckling critical load, to avoid influence of overall bending stresses. An interesting method to evaluate if the ‘distances’ between local buckling and other individual failure modes (global buckling and crushing) are appropriate is by using a ‘map’ in which global slenderness (λ_g) is plotted against the local slenderness (λ_l), given in Eqs 2.13 and 2.14 (CARDOSO *et al.*, 2014).

$$\lambda_g = \sqrt{\frac{F_{PP}}{F_{crg}}} = \sqrt{\frac{\min\{F_{L,c}, F_{crl}\}}{F_{crg}}} \quad (2.13)$$

$$\lambda_l = \sqrt{\frac{F_{L,c}}{F_{crl}}} \quad (2.14)$$

where $F_{L,c}$ is the material crushing strength, F_{crg} is the global critical stress and F_{crl} is the local buckling critical stress, F_{PP} is the perfect plate compressive strength, defined as the lesser value between $F_{L,c}$ and F_{crl} .

Column classification and expected failure modes can be predicted according to slenderness combination, as shown in Table 2.6. According to this Table, for instance, the column must have a relatively slender section and be relatively short for a successful local buckling test.

Table 2.6 - Classification of columns and plates with their expected failure modes (CARDOSO *et al.*, 2014)

$\lambda_l \backslash \lambda_g$	Short ($\lambda_g \leq 0.7$)	Intermediate ($0.7 < \lambda_g < 1.3$)	Long ($\lambda_g \geq 1.3$)
Compact ($\lambda_l \leq 0.7$)	Crushing	Interaction between crushing and global buckling	Global buckling
Intermediate ($0.7 < \lambda_l < 1.3$)	Interaction between crushing and local buckling	Interaction between crushing, local and global buckling	Global buckling
Slender ($\lambda_l \geq 1.3$)	Local Buckling	Interaction between local and global buckling	Global buckling

2.7. Post-Buckling Behavior of Plates

As previously mentioned, plates behavior is analogous to columns. Both present the same bifurcation-type buckling (symmetric and stable) with similar behavior when approaching the critical load, also presenting the same response to imperfections. However, dissimilarities are observed with respect to the post-buckling behavior, as can be seen in Figure 2.20, which presents the load (P) *versus* deflections (w) plot for columns and plates for different values of initial imperfections. In the graph, the perfect and real structures are illustrated by solid and dashed lines, respectively. As can be noticed, columns are usually characterized by a flatter post-critical path, whereas the plates present a large postcritical reserve of strength. Usually, the final collapse of plates occurs at loads 50-100 percent larger than the critical load. In plates simply supported along four edges, it may be explained by their capacity “to redistribute the initial compressive in-plane forces, transferring them from the middle of the plate into strips along the edges, or from compressed diagonal strips into tensioned diagonal strips” (BAZANT and

CEDOLIN, 2010). A similar behavior can be observed for other boundary conditions, where in-plane forces migrate to stiffer regions of the plate.

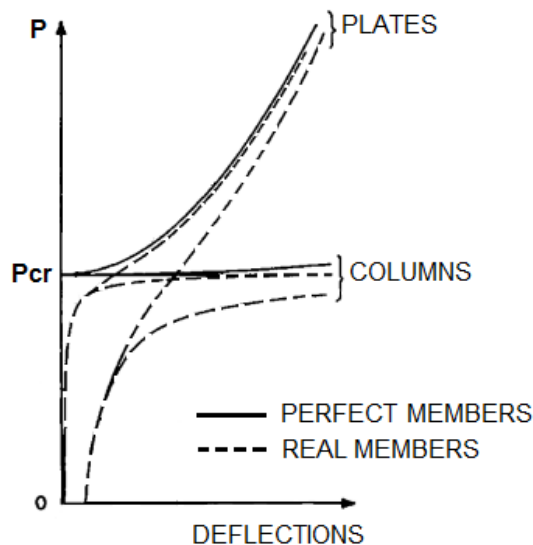


Figure 2.20 – Plates behavior (Adapted from BAZÄNT and CEDOLIN, 2010)

With respect to the experimental local buckling studies, the influence of the post-critical path has been discussed by many authors (*e.g.* SPENCER and WALKER, 1975, BARBERO and TROVILLON, 1998, BAZANT and CEDOLIN, 2010). The most usual method adopted in order to determine the experimental local buckling critical loads in pGFRP columns is the Southwell plot (SOUTHWELL, 1932), although it has been developed to study Euler buckling. The Southwell plot consists in linearizing the hyperbolic curve P versus displacements δ (or w) in a δ versus δ/P curve and the critical load P_{cr} is obtained as the slope of the linear portion of the plot. The method accounts for existing imperfections due to manufacturing process and does not require the critical load to be reached (BARBERO and TOMBLIN, 1993, TOMBLIN and BARBERO, 1994). However, according to BAZÄNT and CEDOLIN (2010), this method is not the most appropriate for structures with post-critical reserve of carrying capacity, such as plates. The post-buckling behavior of plates is completely different from the hyperbolic relationship predicted by Southwell plot, affecting its linearity (SPENCER and WALKER, 1975), as shown in Figure 2.21.

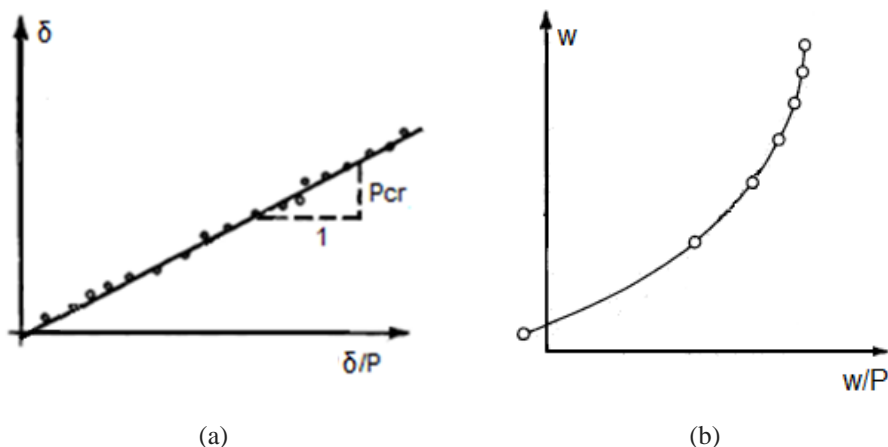


Figure 2.21 - Southwell plots: (a) for Euler columns (Adapted from BAZANT and CEDOLIN, 2010); (b) for plates (Adapted from SPENCER and WALKER, 1975)

The same is stated by BARBERO and TROVILLON (1998), that reported that this technique assumes a flat post-buckling path, thus not taking into account the stiffening of the system due to the post-critical path (nonlinear stress distribution throughout section). Although this effect is negligible for Euler columns, it may be considerable in local buckling, leading to artificially high critical loads, as observed in this work. The authors, as well as SPENCER and WALKER (1975) proposed alternative method for experimental local buckling critical loads prediction (which will not be discussed in this work), but the Southwell plot is still the most usual adopted method.

2.8. Strength Curve

Another important tool to assess column performance is the so-called strength curve, that correlates the member slenderness (λ) with its strength (F_u) (F_u versus λ plot).

Strength curves for GFRP may be obtained for single plates and for columns comprised of real plates and provides a clear understanding on how interaction of individual failure modes reduces the ultimate load with respect to the one expected for a perfect member. Usually, it is presented in a convenient normalized form, in which the slenderness $\lambda_1=1$ marks the transition point between two distinct modes, as can be seen in Figure 2.22.

TOMBLIN and BARBERO (1994) were the first to propose a strength curve for GFRP columns considering buckling interaction. They proposed an empirical equation based on a typical expression used for timber structures (Zahn's equation), where the ultimate strength (F_u) is determined according to the relative column slenderness λ_c . A constant c was suggested to account the degree of interaction between buckling modes. Since then, alternative equations describing the compressive strength behavior in GFRP columns have been proposed (e.g. SEANGATITH and SRIBOONLUE, 1999, PUENTE *et al.* 2006, CARDOSO *et al.*, 2015). However, all these equations are applied to columns. For a plate with negligible post-buckling behavior, CARDOSO *et al.* (2015) derived Eq. 2.15 after combining Classical Plate and Stability Theories.

$$\chi_l = \frac{F_u}{F_{L,c}} = \frac{1 + \alpha_l + \lambda_l^2 - \sqrt{(1 + \alpha_l + \lambda_l^2)^2 - 4\lambda_l^2}}{2\lambda_l^2} \quad (2.15)$$

where α_l is an imperfection factor usually determined experimentally; F_u is the ultimate strength; $F_{L,c}$ is material crushing strength and λ_l is the plate slenderness, given in Eq. 2.14.

For real columns comprised of imperfect plates, CARDOSO *et al.* (2015) presented another equation where χ_l is an input parameter, corresponding to the plate strength. However, as mentioned previously, the bending stresses associated with the global buckling behavior are negligible in short columns and the complete equation presented in the above referred work reduces to Eq. 2.15. Figure 2.22 presents a normalized strength curve obtained from Eq. 2.15. The solid line represents the theoretical strength for a perfect member concentrically loaded, while the dashed line represents the strength expected for a real member, accounting for initial imperfections.

As can be seen, for a column with a greater slenderness ($\lambda_l > 1$), the failure occurs by 'pure' local buckling (presented by the hyperbola $\chi_l = 1/\lambda_l^2$), once the critical load stress F_{cr1} is smaller than the limit of the material strength $F_{L,c}$. On the other hand, for a column with a lower slenderness ($\lambda_l < 1$), failure is dominated by crushing. Finally, for columns with slenderness within the transition mark $\lambda_l = 1$ neighborhood, failure is characterized by interaction between the two modes.

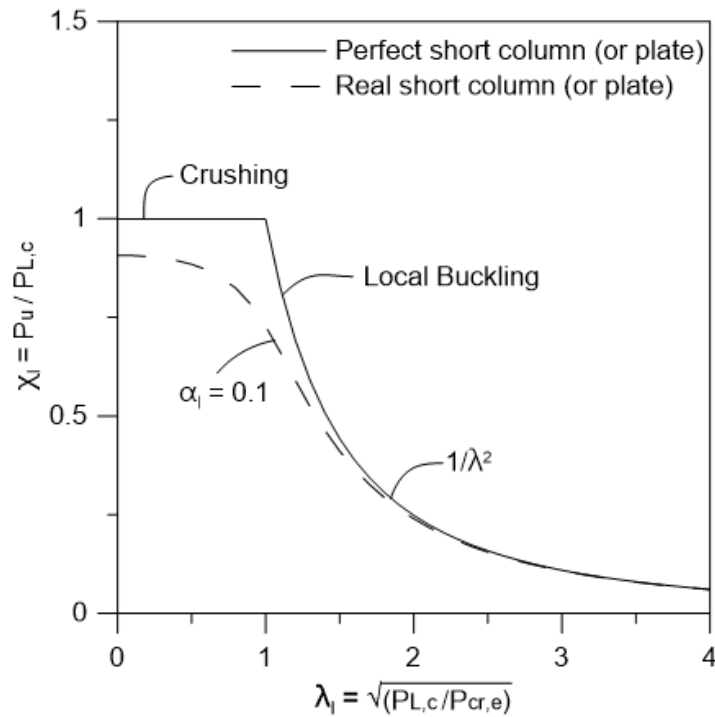


Figure 2.22 - Normalized strength curve

2.9. Previous Experimental Researches on Local Buckling of I-Sections

Appropriate and well-controlled end-conditions need to be ensured on local buckling tests. It is important to evaluate not only the *column*, but also the *plates* ends, as described previously in section 2.5.3. A thorough review was presented by MOTTRAM (2004), who presented the outcomes of relevant previous studies on the local buckling of I-sections. The author has compared results obtained analytically, experimentally and numerically and has shown that a greater attention must be devoted to the actual boundary conditions.

TOMBLIN and BARBERO (1994) presented one of the first known works dedicated to study the local buckling behavior of different pGFRP I-sections (102x102x6.4-mm; 152x152x6.4-mm; 152x152x9.5-mm; 203x203x9.5-mm) by performing stub column tests. The lengths were selected in order to reproduce 2, 3 or 4 half-waves. The differences between experimental results and theory were found by the authors to be less than 11%, 9% and 24% for columns having 2, 3 and 4 half-waves, respectively. The largest difference observed for columns with 4 half-

wavelengths was justified by the occurrence of interaction between global and local buckling modes. The theoretical critical loads were predicted using an analytical solution described in BARBERO and RAFTOYIANNIS (1990) and estimated material properties. The Southwell method (SOUTHWELL, 1932) was used to obtain the experimental critical loads.

YOON (1993) has also tested different I-sections columns (305x305x12.7-mm; 254x254x12.7-mm; 254x254x9.5-mm; 203x203x12.7-mm; 203x203x9.5-mm; 152x152x12.7-mm and 152x152x9.5-mm) with lengths corresponding to 5 to 8 half-wavelengths. The Southwell method was used and the theoretical predictions were made based on a linear finite-element (FE) analysis and on the LEKHNITSKII (1968) equation for a plate with one free and one simply supported unloaded edges. Although simple, the disadvantage of this equation is that it does not account for the restraint provided by the web-flange junction. According to McCARTHY and BANK (2011), the web-flange junction rotational stiffness is relevant in columns, accounting for 35% of the local flange buckling resistance. Therefore, a better correlation with experimental results is achieved when modeling the web-flange junctions as rotationally restrained.

TURVEY and ZHANG (2006) tested 101.6x101.6x6.25-mm I-sections with column lengths varying from 200 to 800 mm. To predict the initial buckling loads and pre- and post-buckling responses, non-linear FE (NL-FE) analyzes were carried out. Linear analyzes (eigenvalue) were also conducted for comparison. According to the authors, this may help to identify the regions that first exhibit nonlinearities and the load level at which the non-linear response starts. It was observed that the NL-FE analyzes predicted critical loads 3% to 7% greater than those from eigenvalue analyzes. After determining experimental loads using Southwell plot, the authors concluded that NL-FE predictions ranged from 7% greater to 6% lower than those obtained experimentally. On the other hand, the linear analyzes led to differences ranging from 2% greater to 11% lower than experiments. Therefore, the results did not present a significant difference when comparing linear and non-linear analysis.

PECCE and COSENZA (2000) tested 203x203x9.5-mm I-sections columns with lengths equal to 500 mm and used the Finite Element Method to evaluate the critical stresses obtained on the experimental tests. A maximum difference of 18%

was reported between the numerical and experimental results. The results were concluded to be in good agreement with theory, once the uncertainties of the moduli of elasticity and the plates end-conditions were not taken into account. The authors also developed an expression of the buckling curve, considering the restraint action of the web on the flange. The analytical curve proved to be in good agreement with the experimental results. However, when the failure mode is governed by local buckling, the proposed curve is not always safe and may be considered too conservative.

As can be seen in the previous paragraphs, works have been focused in the investigation of doubly symmetric WF I-shaped sections having flange width equal to their section depth, *i.e.* $b_f/d=1.0$. According to MOTTRAM (2004), ‘square’ I-sections with high outstanding-to-thickness ratio (b_f/t_f) are more susceptible to local flange buckling. A few works have tested sections with other flange-to-web width ratios, *e.g.* DI TOMASSO and RUSSO, 2003 and CARDOSO *et al.*, 2015. It is important to point out that DI TOMASSO and RUSSO (2003) addresses effective buckling behavior, interaction between buckling modes and types of failure, not focusing specifically on local buckling of pGFRP columns.

CARDOSO *et al.* (2015) performed tests in I-sections with b_f/d equal to 0.5, 0.75 and 1.0 and column lengths varying from 152 to 400 mm. The theoretical local buckling critical loads were predicted by analytical solution proposed by the authors and the experimental loads were determined through Southwell method. In average, the experimental results were 19.7% greater than those calculated by the proposed equation. This may be due to inaccuracy of Southwell plot for the small deflections exhibited by columns with b_f/d equal to 0.50 and to transverse shear effect, which has shown to be relevant when the ratio of the flange width-to-thickness (b_f/t) is lower than 13 (BARBERO, 2010). Additionally, they attributed the difference to the restraint of rotation provided by end plates, as will be discussed in the following paragraphs.

In all the tests mentioned previously, the machined parallel ends of the columns were simply put in contact with the base plates of the universal testing machines, which are restrained from rotation themselves (FF end condition for the column). Nevertheless, these tests fixture neither reproduce clamped nor simply-supported for the *plates* end conditions. In fact, according to CARDOSO *et al.*

(2015), this solution implies that the plates rotation is followed by a shift in the reaction force, causing a restoring eccentricity that apparently increases critical load during test. This effect is shown in Figure 2.23 and may be more important for thicker plates.

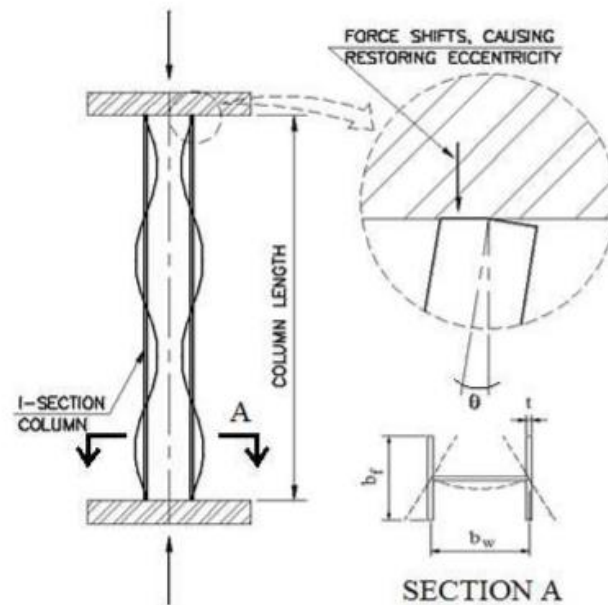


Figure 2.23 - Restoring eccentricity caused by end conditions (CARDOSO *et al.*, 2015)

These adopted boundary conditions may have contributed to the significant differences found between shorter and longer columns critical loads, observed by TOMBLIN and BARBERO (1994), TURVEY and ZHANG (2006) and CARDOSO *et al.* (2015). Additionally, as discussed in the previous sections, greater critical loads may be observed for shorter columns and this is more pronounced if column length is not an integer multiple of its critical half-wave length. The alternative, in this case, is to adopt a longer column, allowing development of multiple half-waves, but carefully avoiding coupled buckling that may reduce significantly the load-carrying capacity.

BARBERO and TROVILLION (1998), on the other hand, reported different end-conditions for plates and columns. The panels were clamped in an attempt to introduce a simply-supported end-condition. Whereas from a global point of view, the columns were fixed at both ends. The authors conducted local buckling tests in three I-section columns having 304.8x304.8x12.7-mm and lengths corresponding to three local buckling half-waves. It is important to point out that the material

properties were obtained by using the lay-up information from manufacturing process. As previously mentioned, this work brings a relevant discussion about the influence of plates post-buckling behavior in the theoretical and experimentally determined critical loads. Therefore, in order to account the curvature of the post-critical path on the P_{cr} prediction, a computer code (FEM) based on perturbation techniques was developed, whereas the experimental critical loads were determined by a quadratic approximation of the post-critical path, proposed by the authors. The numerical predictions were within 9.3% of the experimental critical loads and were considered quite accurate.

Table 2.7 presents a summary of previous local buckling tests conducted on I-sections, with the end-conditions adopted by each author, as well as the properties, sections ($d \times b_f \times t$), lengths L and methods for determining theoretical and experimental critical loads ($F_{cr,t}$ and $F_{cr,e}$).

Table 2.7 - Summary of I-section local buckling tests conducted in previous works

<i>Previous Works</i>	<i>Section</i>	<i>L</i>	<i>Ends</i>		<i>E_L</i>	<i>E_T</i>	<i>G_{LT}</i>	<i>F_{L,C}</i>	<i>Method for:</i>	
	<i>d x b_f x t</i> (mm)	(mm)	L	G	(GPa)	(GPa)	(GPa)	(MPa)	<i>F_{cr,e}</i>	<i>F_{cr,t}</i>
Yoon (1993)	305x305x12.7	1524 - 3048	U	FF	16.5 - 18.1	8.6 - 10.5	3.6 - 4.5	207**	S	FEM-L / Lekhnitskii
	254x254x12.7	1524 - 2438								
	254x254x9.5	1524 - 2438								
	203x203x12.7	1524								
	203x203x9.5	1524 - 2438								
	152x152x12.7	914								
	152x152x9.5	892 - 1219								
Tomblin and Barbero (1994)	203x203x9.5	495 - 1003	U	FF	19.5 - 21.5*	9.1 - 10*	3.1 - 3.3*	228**	S	Proposed
	152x152x9.5	394 - 775								
	152x152x6.4	381 - 762								
	102x102x6.4	267 - 546								
Barbero and Trovillion (1998)	304.8x304.8x12.7	1816 1499 1511	CC	FF	NR	NR	NR	482	Prop.	Proposed
Pecce and Cosenza (2000)	203x203x9.5	500	U	FF	22	7.5	2.4	207**	NR	FEM-L
Turvey and Zhang (2006)	102x102x6.4	200 - 800	U	FF	22.1	10.1	3.7	280	S	FEM-L / FEM-NL
Cardoso et al. (2015)	102x102x6.4	400	U	FF	19.5 - 21.9	9.4 - 12.2	4.1 - 4.7	277 - 429	S	FSM / Proposed
	102x76x6.4	400								
	102x51x6.4	266								
	76x76x6.4	305								
	76x51x6.4	305								
	76x38x6.4	152								

U = undefined; FF = fixed-fixed; S = Southwell; MS= modified Southwell; NR = not reported; FEM-L = FEM, linear; FEM-NL = FEM, non-linear; FSM = finite strip method; Prop/Proposed = equations and methods proposed by authors; *not obtained experimentally; **manufacturer data;

Figure 2.24 presents a local *versus* global slenderness map, showing the classification of I-section columns tested in previous works, according to Table 2.6. As can be observed in the Figure, most of tested columns are classified as short

columns with slender sections, fitting in the region governed by local buckling failure mode.

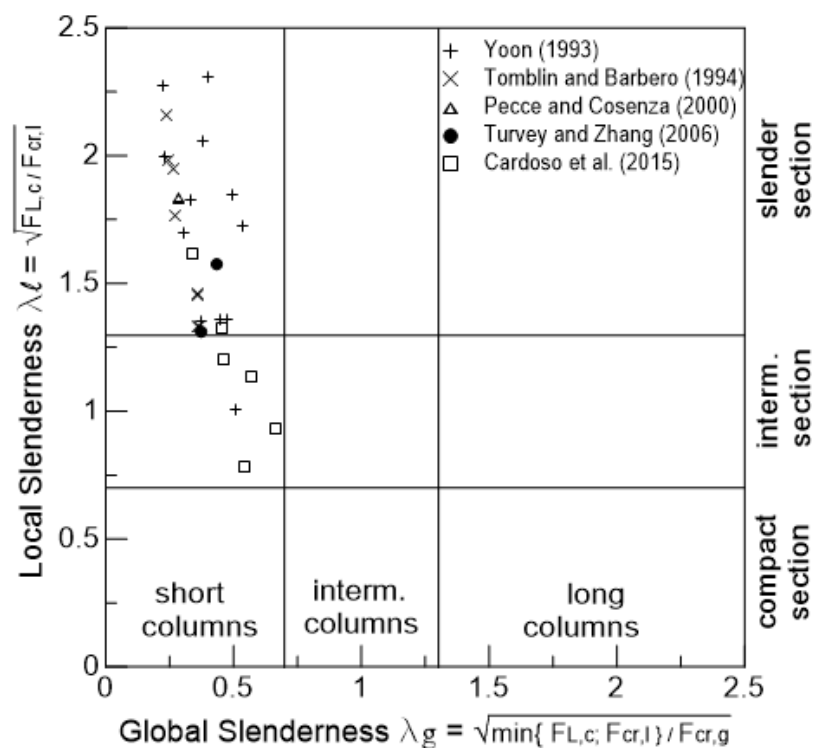
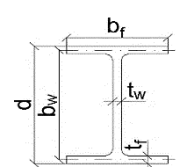


Figure 2.24 - local *versus* global slenderness map of previous studies

In summary, the remaining gaps are shown more clearly in Table 2.8, where the lengths, end-conditions and cross-section geometries (b_f/d) adopted in previous studies are presented. This work aims to contribute fulfilling some of these gaps, by testing columns with different end-conditions and flange-to-depth ratio. Further, to gather information about the stiffening of the system discussed in section 2.7, the nonlinear strains distribution throughout cross section is investigated.

Table 2.8 - Length, flange-to-depth ratio and end-conditions adopted on previous studies



		Yoon (1993)	Tomblin and Barbero (1994)	Barbero and Trovillion (1998)	Pecce and Cosenza (2000)	Turvey and Zhang (2006)	Cardoso <i>et al.</i> (2015)	Present Study
Lengths		892-3048	267-1003	1511-1816	500	200-800	152-400	300-600
End- condition	CC ⁽¹⁾			x				x
	SS ⁽²⁾							x
	CB ⁽³⁾	x	x		x	x	x	x
b/d	0.5						x	x
	0.75						x	x
	1.0	x	x	x	x	x	x	x
Strains distributions ⁽⁴⁾								x

(1) Plates clamped at both ends

(2) Plates simply supported at both ends

(3) Plates simply in contact with base plates at both ends

(4) Investigation on nonlinear strains distribution throughout cross section

3. Experimental Program: Local Buckling of I-Sections

3.1. Overview

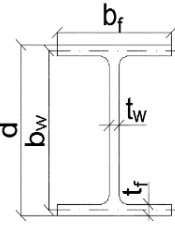
An experimental program addressed to the local buckling behavior of I-sections columns was conducted at the Structures and Materials Laboratory of Civil and Environmental Engineering Department at PUC-Rio (LEM/DEC). The GFRP profiles used in the investigation were all manufactured and supplied by the same Brazilian company: COGUMELO. Relevant material properties were obtained experimentally and stub columns with different cross-section dimensions and overall lengths were tested under concentric compression. In the tests, the *column* bases were fixed at both ends (FF), *i.e.*, overall rotation restrained, whereas three different end-conditions were considered for the *plates edges*: clamped (CC), simply-supported (SS) and simply in contact with end base plates (CB) at both ends. Throughout this work, the terms ‘CC columns’ and ‘SS columns’ refer to *plates* end-conditions. The former refers to columns with clamped edges, whereas the latter refers to stubs with simply-supported plates.

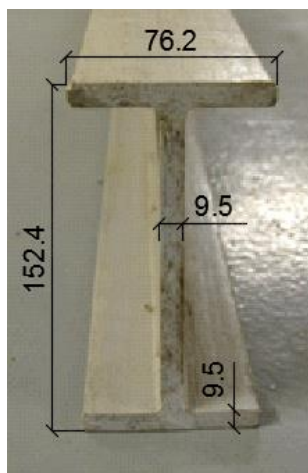
3.1. Studied I-sections

Pultruded GFRP members, made with E-glass fibers, having three different cross sections and two resin matrices were studied: an I-section 152.4 x 76.2 x 9.5-mm with polyester resin (I_1), another I-section 101.6 x 76.2 x 6.4-mm with vinyl ester matrix (I_2) and an H-section 101.6 x 101.6 x 6.4-mm with vinyl ester resin (I_3). In this work, specimens and profiles dimensions are in *mm* and the designation I_1 , I_2 and I_3 will be used to refer to each section. The nominal dimensions and material constituents of each section are specified in Table 3.1, as

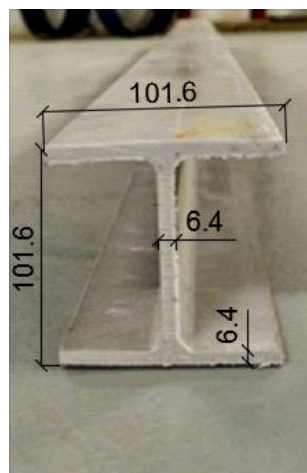
well as their flange-to-depth width ratio (b_f/d). Figure 3.1 presents the studied sections with their nominal dimensions.

Table 3.1 - Specifications of studied profiles

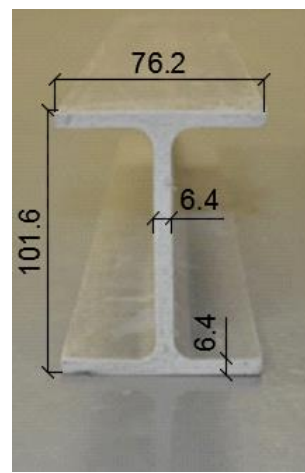
Section	Nominal Dimensions	Resin	Glass Fiber	b_f/d	
I_1	152.4 x 76.2 x 9.5	Polyester	E-glass	0.5	
I_2	101.6 x 76.2 x 6.4	Vinyl Ester	E-glass	0.75	
I_3	101.6 x 101.6 x 6.4	Vinyl Ester	E-glass	1.0	



(a)



(b)



(c)

Figure 3.1 – Studied I-Sections nominal dimensions: (a) I_1 ; (b) I_2 ; (c) I_3

It is important to highlight that I_2 sections were obtained by cutting 12.7 mm of each side of I_3 sections flanges, as shown in Figure 3.2. Therefore, the properties and typical layers of these sections are supposed to be the same.

The typical layers of I_1 and I_2 sections are shown in Figure 3.3 and 3.4, respectively. The pictures were obtained from a *Nikon SMZ 800* optical microscope, equipped with a digital camera. It is important to stand out that the fibers distribution varies widely, even with respect to the same section. As can be noticed, three roving layers were identified on the webs and flanges of I_1 sections, whereas only two were observed on I_2 sections.

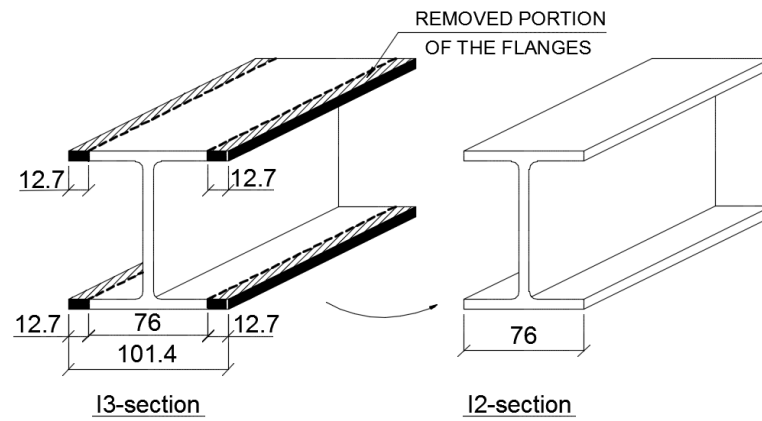
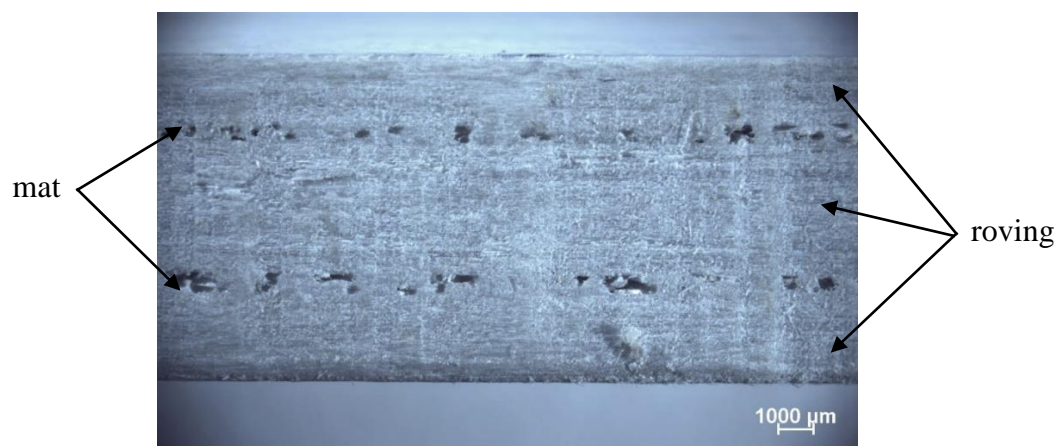


Figure 3.2 - I2-section profiles obtained by cutting parts of the flange of I3 profiles



(a) Web layers

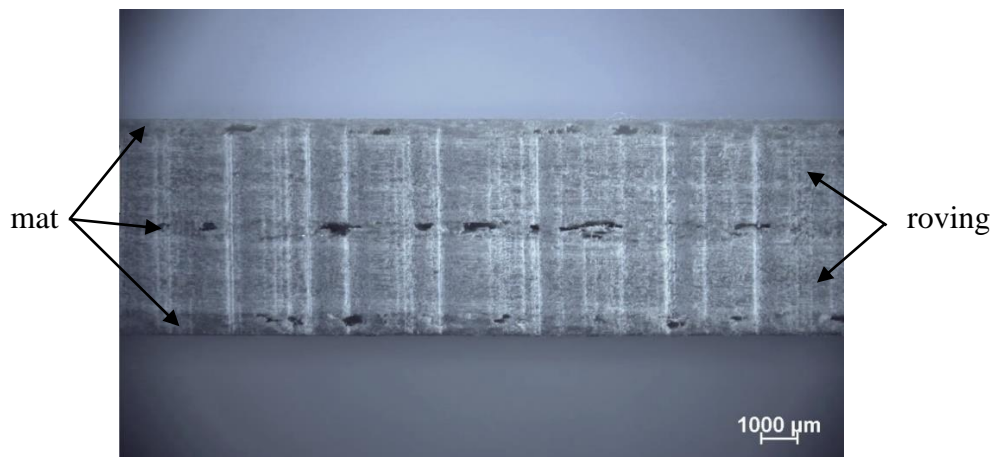


(b) Flange layers

Figure 3.3 - Layers of I1 profiles: (a) web layers; (b) flange layers



(a) Web layers



(b) Flange layers

Figure 3.4 - Layers of I2 profiles: (a) web layers; (b) flange layers

3.2. Material Characterization

The material properties were determined experimentally through five characterization tests, listed in Table 3.2.

Table 3.2 – Characterization tests and respective properties obtained

<i>Characterization Tests</i>	<i>Properties obtained</i>
<i>Burnout test</i>	Fiber volume ratio (V_f)
<i>Three-point bending test</i>	Longitudinal modulus and strength ($E_{L,f}$ and $F_{L,f}$)
<i>Transverse bending test</i>	Transverse modulus ($E_{L,t}$)
<i>Iosipescu / Torsion tests</i>	Shear modulus (G_{LT})
<i>Combined loading compression test</i>	Longitudinal modulus and strength ($E_{L,c}$ and $F_{L,c}$)

In order to identify the specimens for the characterization tests, sets of letters and numbers were used, as shown in Figure 3.5. The first set refers to the profile from which the coupon was extracted (I_1 , I_2 or I_3). The second is related to the specimen's number, whereas the third refers to the respective characterization test. Finally, the last set identifies the region from where the specimen was cut (acronyms in Portuguese). The specimens of the transverse bending test were identified without the fourth set.

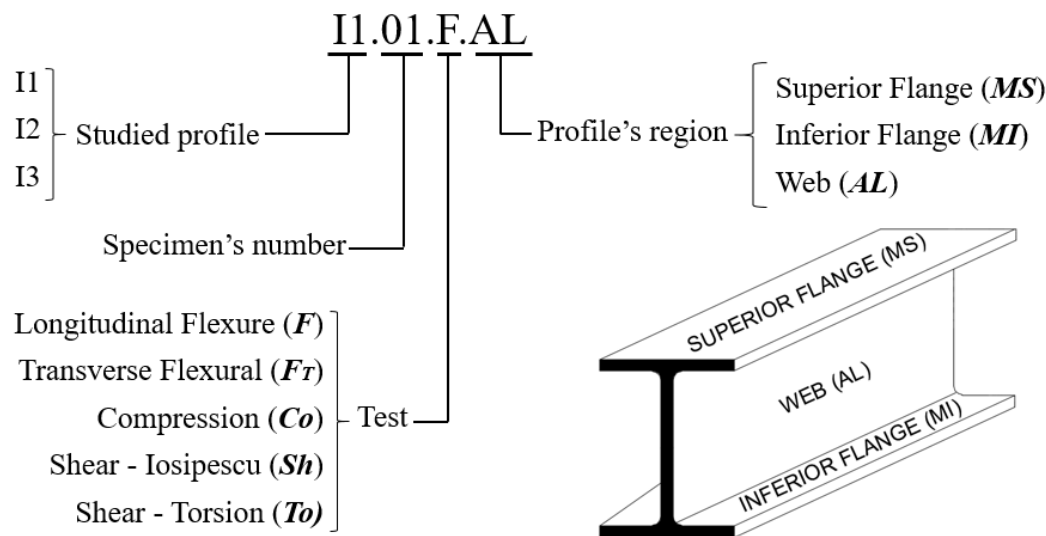


Figure 3.5 - Alphanumeric code for specimens' identification

3.2.1. Fiber Volume Fraction

In order to determine the fiber volume ratio, a Burnout Tests following recommendations of ISO 1172:1996 were conducted at the Fernando Lobo Carneiro Material Structure Laboratory (LABEST) of Federal University of Rio de Janeiro (UFRJ). In all, twelve squares 20x20-mm samples were tested, among which half were extracted from I_1 profiles and the other half from I_2 -section profiles. For the test, twelve porcelain crucibles with variable sizes, a balance graduated to 0,1 mg, a muffle furnace and a desiccator were used. The specimens and a representative crucible are shown in Figure 3.6 a and b, respectively.



Figure 3.6 - Burnout test: (a) samples; (b) crucible with samples extracted from I_1 and I_2

The test consisted in placing the samples in porcelain crucibles and into a muffle furnace where an elevated temperature was applied to carbonize the resin. The specimens and crucibles were cleaned and weighed individually, as shown in Figure 3.7. After, the crucibles containing the specimens were placed in the desiccator while transported to the INTI[®] muffle furnace, as shown in Figure 3.8.

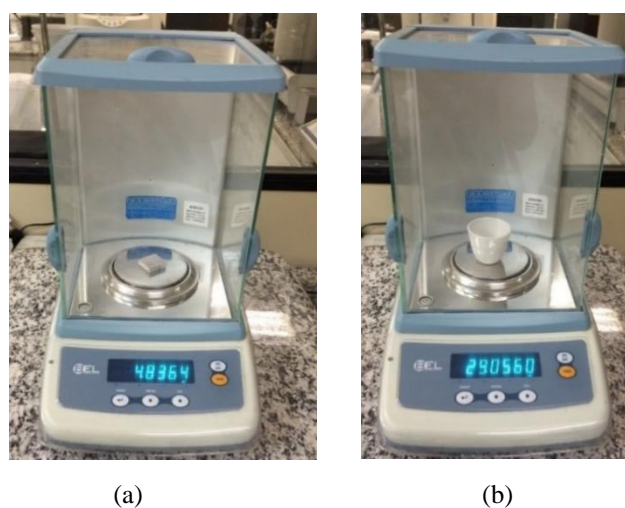


Figure 3.7 - Weighing: (a) Samples, (b) Crucibles

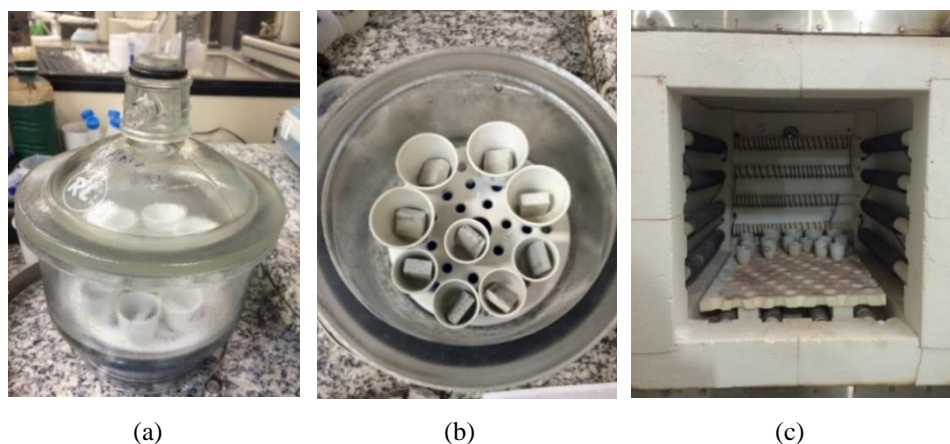


Figure 3.8 – (a) and (b): Desiccator with 9 of 12 crucibles containing the samples before being placed into the furnace; (c) muffle furnace

In order to burn out the samples, but avoiding fibers degradation, the specimens were subject to a temperature of 600° C for three hours. After the test, the crucibles containing the post-burned samples were placed into the desiccator and were reweighed, as shown in Figure 3.9. The roving was separated from the mat (Figure 3.10) and in order to determine the percentage of each type of fiber in the composite, the porcelain crucible containing the roving was also weighed.

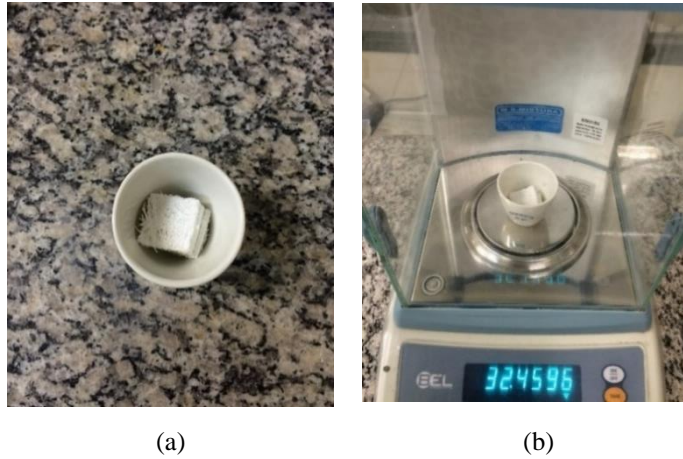


Figure 3.9 – Post-burn: (a) Crucible containing the post-burned samples; (b): Reweighing

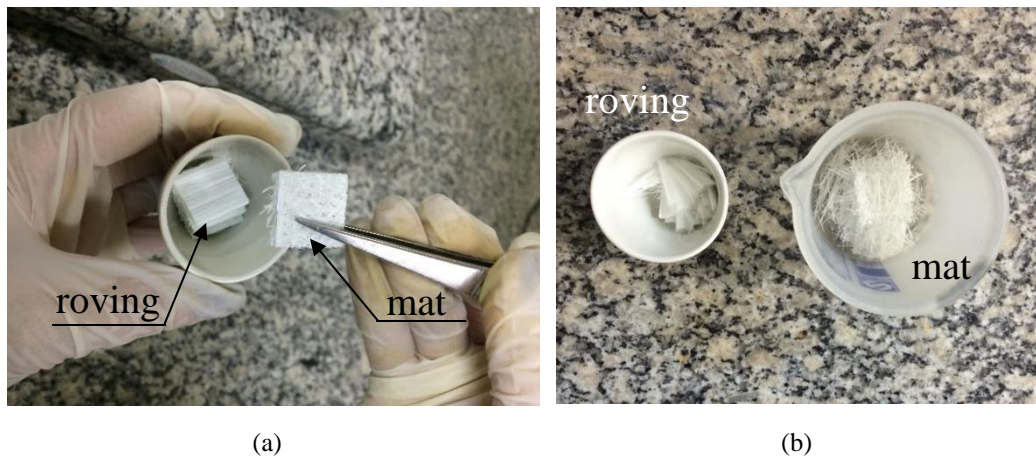


Figure 3.10 (a) and (b) - Separation of roving from mat

The fiber content by weight W_f was obtained by Eq. 3.1. Table 3.3 presents the values w_1 , w_2 and w_3 obtained for each studied profile.

$$W_f (\%) = \frac{w_3 - w_1}{w_2 - w_1} \times 100 \quad (3.1)$$

where:

w_1 is the initial weight of the porcelain crucible;

w_2 is the initial weight of the porcelain crucible containing the sample;

w_3 is the weight of the porcelain crucible containing the post-burned sample.

Table 3.3 - Weight w_1 , w_2 and w_3

<i>Specimens</i>		<i>w₁ (g)</i>	<i>w₂ (g)</i>	<i>w₃ (g)</i>
<i>Section I₁</i>	<i>I1.01.AL</i>	28.167	34.062	31.422
	<i>I1.02.AL</i>	29.056	34.532	32.124
	<i>I1.03.AL</i>	29.520	34.742	32.359
	<i>I1.04.MS</i>	28.550	34.825	32.460
	<i>I1.05.MS</i>	12.829	18.904	16.292
	<i>I1.06.MI</i>	75.584	81.983	79.541
<i>Section I₂</i>	<i>I2.01.AL</i>	11.479	16.028	14.433
	<i>I2.02.AL</i>	12.037	16.874	15.151
	<i>I2.03.MS</i>	57.127	62.362	60.623
	<i>I2.04.MS</i>	11.903	16.739	25.043
	<i>I2.05.MI</i>	11.627	16.260	14.864
	<i>I2.06.MI</i>	60.089	64.463	62.898

In order to determine the fiber volume ratio, the specific mass of the composite ρ_c were determined with the aid of a helium gas picnometer, model *Accupyc 1340 Micromeritics*. This equipment prescribes the volume of a known sample mass through the gas pressure variation in a calibrated volume. Table 3.4 shows the composites and glass fiber specific masses (ρ_c and ρ_f).

Table 3.4 - Specific masses

<i>Specific Mass</i>	<i>I₁</i>	<i>I₂</i>
<i>Composite $\rho_c^{(1)}$</i>	1.862	1.839
<i>Glass Fiber $\rho_f^{(2)}$</i>	2.54	

(1) Obtained through the picnometer

(2) MALLICK (1997)

The fiber volume ratios were obtained through Eq. 3.2:

$$V(\%) = \frac{\rho_c}{\rho_f} \times W(\%) \quad (3.2)$$

The fibers contents by weight and volume for I₁ and I₂-section profiles are indicated in Table 3.5 and 3.6, respectively.

Table 3.5 - Fibers contents by weight and volume for I1 sections

<i>Specimens</i>		<i>Fiber Content by Weight</i>			<i>Fiber Volume Ratio</i>		
		W_{glass} (%)	W_{roving} (%)	W_{mat} (%)	V_{glass} (%)	V_{roving} (%)	V_{mat} (%)
<i>II.01.AL</i>		55.21	39.17	16.03	40.47	28.71	11.75
<i>II.02.AL</i>		56.02	40.07	15.96	41.07	29.37	11.70
<i>II.03.AL</i>		54.37	38.29	16.08	39.85	28.06	11.79
<i>II.04.MS</i>		62.31	48.61	13.70	45.67	35.63	10.04
<i>II.05.MS</i>		57.00	49.94	7.07	41.78	36.60	5.18
<i>II.06.MI</i>		61.84	52.46	9.38	45.33	38.45	6.87
<i>Flange</i>	Av⁽¹⁾ (%)	60.38	50.34	10.05	44.26	36.90	7.37
	sd⁽²⁾ (%)	2.40	1.59	2.75	1.76	1.17	2.02
	cov⁽³⁾	0.0397	0.0317	0.2738	0.0397	0.0317	0.2737
<i>Web</i>	Av⁽¹⁾ (%)	55.20	39.18	16.02	40.46	28.72	11.75
	sd⁽²⁾ (%)	0.675	0.72	0.05	0.49	0.53	0.04
	cov⁽³⁾	0.0122	0.0186	0.0032	0.0122	0.0185	0.0032
<i>Profile</i>	Av⁽¹⁾ (%)	57.79	44.76	13.04	42.36	32.81	9.56
	sd⁽²⁾ (%)	3.13	5.71	3.56	2.30	4.19	2.61
	cov⁽³⁾	0.0542	0.1277	0.2735	0.0542	0.1277	0.2735

(1) Average

(2) Standard Deviation

(3) Coefficient of Variation

Table 3.6 - Fibers contents by weight and volume for I2 section

<i>Specimens</i>		<i>Fiber Content by Weight</i>			<i>Fiber Volume Ratio</i>		
		W_{glass} (%)	W_{roving} (%)	W_{mat} (%)	V_{glass} (%)	V_{roving} (%)	V_{mat} (%)
<i>I2.01.AL</i>		64.94	53.44	11.50	47.02	38.70	8.33
<i>I2.02.AL</i>		64.37	47.73	16.64	46.61	34.56	12.05
<i>I2.03.MS</i>		66.78	59.04	7.74	48.36	42.76	5.60
<i>I2.04.MS</i>		64.94	55.48	9.47	47.03	40.17	6.85
<i>I2.05.MI</i>		69.87	62.02	7.84	50.59	44.91	5.68
<i>I2.06.MI</i>		64.22	53.22	11.00	46.50	38.54	7.96
<i>Flange</i>	Av⁽¹⁾ (%)	64.65	57.44	9.01	48.12	41.59	6.52
	sd⁽²⁾ (%)	0.28	3.36	1.33	1.13	2.44	0.96
	cov⁽³⁾	0.0044	0.0585	0.1482	0.0235	0.0585	0.1482
<i>Web</i>	Av⁽¹⁾ (%)	66.45	50.59	14.07	46.82	36.63	10.19
	sd⁽²⁾ (%)	2.18	2.85	2.57	0.21	2.07	1.86
	cov⁽³⁾	0.0328	0.0564	0.1827	0.0044	0.0564	0.1827
<i>Profile</i>	Av⁽¹⁾ (%)	65.85	55.16	10.70	47.69	39.94	7.75
	sd⁽²⁾ (%)	1.98	4.55	3.01	1.43	3.29	2.18
	cov⁽³⁾	0.0300	0.0825	0.2817	0.0300	0.0825	0.2816

(1) Average

(2) Standard Deviation

(3) Coefficient of Variation

When comparing the fiber volume ratio (V_f) of both studied sections, it can be noticed that I₂ profiles present higher average of roving, whereas I₁ sections have greater mat fractions. Further, I₂ sections present more total fiber contents (roving + mat) than I₁ profiles.

With respect to the different V_f on webs and flanges, both profiles present greater average roving on the flanges and higher mat fractions on the webs. However, for I₂ sections the difference between the fiber volume ratio on flanges and webs is very small.

3.2.2. Longitudinal Bending Modulus and Strength ($E_{L,f}$ and $F_{L,f}$)

In order to determine the longitudinal bending modulus $E_{L,f}$ and strength $F_{L,f}$, two different procedures may be adopted for flexural tests: the three and four-point bending tests, described in ASTM D790 (2015) and ASTM D6272 (2010), respectively. Equivalent ISO standards are also available, *e.g.* ISO 14125 (1998) for three-point bending.

In this work, three-point bending tests were carried out to obtain the longitudinal bending modulus ($E_{L,f}$) and strength ($F_{L,f}$), following recommendations of ISO 14125 and ASTM D790. The specimens' dimensions were defined according to Table A.1 of ISO 14125. The ratios $L/t = 20$ and $l/t = 30$ were adopted as suggested by ISO to reduce influence shear deformation, where L is the test span, l is the specimen length and t is the thickness, as shown in Figure 3.11. The average dimensions measured with a digital caliper are presented in Table 3.7.

Table 3.7 – Specimens dimensions

<i>Specimen's Dimensions</i>	I_1	I_2
t (mm)	9.60 ± 0.12	6.30 ± 0.11
b (mm)	15.63 ± 0.50	15.80 ± 0.21
l (mm)	285	195
L (mm)	200	130

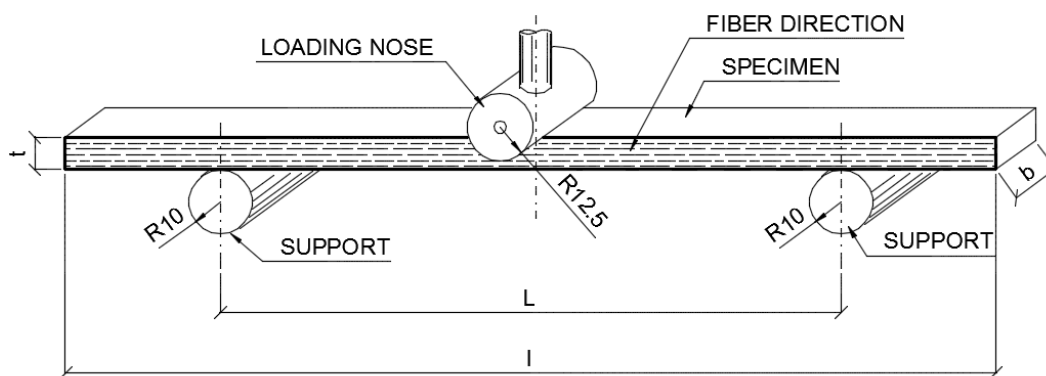


Figure 3.11 - Three-point bending test scheme

In all, ten longitudinally-oriented coupons 15-mm wide x 285-mm long were extracted from I_1 profiles and six longitudinally-oriented coupons of 15-mm

wide x 195-mm long were extracted from flanges and webs of I_2 profiles. The sets of the specimens are shown in Figure 3.12.

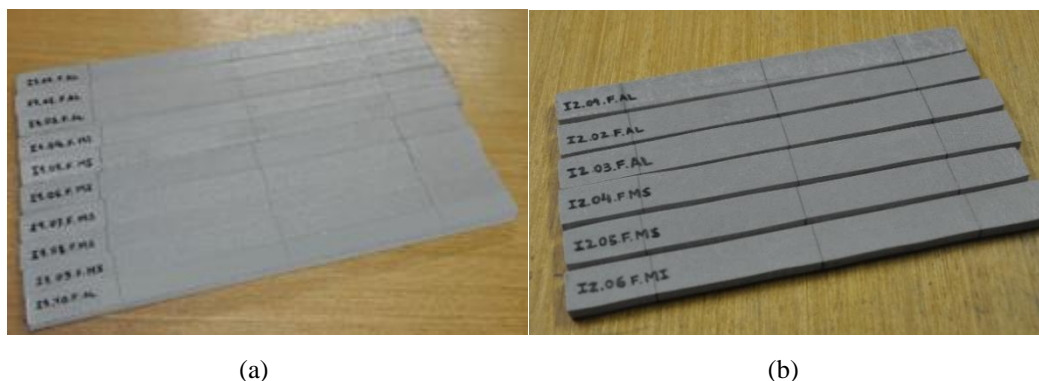


Figure 3.12 - Coupons for bending test: (a) from I_1 ; (b) from I_2

The tests were conducted up to failure under a displacement controlled rate of 2 mm/min on a servo-hydraulic universal testing machine *MTS model 204.63* machine with load capacity of 100 kN. Mid-span deflections were measured using internal transducers, which were compared and validated by an external transducer used in preliminary tests. Figure 3.13 presents the bending test fixture.

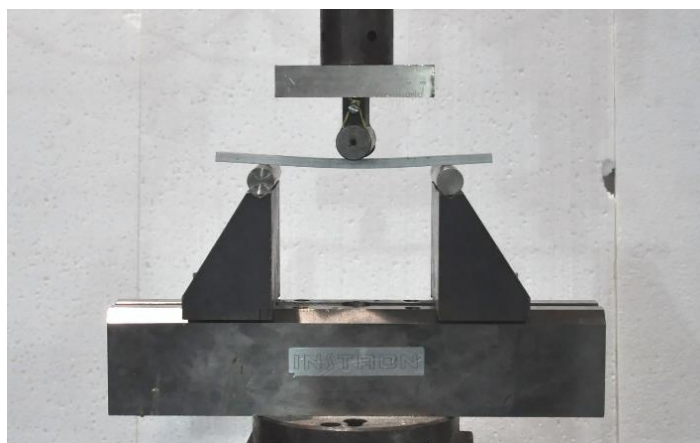


Figure 3.13 - Bending test fixture

Two failures modes were observed along the tests: one initiated by interlaminar shear and other by tensile fracture of the fiber, as shown in Figure 3.14 (a) and (b), respectively. According to ISO 14125, the former is not acceptable for obtaining flexure strength and the coupons that presented this kind of fracture ($I_1.01$

to I₁.03, I₂.02 and I₂.03) were not considered to obtain the flexural strength $F_{L,f}$, as shown in Tables 3.10 and 3.11.

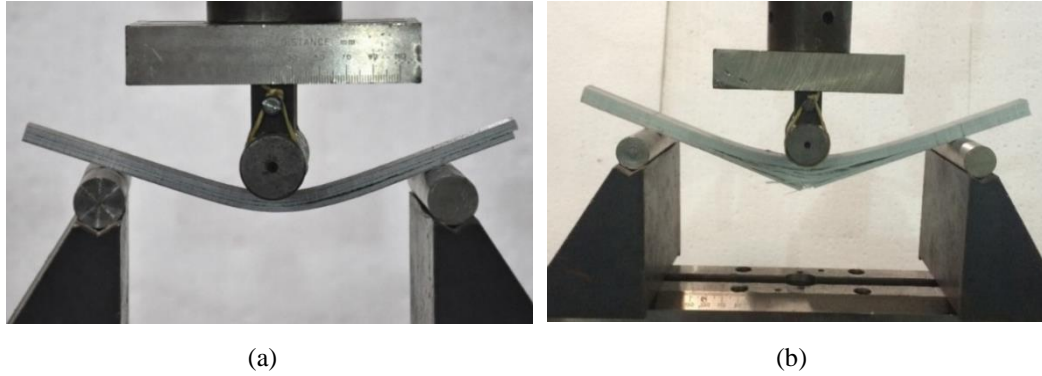


Figure 3.14 – Failure modes obtained: (a) interlaminar shear fracture (b) tensile fracture of fiber

In order to obtain the flexural modulus and strength, the stress-strain curves were plotted for each specimen tested, using well-known Strength of Materials Equations 3.3 and 3.4 to determine strain $\varepsilon_{L,f}$, and stress $\sigma_{L,f}$.

$$\varepsilon_{L,f} = \frac{6 t s}{L^2} \quad (3.3)$$

$$\sigma_{L,f} = \frac{3 P L}{2 b t^2} \quad (3.4)$$

where s is the deflection measured by the displacement transducer and P is the applied load.

Stress-strain curves for specimens extracted from I₁ and I₂ are presented in Figure 3.15. The flexural modulus $E_{L,f}$ were obtained as the slope of the linear portion between strains 0.0005 and 0.01 of the stress-strain curve. Tables 3.8 and 3.9 present a summary, including the averages and the standard deviations for the flexural moduli of I₁ and I₂ profiles. Whereas Tables 3.10 and 3.11 present the average flexural strength for both I-section columns.

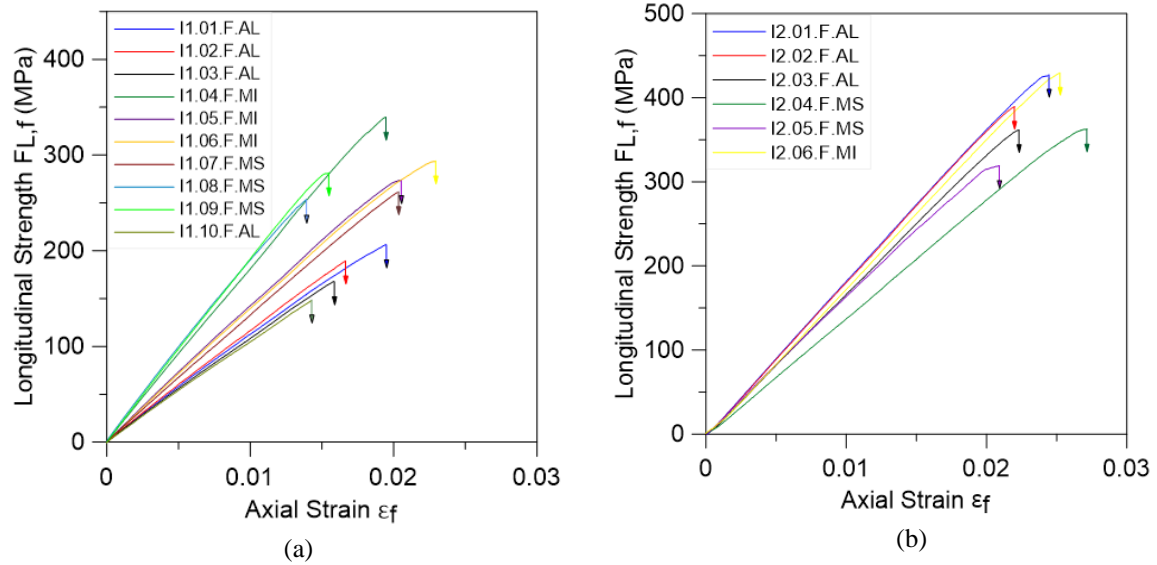


Figure 3.15 - Stress-Strain Curve: (a) specimens from I_1 profiles; (b) specimens from I_2 profiles

Table 3.8 - Flexural Modulus of I_1

<i>Specimen</i>	<i>$E_{L,f}$ (GPa)</i>
<i>$I_{1.01.F.AL}$</i>	11.72
<i>$I_{1.02.F.AL}$</i>	12.19
<i>$I_{1.03.F.AL}$</i>	11.25
<i>$I_{1.04.F.MI}$</i>	18.62
<i>$I_{1.05.F.MI}$</i>	14.75
<i>$I_{1.06.F.MI}$</i>	14.55
<i>$I_{1.07.F.MS}$</i>	13.49
<i>$I_{1.08.F.MS}$</i>	20.04
<i>$I_{1.09.F.MS}$</i>	19.71
<i>$I_{1.10.F.AL}$</i>	10.96
Average:	14.73 ± 3.33
<i>cov</i>⁽¹⁾	0.227

⁽¹⁾ Coefficient of variation

Table 3.9 - Flexural Modulus of I_2

<i>Specimen</i>	<i>$E_{L,f}$ (GPa)</i>
<i>$I_{2.01.F.AL}$</i>	18.20
<i>$I_{2.02.F.AL}$</i>	17.06
<i>$I_{2.03.F.AL}$</i>	15.75
<i>$I_{2.04.F.MS}$</i>	12.96
<i>$I_{2.05.F.MS}$</i>	16.93
<i>$I_{2.06.F.MI}$</i>	14.42
Average:	15.89 ± 1.76
<i>cov</i>⁽¹⁾	0.111

⁽¹⁾ Coefficient of variation

Table 3.10 - Flexural Strength of I₁

<i>Specimen</i>	<i>F_{L,f} (MPa)</i>
<i>I_{1.04.F.MI}</i>	348.97
<i>I_{1.05.F.MI}</i>	273.38
<i>I_{1.06.F.MI}</i>	293.87
<i>I_{1.07.F.MS}</i>	260.82
<i>I_{1.08.F.MS}</i>	252.96
<i>I_{1.09.F.MS}</i>	281.26
<i>I_{1.10.F.AL}</i>	148.31
<i>Average:</i>	265.65 ± 56.05
<i>cov⁽¹⁾</i>	0.211

⁽¹⁾ Coefficient of variationTable 3.11 - Flexural Strength of I₂

<i>Specimen</i>	<i>F_{L,f} (MPa)</i>
<i>I_{2.01.F.AL}</i>	426.98
<i>I_{2.04.F.MS}</i>	362.36
<i>I_{2.05.F.MS}</i>	319.08
<i>I_{2.06.F.MI}</i>	428.53
<i>Average:</i>	384.24 ± 46.13
<i>cov⁽¹⁾</i>	0.120

⁽¹⁾ Coefficient of variation

As can be noticed in Table 3.8, the moduli of elasticity for specimens extracted from I₁ webs were lower than the ones cut from the flanges. On the other hand, flanges and webs of I₂ profiles presented closer results.

Through Tables 3.10 and 3.11, it can be observed that I₂ specimens exhibited higher strengths than I₁. Further, almost all specimens extracted from webs presented an interlaminar shear fracture. Therefore, it was not possible to achieve a good comparison between the flexural strength of webs and flanges for the studied sections.

The results are apparently consistent with the fiber volume ratios presented in section 3.2.1 and layers distribution shown in section 3.1.

3.2.3. Transverse bending (E_{T,f})

In pultruded GFRP, the narrow sections may be an obstacle to determine the transverse bending modulus (E_{T,f}), once the coupons cannot be extracted with the dimensions required in standards. In these cases, non-standard tests have been successfully adopted by many authors (*e.g.* CARDOSO *et al.*, 2014, TOGASHI, 2017).

In this work, for the same mentioned reason, the transverse bending moduli were obtained using a non-standard test. Four specimens with a ‘T’ shape and 20-

mm wide (b) and half of the section depth ($d/2$) were extracted from the profiles and tested (two for each). Figure 3.16 illustrates how the specimens were extracted and Figure 3.17 shows the specimens for I₁ (on the left) and I₂ profiles (on the right).

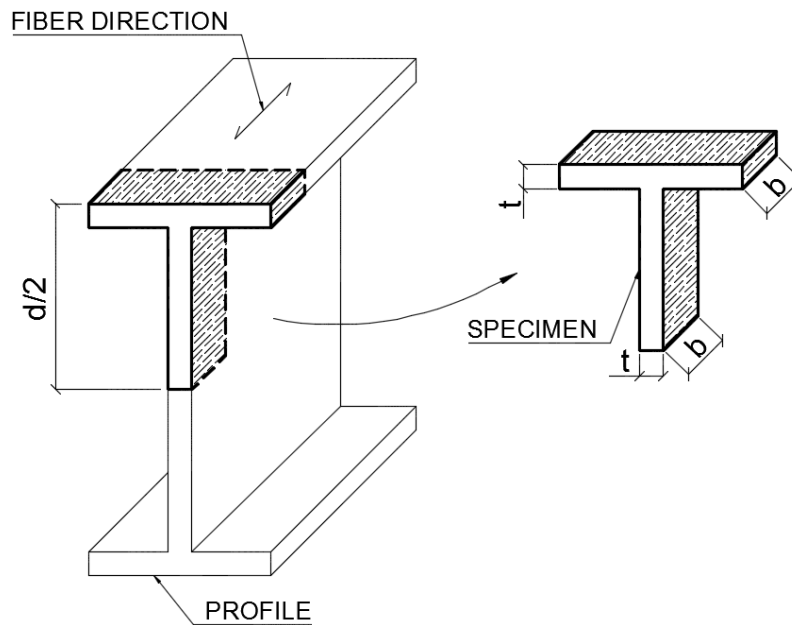


Figure 3.16 – Extraction of T-shaped coupons from profile

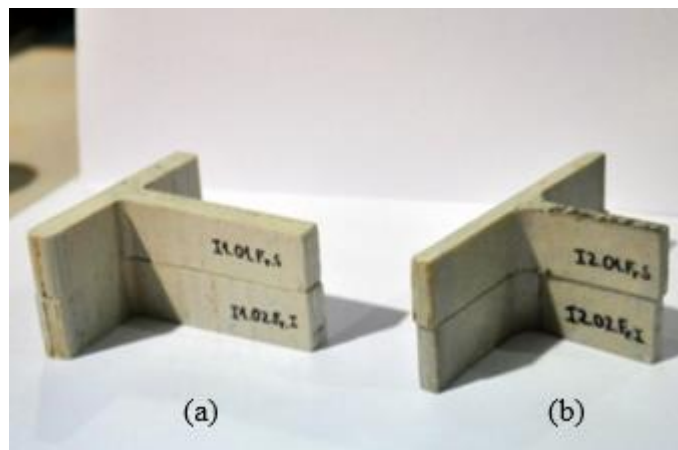


Figure 3.17 - Specimens for the transverse bending test: (a) I1; (b) I2

In this non-standard test, a load P perpendicular to the flange and eccentric with respect to the web neutral axis was applied to the specimen using a pulley system, while the strains were measured by back-to-back strain-gages positioned on the web portion of the specimens. During the test, grips were used to keep the T web clamped. A load cell was used to confirm the applied loads and all data were gathered automatically using the software *catmanEasy v4.1.2* (HBM Manual,

2005). Figure 3.18 illustrates the test setup whereas the specimen's dimensions measured with a digital caliper for each profile and the respective values for the lever arm e are indicated in Table 3.12.

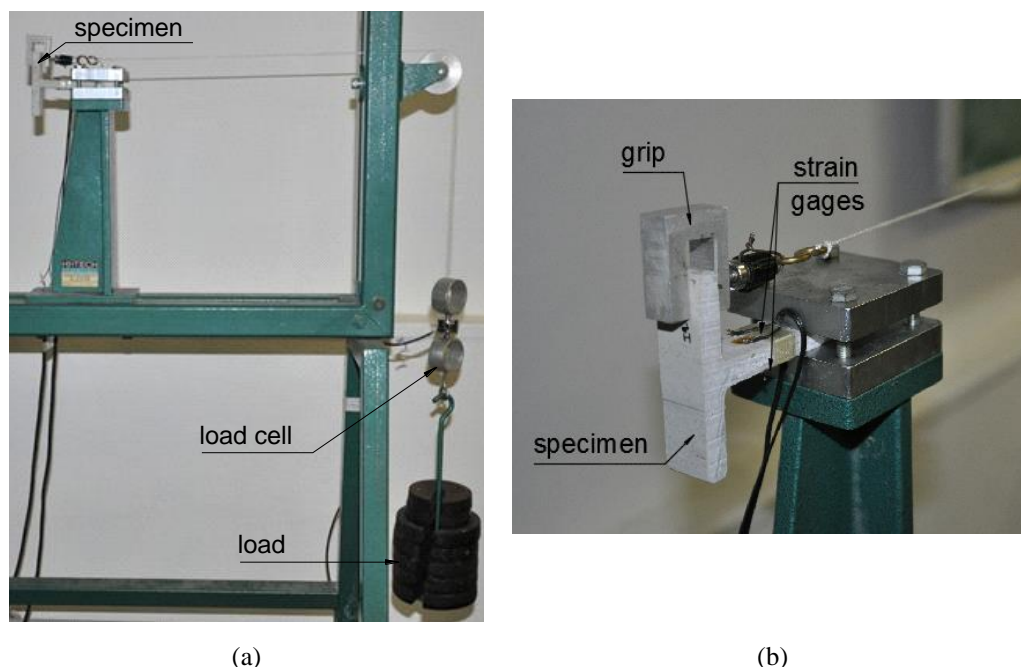


Figure 3.18 - Transversal bending test: (a) test set-up; (b) strain gages position

Table 3.12 – Adopted dimensions

<i>Specimen</i>	<i>t (mm)</i>	<i>b (mm)</i>	<i>e (mm)</i>
<i>I1.01.Ft</i>	9.9	20.6	30
<i>I1.02.Ft</i>	9.6	20.4	30
<i>I2.01.Ft</i>	6.6	20.7	45
<i>I2.02.Ft</i>	6.6	20.6	45

The load P , applied on a distance e from the centroid of the sample, produced a moment about the z axis, as presented in Figure 3.19. Thus, a moment *versus* curvature $1/r$ curve can be plotted, from which the slope of the straight line corresponds to the transverse bending modulus multiplied by the specimen's second moment of area (EI). The curvatures are obtained through Eq. 3.5, where ε_{sup} and ε_{inf} are the superior and inferior measured strains.

$$\frac{1}{r} = \frac{\varepsilon_{sup} - \varepsilon_{inf}}{t} \quad (3.5)$$

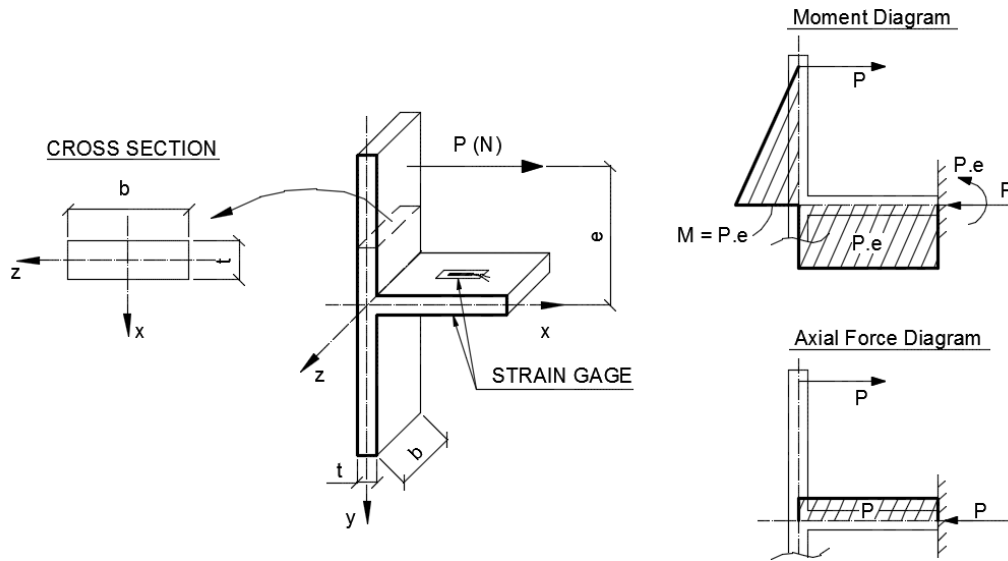


Figure 3.19 - Bending Test Scheme and corresponding moment and axial force diagrams

As shown in Figure 3.19, axial forces are also produced in the instrumented region. However, the strains produced by these ones are small when compared to those produced by bending, therefore not affecting the experimental results. It is also important to stand out that this test is not perfect, once the stiffness of the web-flange interface may affect the results.

Figure 3.20 a and b present the plots $M \times 1/r$ of the coupons extracted from I_1 and I_2 profiles, respectively. Tables 3.13 and 3.14 present the average transverse bending modulus for each studied profile.

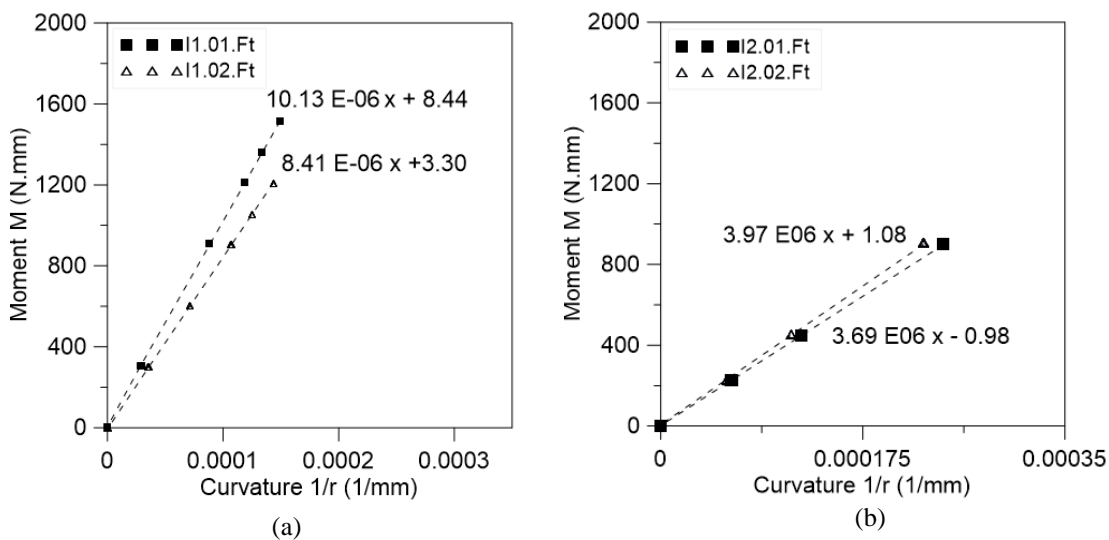


Figure 3.20 - Curve $M \times 1/r$: (a) Coupons from I_1 ; (b) Coupons from I_2

Table 3.13 - Transverse Bending Modulus of I₁

<i>Sample</i>	<i>EI (N.mm²)</i>	<i>I (mm⁴)</i>	<i>E (GPa)</i>
<i>I1.01.Ft</i>	10.13 x 10 ⁶	1.66 x 10 ³	6.08
<i>I1.02.Ft</i>	8.41 x 10 ⁶	1.50 x 10 ³	5.59
<i>Average</i>			5.84

Table 3.14 - Transverse Bending Modulus of I₂

<i>Sample</i>	<i>EI (N.mm²)</i>	<i>I (mm⁴)</i>	<i>E (GPa)</i>
<i>I2.01.Ft</i>	3.69 x 10 ⁶	495.9	7.44
<i>I2.02.Ft</i>	3.97 x 10 ⁶	493.5	8.05
<i>Average</i>			7.75

As can be observed in Tables 3.13 and 3.14, I₁ and I₂ sections present near transverse bending moduli. These results are apparently consistent, once I₁ and I₂ profiles have similar mat fractions and matrix properties.

3.2.4. Shear Modulus (G_{LT})

A non-linear shear response has been observed for pGFRP composites (*e.g.* ZUREICK and SCOTT, 1997). Further, many shear tests do not provide a full shear stress-strain relationship due to difficulty in reaching a pure and uniform state of shear stress in the test coupons (ADAMS *et al.*, 2003). According to PINDER (1989), the values reported in literature for the in-plane shear modulus (G_{LT}) of FRP present many discrepancies, due to incorrect interpretations of tests data caused by shear non-uniformities. Thereby, although many shear tests are available in literature, only a few are commonly used.

One of the most used shear tests is the *Iosipescu test* (ASTM D5379-12), also called asymmetric bending test. It is preferred by many researchers (*e.g.* BANK, 1990, SONTI and BARBERO, 1996, ZUREICK AND SCOTT, 1997, ZUREICK AND STEFFEN, 2000 and KANG, 2002) because the specimen preparation is simple and the results are accurate and relatively easy to interpret. However, a specific test fixture is required, which may not be always available. Because of this lack of special apparatus, other non-standard tests are reported in

literature, such as the *torsion test*, which was adopted by SONTI and BARBERO (1996), TURVEY (1998) and TOGASHI (2017).

In this work, non-standard torsion tests were conducted in order to experimentally determine the shear moduli and the results obtained were validated by the Iosipescu test for material extracted from I₂. This was particularly important because local buckling in sections having $b_f/d = 0.75$ and 1.0 is dominated by flange properties, in which the in-plane shear modulus G_{LT} plays an important role. Therefore, in this case, a good estimate of G_{LT} was necessary. For I₁ profiles, only torsion tests were conducted for coupons extracted from web. Both are presented in the following sections.

3.2.4.1. Torsion Tests

Two longitudinally-oriented specimens were extracted from each I-section profile, having the same dimensions adopted on the bending test, *i.e.* – 15-mm wide x 285-mm long for I₁ profiles and 15-mm wide x 195-mm for I₂ ones. In flange-dominated buckling problems (case of I₂ sections), the behavior is mainly governed by the flange properties. Even though, for these sections profiles, the coupons were extracted from both flange and web. Whereas for I₁ sections, the specimens were cut only from webs. The strains were captured by a 45° strain gage positioned on the center of specimen's face. Figure 3.21 and Table 3.15 present the specimens dimension, as well as the torsion span L_1 .

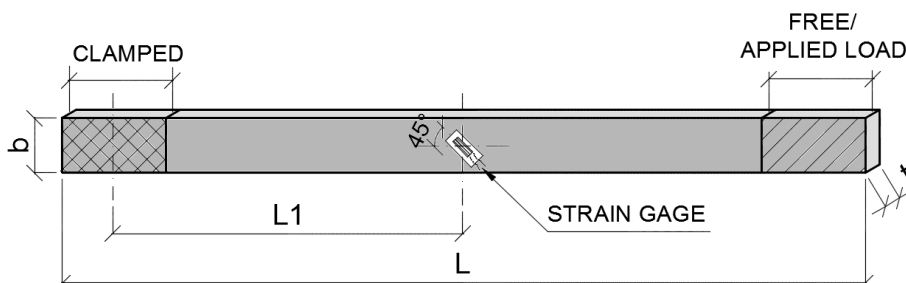


Figure 3.21 – Specimen geometry adopted for torsion tests

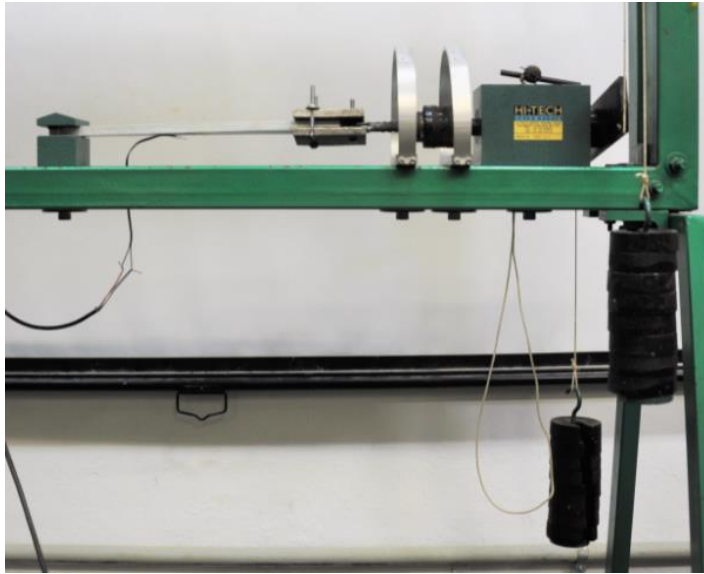
Table 3.15 - Specimens dimensions

<i>Specimen</i>	<i>t (mm)</i>	<i>b (mm)</i>	<i>L (mm)</i>	<i>L₁ (mm)</i>
<i>I1.01.To.AL</i>	9.5	16.1	285	130
<i>I1.02.To.AL</i>	9.4	14.4	285	126.5
<i>I2.01.To.MI</i>	6.2	15.1	195	83.5
<i>I2.02.To.AL</i>	6.5	15.6	195	83.5

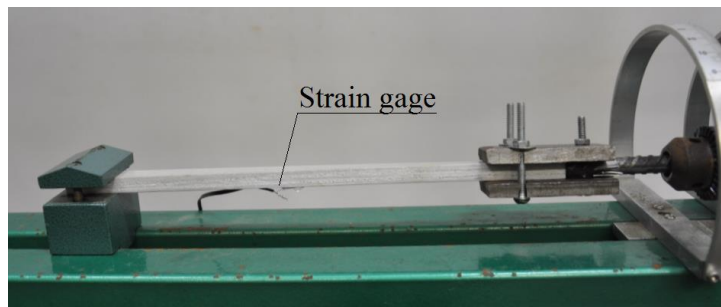
In this non-standard test, torsion about the longitudinal axis was applied at one end of the specimen, whereas the other end was clamped on a fixed support. The torsion is provided via load hangers on nylon cords, one of which passes up over an offset pulley, as shown in Figure 3.22. An adapter was necessary to couple the specimen with the mandrel (torsion head). Figure 3.23 presents pictures taken during the test.



Figure 3.22 - Non-standard torsion test fixture (Adapted from TOGASHI, 2017)



(a)



(b)

Figure 3.23 - Torsion test: (a) overview; (b) specimen twisted

The strains were measured after each increment of weight (2N) with the aid of a Vishay portable strain indicator, *Model P-350A*, shown in Figure 3.24.



Figure 3.24 – Portable Strain Indicator

The in-plane shear moduli G_{LT} of an orthotropic rectangular cross section subjected to pure torsion can be obtained by Eq. 3.6 (TURVEY, 1998).

$$G_{LT} = \frac{T L_1}{\theta J} \quad (3.6)$$

in which T is the torque, θ is the angle of twist, J is the torsion constant equal to $\beta c b t^3$ and L_1 is the torsion span.

The parameters β and c and the angle of twist θ are expressed in Eq. 3.7, 3.8 and 3.9, respectively, and were calculated by assuming transverse isotropy.

$$\beta(c) = 32 \frac{c^2}{\pi^4} \sum_{k=1,3,5}^{\infty} \frac{1}{k^4} \left(1 - \frac{2c}{k\pi} \tanh \left\{ \frac{k\pi}{2c} \right\} \right) \quad (3.7)$$

$$c = \frac{b}{t} \sqrt{\frac{G_{TT}}{G_{LT}}} \quad (3.8)$$

$$\theta = \frac{2L}{t} \varepsilon_{45} \quad (3.9)$$

where G_{TT} is the through-thickness shear modulus and ε_{45} are the strains recorded after each increment of weight.

By substituting Eq. 4.7 on 4.4, the in-plane shear modulus can be expressed by Eq. 3.10.

$$G_{LT} = \frac{T t}{2 J \varepsilon_{45}} \quad (3.10)$$

Therefore, the shear modulus was obtained as the slope of the curve T versus $2J\varepsilon_{45}/t$, which are plotted for each studied I-section in Figure 3.25 a and b.

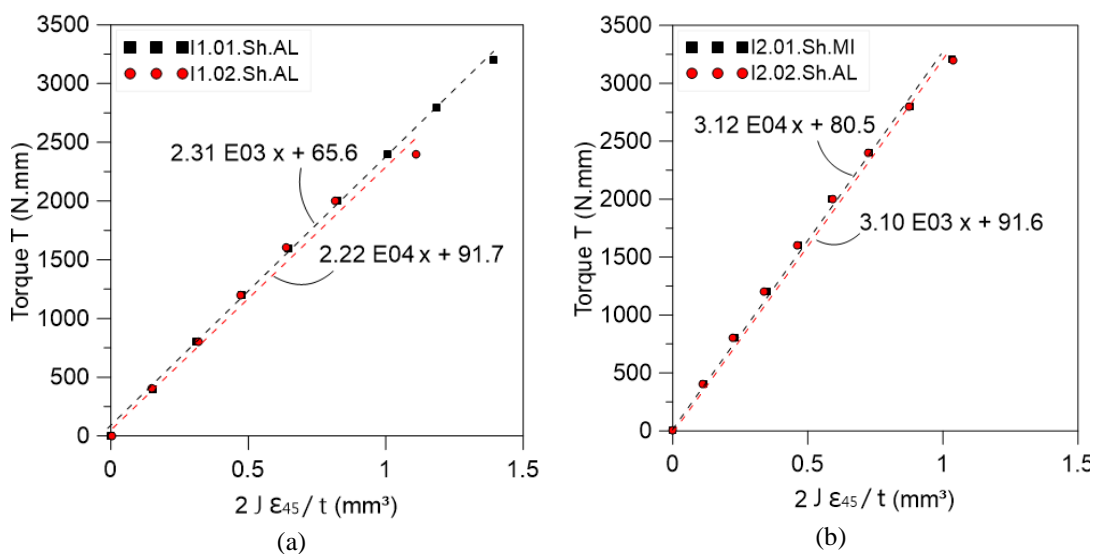


Figure 3.25 - T versus $2J\epsilon_{45}/t$: (a) Specimens extracted from I_1 ; (b) Specimens extracted from I_2

The shear moduli for each I-section are presented in Tables 3.16 and 3.17.

Table 3.16 Shear moduli of I_1 sections

<i>Specimen</i>	G_{LT} (GPa)
<i>I₁.01.Sh.AL</i>	2.31
<i>I₁.02.Sh.AL</i>	2.22
Average:	2.26

Table 3.17 - Shear moduli of I_2 sections

<i>Specimen</i>	G_{LT} (GPa)
<i>I₂.01.Sh.MI</i>	3.12
<i>I₂.02.Sh.AL</i>	3.10
Average:	3.11

Although I_1 profiles have higher mat volume fractions than I_2 sections, the shear moduli of I_1 profiles were lower than those ones obtained for I_2 , as can be observed in Tables 3.16 and 3.17.

3.2.4.1. Iosipescu Test

In order to validate the shear moduli obtained from torsion tests, Iosipescu tests were carried out for profile I_2 , following recommendations of the ASTM 5379. In this method, the specimens have V-notched details introduced in an apparently shear constant and ‘null’ moment region, which results in a nearly pure shear state

of stress, but not uniform (PINDERA, 1989). For this work, an adaptation of Iosipescu test fixture was fabricated, as illustrated in Figure 3.26.

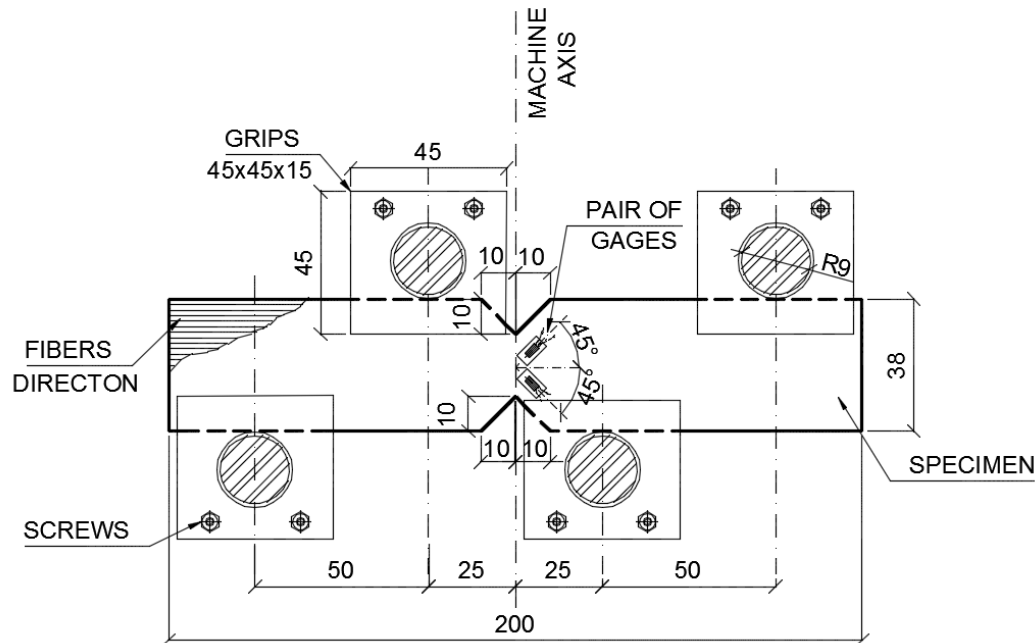


Figure 3.26 - Adapted Iosipescu test fixture

Three longitudinally-oriented specimens 38-mm wide x 200-mm long x 6.4-mm with V-notches details were extracted from the profiles flanges and tested. Aluminum tabs were locally bonded to both faces of the specimen away from the test region. According to the followed standard, this procedure strengthens and stabilizes the specimen, avoiding localized crushing failure in loading points, also reducing the possibility of twisting.

The tests were conducted until failure – defined by a sudden drop in the load/displacement plot – under a displacement controlled rate of 0.5 mm/min using a servo-hydraulic *MTS model 204.63* machine with load capacity of 100 kN. The strains were captured by a $\pm 45^\circ$ pair of strain gages positioned between the notches. However, once the pair of gages were not positioned exactly in the mid distance between the V-notches, one specimen was instrumented with a third strain gage on the back face in order to validate the strains measured by the pair of gages. No significant differences were found between the measurements. Figure 3.27 a, b and c shows the tabbed specimens before and after being tested, as well as the specimen

with the third strain gage. The failure mode occurred between the V-notches, as expected.

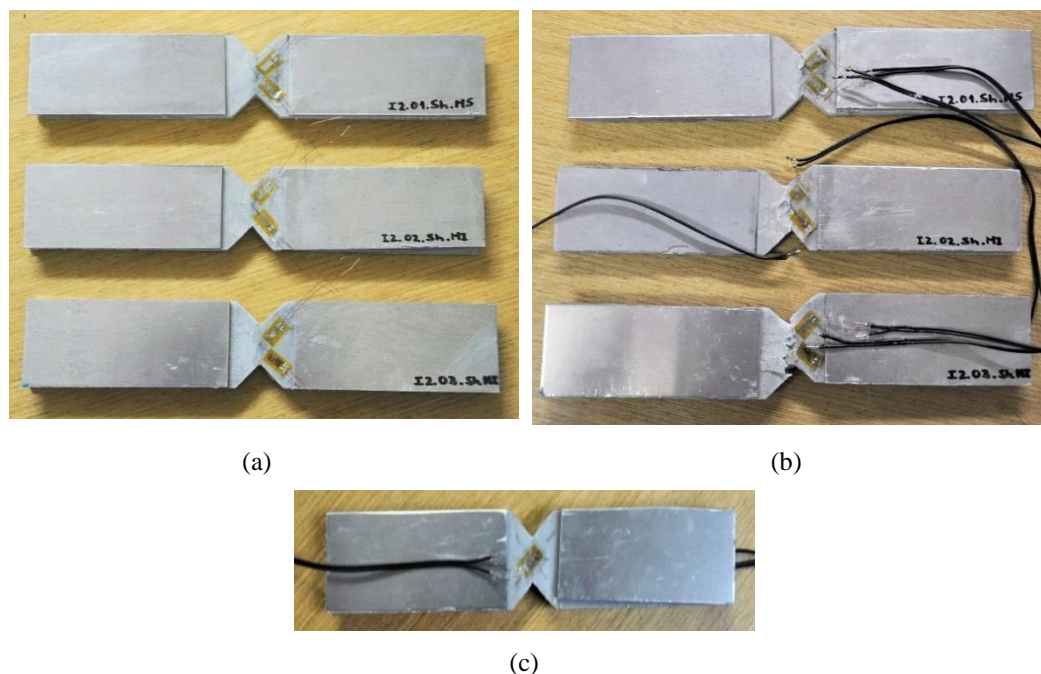


Figure 3.27 – Tabbed specimens: (a) before being tested; (b) after being tested with failure between the V-notches; (c) third 45 deg strain gage positioned in the back of the specimen

The average specimens dimensions with their respective standard deviations are presented in Table 3.18, along with the coupon depth in V-notched region d_v (Figure 3.26).

Table 3.18 – Specimens dimensions

<i>Specimen's Dimensions</i>	<i>I₂</i>
t (mm)	6.36 ± 0.07
b (mm)	38.39 ± 0.25
L (mm)	200.60 ± 0.04
d_v (mm)	17.89 ± 0.31

To ensure the load distribution, the V-notched details were aligned with the load applied axis with the aid of a laser machine, as shown in Figure 3.28.

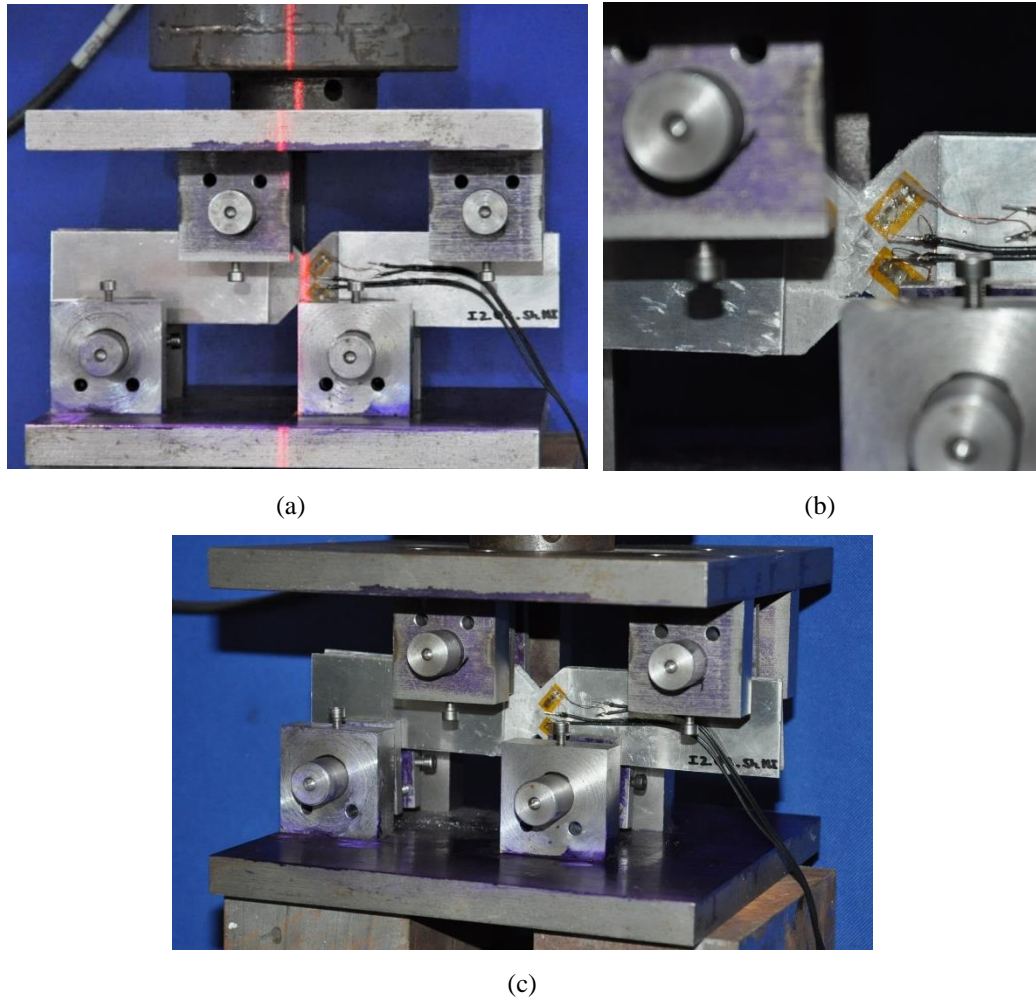


Figure 3.28 – Iosipescu test: (a) alignment with load applied axis; (b) failure in pure shear stress region; (c) test fixture's overview

The shear modulus was obtained as the slope of the shear stress across the notched section (τ_{LT}) *versus* the shear strain (γ_{LT}) plot, where γ_{LT} is determined as the sum of the absolute values captured by the strain gages ($\gamma_{LT} = \epsilon_{-45^\circ} + \epsilon_{+45^\circ}$). Figure 3.29 illustrates the shear diagram based on the test apparatus' dimensions. As can be seen, the internal shear in the central portion region corresponds to 50% of the total applied load P . Thus, the shear stress across the notched section τ is given by Eq. 3.11. It is important to point out that this equation assumes uniform shear strain distribution across the specimen depth.

$$\tau = \frac{0,5 P}{d_v t} \quad (3.11)$$

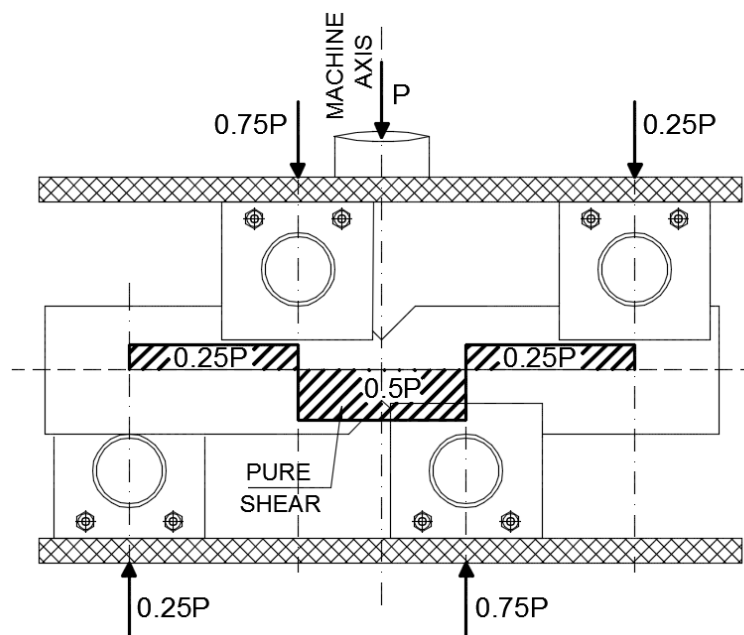


Figure 3.29 - Shear diagram based on test fixture's dimensions

The τ versus γ plots obtained are illustrated in Figure 3.30. A non-linear shear behavior was observed. The in-plane shear modulus was taken as the chord modulus comprehended between strains 0.001 and 0.006 of stress-strain curve, similarly to previous tests reported in literature (*e.g.* ZUREICK and SCOTT, 1997). The average results are presented in Table 3.19.

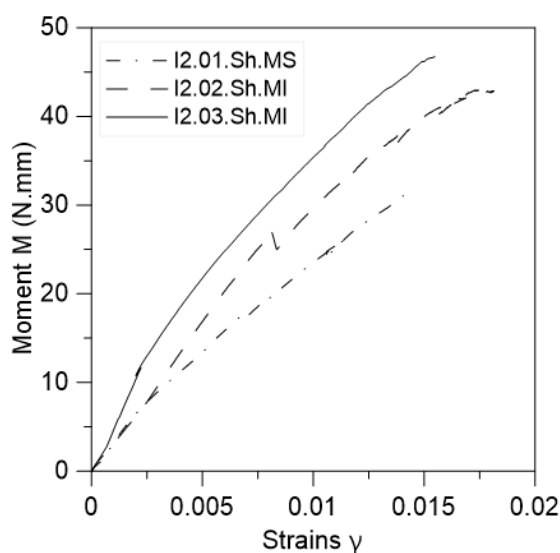


Figure 3.30 - τ versus γ plot

Table 3.19 - Shear modulus of specimens from I_2

<i>Specimen</i>	<i>G_{LT}</i> (GPa)
<i>I₂.01.Sh.MS</i>	2.43
<i>I₂.02.Sh.MI</i>	3.51
<i>I₂.03.Sh.MI</i>	3.45
Average:	3.13 ± 0.61
cov⁽¹⁾	0.194

⁽¹⁾ Coefficient of variation

The average shear modulus obtained through Iosipescu test ($G_{LT} = 3.13$ GPa) was very close to the one found through the torsion tests ($G_{LT} = 3.11$ GPa), validating the results. In order to obtain the local buckling critical loads for I_2 profiles, the shear modulus of 3.13 GPa was used.

3.2.5. Compressive Modulus ($E_{L,c}$) and Strength ($F_{L,c}$)

The difficulty in determining the true compressive strength is to produce compression failure while avoiding severe stress concentrations at loaded ends, loading eccentricity and member buckling (ADAMS *et al.*, 2003). With the purpose of obtaining the compressive properties, three test methods may be adopted: an *end loading* test (ASTM D695-15), a *shear loading* test (ASTM D3410-16) or a *combined loading compression* (CLC) test (ASTM D6641-16). In previous studies, standard compressive tests on longitudinal coupons have been performed by ZUREICK and SCOTT (1997), ZUREICK and STEFFEN (2000), according to ASTM D3410 and by TOGASHI (2017) according to ASTM D6641.

In this work, CLC tests were conducted in order to obtain the compressive strengths and moduli. In this test method, the favorable features of both end and shear loading tests are combined and the objective is to achieve sufficient shear loading to eliminate end crushing (ADAMS *et al.*, 2003). Five and six specimens 15-mm wide x 155-mm long were extracted from I_1 and I_2 profiles, respectively. Dimensions were measured with a digital caliper and the averages and standard deviations are presented in Table 3.20.

Table 3.20 - Specimens' Dimensions - Compression Test

<i>Specimens' dimensions</i>	I_1	I_2
b (mm)	15.42 ± 2.19	15.40 ± 3.02
t (mm)	9.58 ± 1.22	6.30 ± 2.01
L (mm)	155	155

To avoid undesirable end crushing, the coupons were tabbed with aluminum plates of 2-mm, glued to the composite with an epoxy resin (Sikadur-32).

Specimens untabbed and tabbed of both profiles are respectively shown in Figure 3.31 and Figure 3.32.

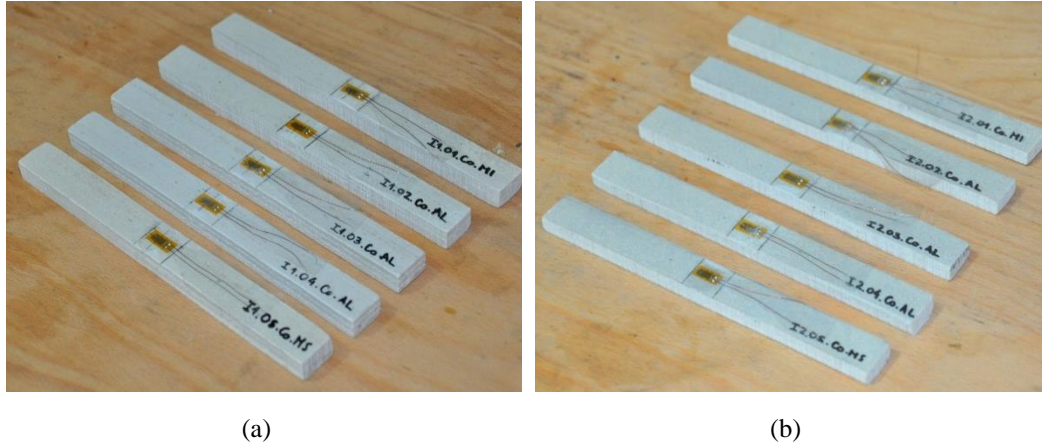


Figure 3.31 - Untabbed Specimens: (a) extracted from I₁; (b) extracted from I₂

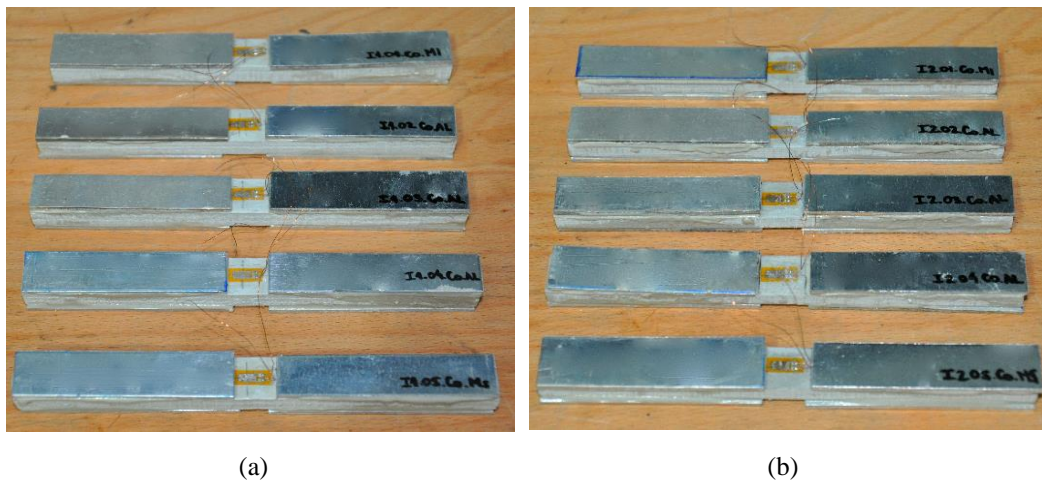


Figure 3.32 - Tabbed Specimens: (a) extracted from I₁; (b) extracted from I₂

For this work, an adapted test apparatus was fabricated and its dimensions are shown in Figure 3.33. The test consisted of loading the specimen between flat plates and the ratio of shear to end loading was controlled by the torque of 13 N.m applied in the clamping screws. The test was conducted under a displacement controlled rate of 1.3 mm/min on a *MTS model 810* universal testing machine with load capacity of 500 kN. The strains were measured using strain gages positioned on the middle of the specimen's face. According to the adopted standard, failure is acceptable if it occurs within the gage length. Figure 3.34 shows the test fixture and the specimen's failure within the gage length.

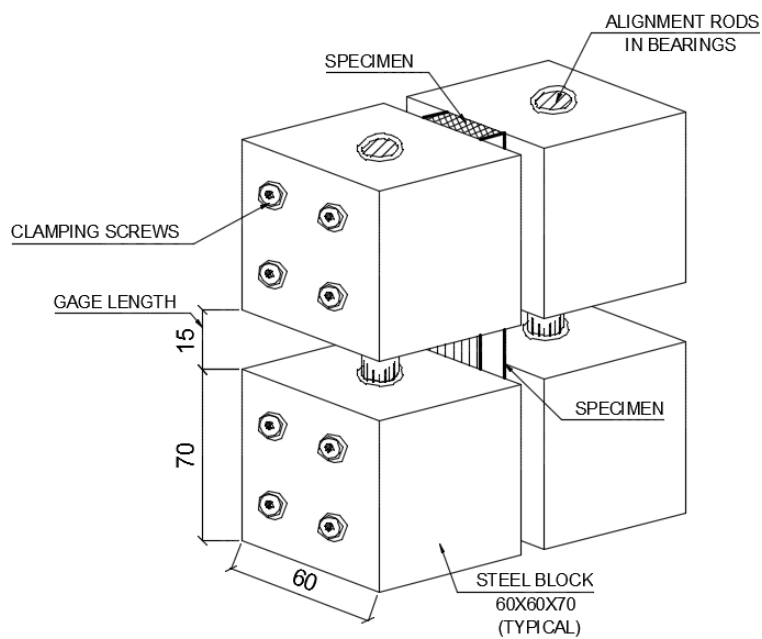
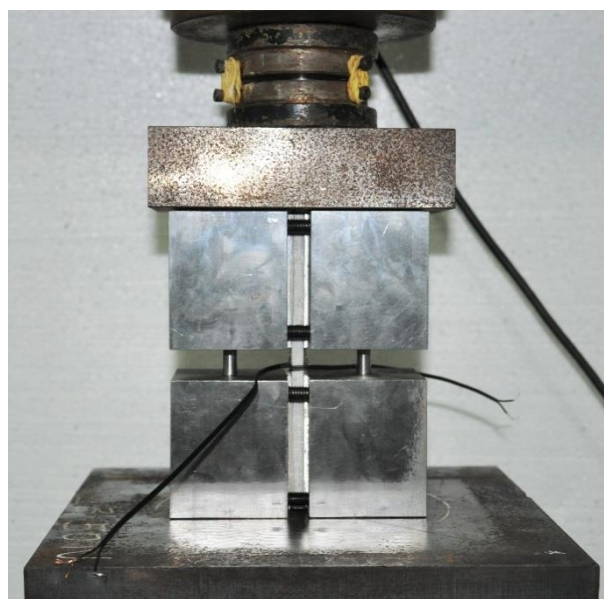
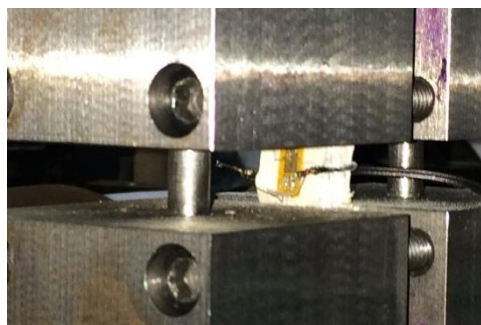


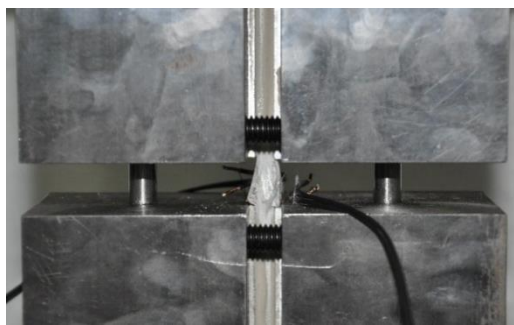
Figure 3.33 - CLC Test Scheme (dimensions in mm)



(a)



(b)



(c)

Figure 3.34 – CLC test: (a) test fixture; (b) detail of gage length; (c) failure within the gage length

Buckling of coupon within gage length must also be prevented. As it is not possible to detect buckling by visual inspection during the test, one of the specimens of each section was instrumented with back-to-back strain gages in order to confirm ‘pure compression’. Figure 3.35 presents the compressive stress plotted against the strains for the back-to-back gages of each profile (I_1 and I_2). As can be noticed, Figure 3.35a apparently shows flexure, which may be explained by an eccentricity due to the misalignment of the fibers. Even though, the displacements did not experience a quickly growth and therefore, any buckling was identified.

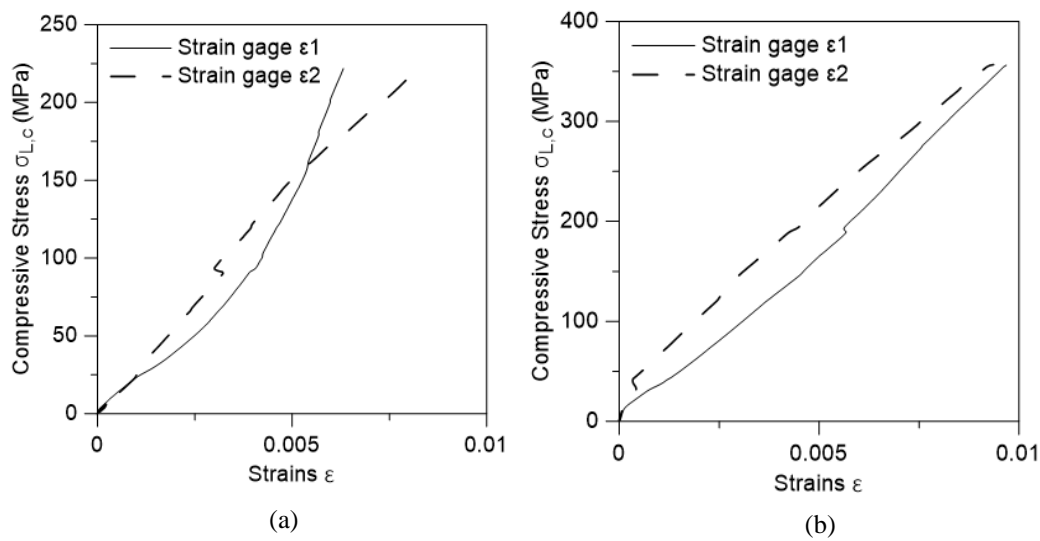


Figure 3.35 - Strains measurements to ensure that buckling would not occur: (a) Strains measurements of specimen $I_{1.05.Co.AL}$; (b) Strains measurements of specimen $I_{2.06.Co.MI}$

The moduli of elasticity were obtained as the slope of the plot of axial compressive strength ($F_{L,c}$) *versus* measured average strain (ϵ). In the cases of specimens with two strain gages, the average strain was used. The compressive strengths were determined as the stresses immediately before an observed sudden drop of the load, by using Eq. 3.12.

$$\sigma_{L,c} = \frac{P}{b t} \quad (3.12)$$

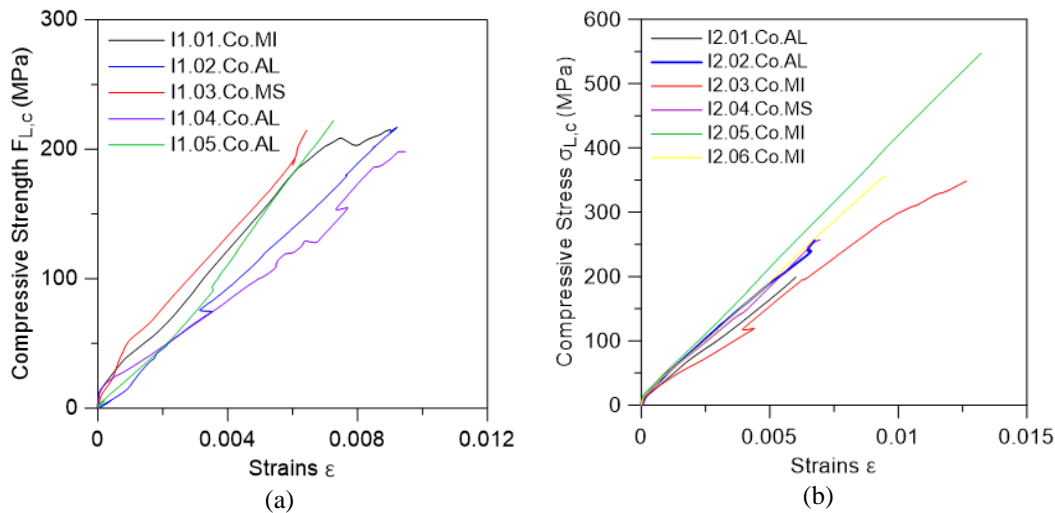


Figure 3.36 - Stress-strain curves: (a) Coupons extracted from I₁; (b) Coupons extracted from I₂

The compressive moduli were obtained as the slope of the linear portion of the plot, usually between 20% to 55% of the maximum strength reached by the sample. Tables 3.21 and 3.22 present the average compressive moduli and Tables 3.23 and 3.24 present the average compressive strengths $F_{L,c}$ for both profiles.

Table 3.22 - Compressive Modulus of I₁

<i>Specimen</i>	<i>E_{L,c} (GPa)</i>
<i>I₁.01.Co.MI</i>	29.63
<i>I₁.02.Co.AL</i>	23.18
<i>I₁.03.Co.MS</i>	27.79
<i>I₁.04.Co.AL</i>	17.14
<i>I₁.05.Co.AL</i>	23.59
Average:	24.27 ± 4.38
cov⁽¹⁾	0.178

⁽¹⁾Coefficient of variation

Table 3.21 - Compressive Modulus of I₂

<i>Specimen</i>	<i>E_{L,c} (GPa)</i>
<i>I₂.01.Co.AL</i>	32.18
<i>I₂.02.Co.AL</i>	33.12
<i>I₂.03.Co.MI</i>	33.11
<i>I₂.04.Co.MS</i>	32.97
<i>I₂.05.Co.MI</i>	40.33
<i>I₂.06.Co.MI</i>	37.11
Average:	33.70 ± 1.75
cov⁽¹⁾	0.052

⁽¹⁾Coefficient of variation

Table 3.23 - Compressive Strength of I₁

<i>Specimen</i>	<i>F_{L,c} (MPa)</i>
<i>I_{1.01.Co.MI}</i>	220.37
<i>I_{1.02.Co.AL}</i>	217.24
<i>I_{1.03.Co.MS}</i>	213.88
<i>I_{1.04.Co.AL}</i>	198.31
<i>I_{1.05.Co.AL}</i>	221.61
Average:	214.28 ± 8.42
cov⁽¹⁾	0.039

⁽¹⁾Coefficient of variationTable 3.24 - Compressive Strength of I₂

<i>Specimen</i>	<i>F_{L,c} (MPa)</i>
<i>I_{2.01.Co.AL}</i>	199.16
<i>I_{2.02.Co.AL}</i>	259.47
<i>I_{2.03.Co.MI}</i>	349.27
<i>I_{2.04.Co.MS}</i>	257.18
<i>I_{2.05.Co.MI}</i>	547.30
<i>I_{2.06.Co.MI}</i>	356.28
Average:	283.65 ± 60.27
cov⁽¹⁾	0.212

⁽¹⁾Coefficient of variation

As can be observed, the sample I_{2.05.Co.MI} presented much greater strength and modulus if compared to the other specimens. This may be due to a higher fiber volume fraction presented in this sample. To avoid dispersion of results, this specimen was considered as an outlier and its data were discarded.

Although the profiles presented similar fiber volume ratios, it can be noticed that I₂ sections presented average strength 32% higher than I₁ profiles. This may be explained by the fact that mechanical properties of the matrices have a certain influence on the compressive strength.

3.2.6. Summary of Material Properties

The mechanical properties obtained by characterization tests were compared with theoretical predictions obtained by the Rule of Mixture and the Halpin-Tsai equations, which were based on the isotropy assumption for the constituent materials:

- the elastic tensile and compressive properties ($E_{L,t}$ and $E_{L,c}$) were assumed to be equal;
- the transverse flexural and tensile modulus ($E_{T,f}$ and $E_{T,i}$) of the fibers were assumed to be equal;

iii. the shear moduli for fibers and resins can be obtained by the well-known Eq. 3.13:

$$G = \frac{E}{2(1 + \nu)} \quad (3.13)$$

where E and ν are the corresponding elasticity modulus and Poisson's ratio.

Table 3.24 - Elastic properties of fibers and resins

Mechanical Properties	Fiber (GPa)	Polyester (GPa)	Vinyl Ester (GPa)
E	72.50 ⁽¹⁾	4.00 ⁽¹⁾	3.50 ⁽¹⁾
G	28.88	1.54	1.35
ν	0.26 ⁽²⁾	0.30	0.30 ⁽²⁾

(1) BANK (2006)

(2) DAVALOS (1996)

The prediction of the longitudinal flexural modulus is based on the classic laminated theory and it will not be addressed in this work. The CSM layers were taken into account through equations 2.6 and 2.7, presented in Chapter 2. The experimental and theoretical elastic properties are presented in Table 3.25.

Table 3.25 – Summary of material properties obtained experimentally and comparison with theoretical prediction

Mechanical Properties	I₁			I₂		
	<i>Exp.</i> ⁽¹⁾	<i>ROM</i> ⁽²⁾	<i>H.T.</i> ⁽³⁾	<i>Exp.</i> ⁽¹⁾	<i>ROM</i> ⁽²⁾	<i>H.T.</i> ⁽³⁾
<i>F_{L,f}</i> (MPa)	265.65	-	-	384.23	-	-
<i>E_{T,f}</i> (GPa)	5.84	8.9	10.4	7.75	8.2	12.9
<i>G_{LT}</i> (GPa)	2.26	3.4	4.1	3.13	3.1	4.1
<i>E_{L,c}</i> (GPa)	24.27	29.3	29.5	33.70	33.3	33.8
<i>F_{L,c}</i> (MPa)	214.28	-	-	283.65	-	-
<i>V_{roving}</i> (%)	32.81			39.94		

(1) Experimental data

(2) Rule of Mixtures

(3) Halpin-Tsai Equation

It can be observed that most of predictions obtained by Rule of Mixtures (ROM) are closer to experimental data than the ones obtained by Halpin Tsai equation. Further, in general the theoretical properties were higher than the ones obtained experimentally.

3.3. Stub Column Tests

Pultruded GFRP stub columns having different flange width-to-section depth ratios (b_f/d) were tested in compression to study the influence of length and end-conditions on the local buckling behavior. In each test, *column* bases rotations were restrained about minor and major axes, *i.e.*, fixed end conditions were adopted for each column (FF). On the other hand, three end-conditions were considered for the *plates* comprising the cross-section: simply-supported (SS), clamped (CC) and simply in contact with base plates (CB). For the third end-condition, plates are not entirely free to rotate, thus reproducing neither a clamped nor a simply-supported boundary-condition. This condition has been adopted by many authors and is also studied in the present work for comparison with controlled end-conditions.

Table 3.26 presents the 29 tested stubs. Two different lengths were selected for each cross-section and end-condition.

Table 3.26 - Local Buckling Tests Summary

<i>Plates end condition</i>	<i>Section</i>	<i>Short Columns</i>		<i>Long Columns</i>	
		<i>N⁽¹⁾</i>	<i>L (mm)</i>	<i>N⁽¹⁾</i>	<i>L (mm)</i>
<i>Clamped</i>	I ₁	3	300	3	600
	I ₂	3	250	3	550
	I ₃	3	300	3	550
				1	495
<i>Simply-supported</i>	I ₃	3	300	3	550
<i>In Contact with plates</i>	I ₃	2	300	2	550

(1) Number of specimens tested

Column lengths were determined based on the signature curve provided by the software *GBTUL 2.0* in order to ensure ‘pure’ local buckling. All tests were conducted under displacement control at a rate of 0.6 mm/min until failure using a servo-hydraulic universal testing machine *MTS model 810* with a load capacity of 500 kN.

In order to identify the stub columns, an alphanumeric code was used, as presented in Figure 3.37. The first set refers to the studied profile (I_1 , I_2 or I_3). The second corresponds to the polymeric matrix used in the composite, whereas the third and fourth sets refer to the test number and column length, respectively. In some tables throughout this work, the stubs will be identified only by the first and third set for simplicity.

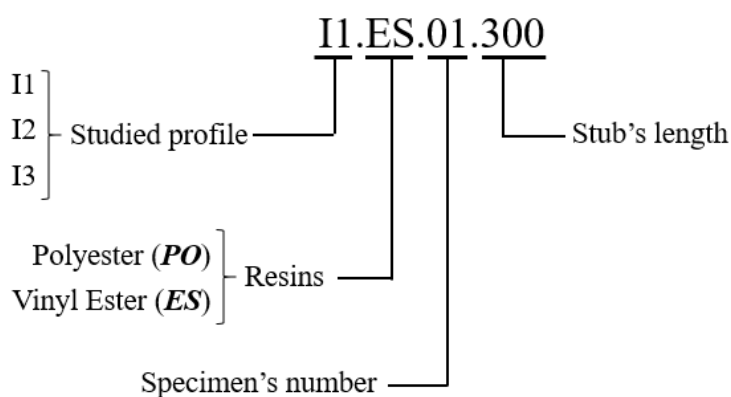


Figure 3.37 - Alphanumeric code for stub identification

With the exception of one column (described in section 3.3.1.1), all stubs were instrumented with four displacements transducers, identified in Figure 3.38. Two of them (1 and 2) were positioned at the tips of one of the flanges and the third on the web (3), being all located at the point where maximum out-of-plane deflections were expected, determined using software *GBTul*. Transducer 4 was positioned on the base plate in order to measure the axial shortening of column. In each test, photos were taken every five seconds with a *Nikon D90* in order to monitor lateral deflection growth. Figure 3.39 presents a general view with the equipment used to record data during test.

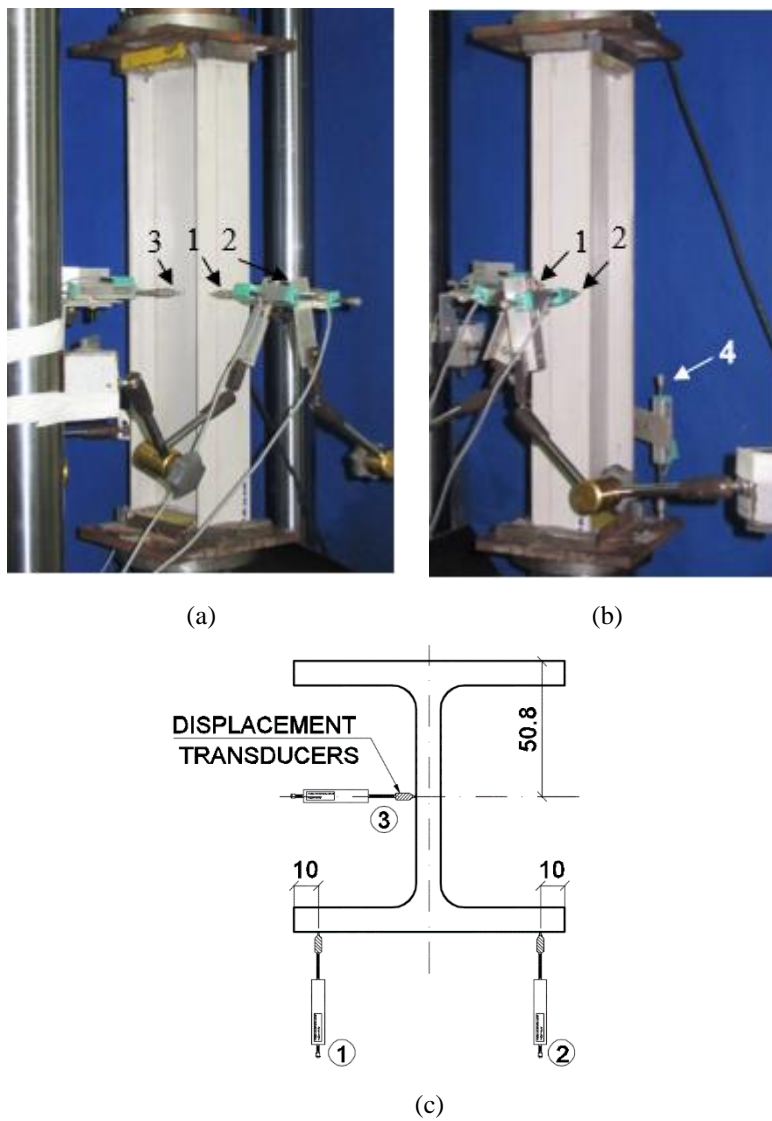


Figure 3.38 – Displacements transducers: (a) transducers 1 to 3; (b) transducers 1,2 and 4; (c) transducers' location (mm)



Figure 3.39 – Equipment required for the tests

3.3.1. Columns with Clamped Edges

Nineteen stubs were submitted to concentric compression, having the *plates edges* clamped at both ends. As previously mentioned, one of them was instrumented with strain gages and its setup will be particularly discussed in Section 3.3.1.1. The other eighteen stubs dimensions (in mm), measured with a digital caliper, are presented in Table 3.27, as well as the calculated cross-sectional areas A and chosen lengths. The ratios between average measured dimensions (MD) and nominal dimensions (ND) are presented in Table 3.28.

Table 3.27 - Average cross-section dimensions, lengths and calculated areas.

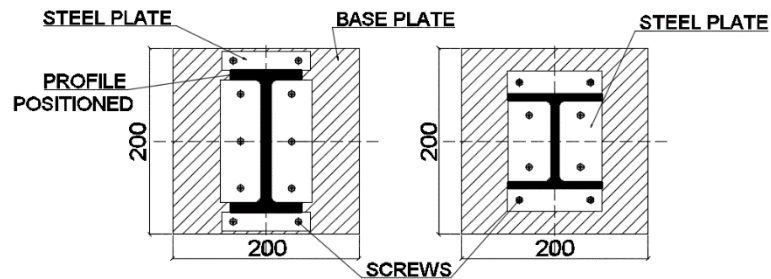
<i>Stub</i>	<i>L</i> (mm)	<i>b_f</i> (mm)	<i>t_f</i> (mm)	<i>d</i> (mm)	<i>t_w</i> (mm)	<i>b_w</i> (mm)	<i>b_f/d</i> (mm)	<i>A</i> (mm ²)
<i>I_{1.01}</i>	300	76.30	9.90	153.70	9.70	143.80	0.50	2809.57
<i>I_{1.02}</i>	300	76.40	10.00	153.50	9.80	143.50	0.50	2836.30
<i>I_{1.03}</i>	300	76.45	10.00	153.10	10.00	143.10	0.50	2860.00
<i>I_{1.04}</i>	600	76.20	9.90	152.70	9.90	142.80	0.50	2824.47
<i>I_{1.05}</i>	600	76.05	9.70	153.00	9.20	143.30	0.50	2704.49
<i>I_{1.06}</i>	600	76.30	9.85	152.90	9.70	143.05	0.50	2795.15
<i>I_{2.01}</i>	250	74.30	6.15	100.40	6.45	94.25	1.01	1482.14
<i>I_{2.02}</i>	250	73.80	6.00	100.40	6.35	94.40	1.01	1446.94
<i>I_{2.03}</i>	250	75.50	6.50	100.50	6.35	94.00	1.00	1537.13
<i>I_{2.04}</i>	550	74.20	6.10	100.95	6.45	94.85	1.00	1477.68
<i>I_{2.05}</i>	550	75.05	6.00	100.95	6.60	94.95	1.00	1487.67
<i>I_{2.06}</i>	550	72.60	6.25	100.85	6.55	94.60	1.01	1486.19
<i>I_{3.01}</i>	300	101.10	6.17	100.00	6.45	93.83	0.74	1812.98
<i>I_{3.02}</i>	300	100.88	6.33	100.00	6.55	93.67	0.74	1849.22
<i>I_{3.03}</i>	300	100.90	6.20	100.70	6.40	94.50	0.75	1816.28
<i>I_{3.04}</i>	550	101.40	6.35	101.10	6.65	94.75	0.74	1875.64
<i>I_{3.05}</i>	550	100.70	6.42	100.95	6.69	94.53	0.74	1882.44
<i>I_{3.06}</i>	550	101.47	6.24	100.70	6.52	94.46	0.72	1841.54

Table 3.28 – Ratio of average measured and nominal dimensions

		<i>MD</i> (mm)	<i>ND</i> (mm)	<i>MD/ND</i> (mm)
<i>I₁</i>	<i>b_f</i>	76.28	76.20	1.001
	<i>t_f</i>	9.89	9.50	1.041
	<i>d</i>	153.15	152.40	1.005
	<i>t_w</i>	9.72	9.50	1.023
<i>I₂</i>	<i>b_f</i>	74.24	76.20	0.974
	<i>t_f</i>	6.17	6.40	0.964
	<i>d</i>	100.68	101.60	0.991
	<i>t_w</i>	6.46	6.40	1.009
<i>I₃</i>	<i>b_f</i>	101.08	101.60	0.995
	<i>t_f</i>	6.29	6.40	0.982
	<i>d</i>	100.58	101.60	0.990
	<i>t_w</i>	6.54	6.40	1.022

In order to avoid the edges rotation, 19-mm thick steel plates attached with screws to the base plates were used. To ensure uniform loading and to fill in a gap

of 3.5 mm between the column's edges and steel plates, *Iberê* plastic filler material was applied between the base plates and the profile. Figure 3.40 presents schemes and pictures of the test setup.



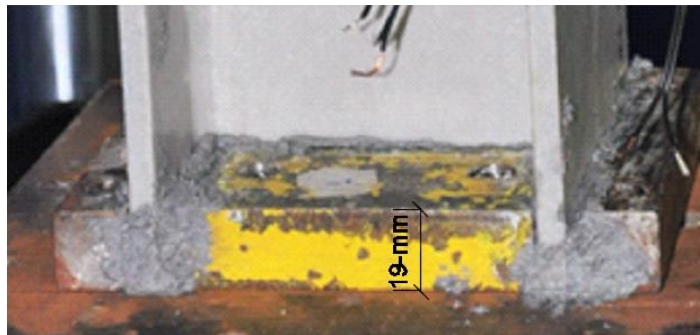
(a)



(b)



(b)



(d)

Figure 3.40- Set-up used to avoid plates edges rotation: (a) Test fixture scheme for I_1 (on the left) and I_2 (on the right); (b) steel plates fixed on the base plate; (c) profile being regularized with filler material; (d) clamped wall end-condition

3.3.1.1. Stub instrumented with strain gages

In order to evaluate the strain distribution throughout cross-section due to post-critical path, a 495-mm long I_3 profile instrumented with twelve strain gages was tested. The gages were positioned on the center of the web and flanges, as

shown in Figure 3.41. The average measured dimensions (MD), as well as the cross-sectional area are presented in Table 3.29, as well as the ratio between measured and nominal dimensions (ND).

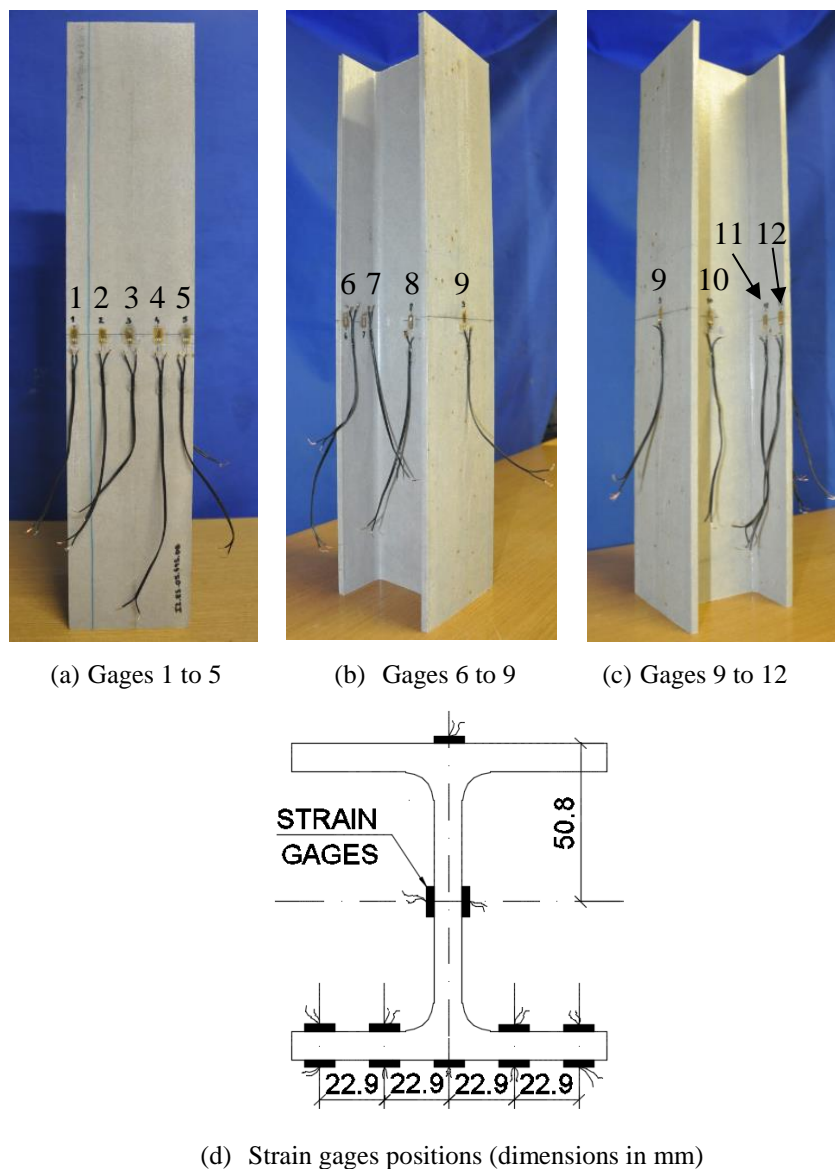


Figure 3.41 – Numbering and gages positions: (a) gages 1 to 5; (b) gages 6 to 9; (c) gages 9 to 12; (d) strain gages positions (dimensions in mm)

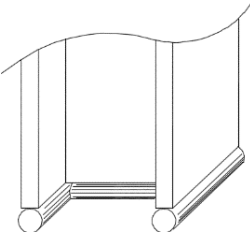

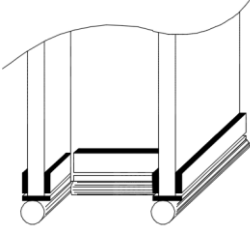

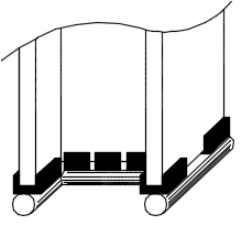

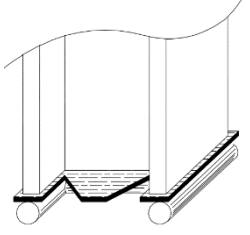

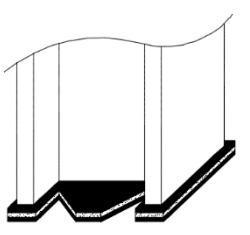

Table 3.29 - Average dimensions of I3.ES.07.495 and ratio of measured and nominal dimensions

<i>I_{3.07}</i>	<i>L</i> (mm)	<i>b_f</i> (mm)	<i>t_f</i> (mm)	<i>d</i> (mm)	<i>t_w</i> (mm)	<i>b_w</i> (mm)	<i>b_f/d</i> (mm)	<i>A</i> (mm ²)
MD	495	101.35	6.33	101.20	6.50	94.88	1.00	1857.65
ND		101.60	6.40	101.60	6.40			
MD/ND		0.998	0.988	0.996	1.016			

3.3.1. Columns with Simply Supported Edges

One of the major challenges of this work was the reproduction of a boundary condition as close as possible to an ideal column with simply-supported plates. Many attempts were made in order to ensure that the edges would be free to rotate, but with translation restrained. Rollers were used for this purpose in most of attempts. Although carefully positioned and leveled before being welded to the end plates, leveling of columns and alignment with rollers were major issues in the tests because of column imperfections. Most of attempts were conducted on I₃-section profiles, once they are more susceptible to local buckling, presenting larger deflections and allowing better and easier test monitoring. The principal attempts are described in Table 3.30.

Table 3.30 - Attempts to reproduce a column with simply supported plates edges

	<i>Scheme</i>	<i>Picture</i>	<i>Attempt description</i>
<i>Attempt 1</i>			<p><u>Set-up</u>: column's plates supported directly on a roller.</p> <p><u>Failure</u>: localized end crushing due to reduced area of contact.</p>
<i>Attempt 2</i>			<p><u>Set-up</u>: 2-mm thick aluminum tabs were glued with epoxy resin to the specimen close to the loading point</p> <p><u>Failure</u>: the plates came off and the profile experienced end crushing.</p>
<i>Attempt 3</i>			<p><u>Set-up</u>: column's plates were fit in segmented steel channels supported on the rollers.</p> <p><u>Difficulties</u>: The sheets accentuated the profile's imperfections and provided an undesirable torsional stiffness.</p> <p><u>Failure</u>: Block shear due to stresses concentration.</p>
<i>Attempt 4</i>			<p><u>Set-up</u>: edges supported on a pultruded GFRP plate over the rollers, with the fibers oriented parallel to the web.</p> <p><u>Failure</u>: GFRP plate failure</p>
<i>Attempt 5</i>			<p><u>Set-up</u>: edges supported on a base made of two aluminum plates with a neoprene between them.</p> <p><u>Failure</u>: Neoprene ended up crushing and the plates were not able to rotate at the bottom, behaving similarly to a clamped plate end-condition.</p>

A suitable result was reached when a 2-mm steel 'I' sheet was placed between the rollers and the stubs, as shown in Figure 3.42 a and b. In order to reduce steel sheet torsional stiffness, allowing it to accompany rotation of the plates, cuts were introduced in their corners. To avoid leveling problems, columns had their ends machined using a table saw.

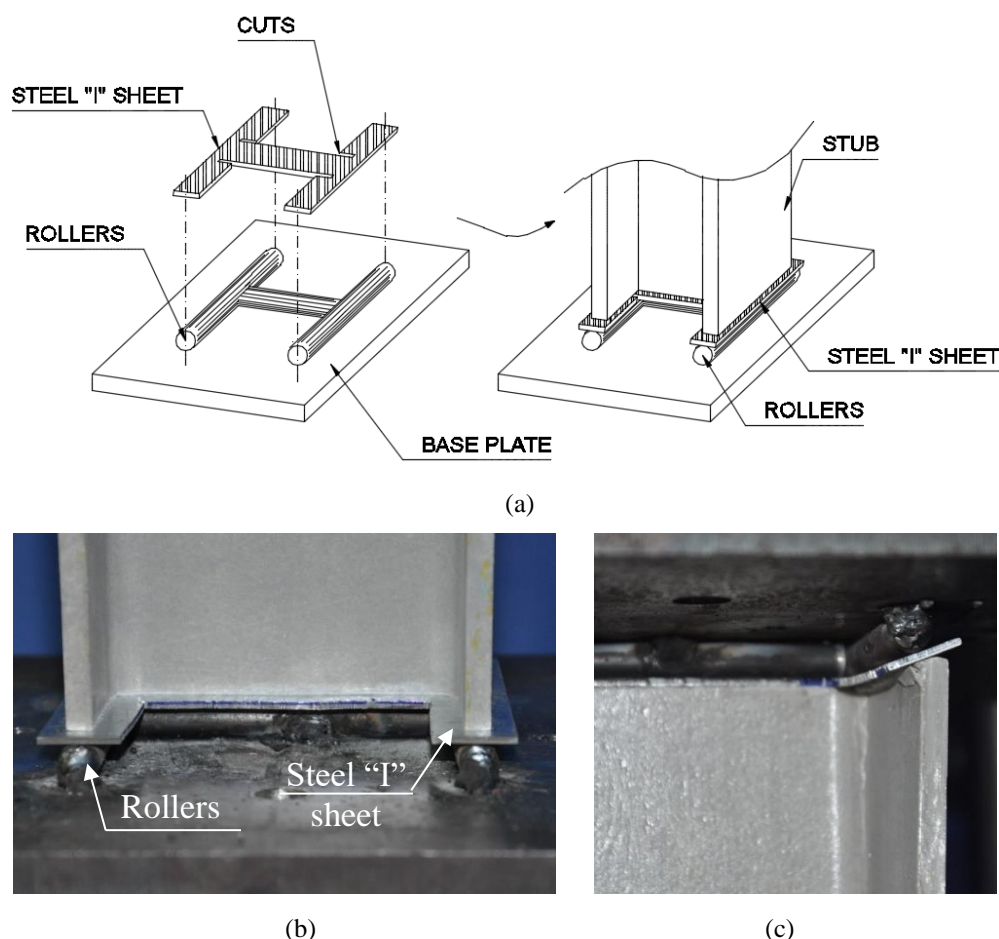


Figure 3.42 – Set-up for simply-supported plates: (a) scheme of the set-up; (b) simply supported plates; (c) column sliding off the roller axis

In some attempts, the I_3 -section profile slid off the rollers axis, as shown in Figure 3.44b. Therefore, to brace the column laterally, a fixture consisting of four steel angles and screws was used, as shown in Figure 3.43. Steel angles were welded to the end plates and sets of screw and nuts were connected to them while in contact with the middle of column flanges, thus preventing slippage and allowing plates motions. Screws were only finger-tightened and a rounded-shape nut was used in the screw end in contact with column to avoid damaging the GFRP profile.

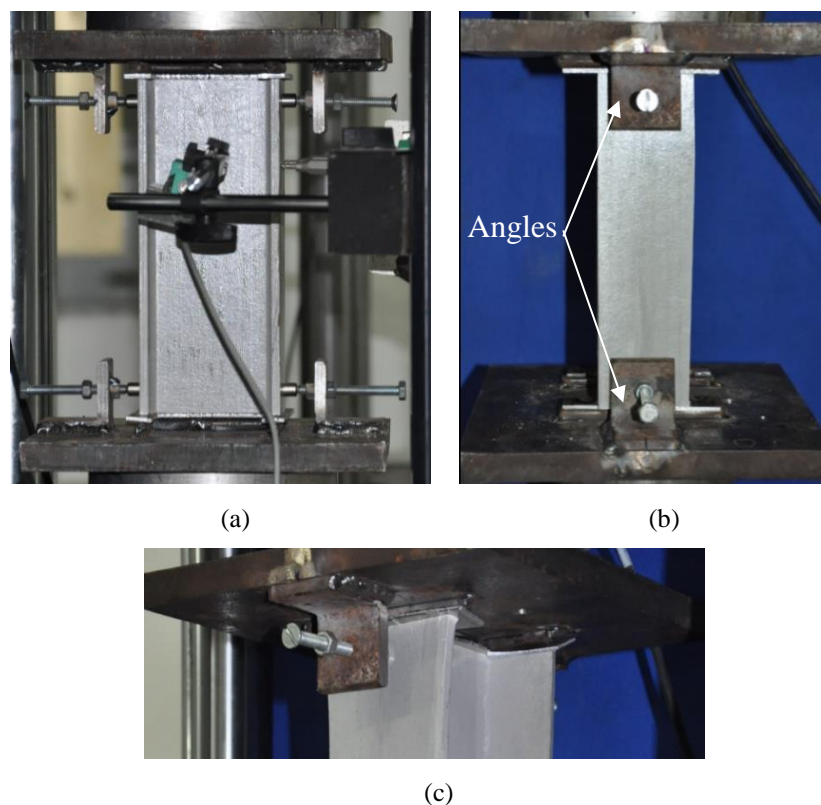


Figure 3.43 - Final set-up for simply supported plates: (a) Lateral view; (b) Frontal view; (c) Overview

Nevertheless, the existence of imperfections due to manufacturing process were a considerable obstacle in this test fixture, especially on longer stubs. Even with the described apparatus, some tested stubs slid off the rollers before reaching their ultimate failure, as shown in Figure 3.44. The tests results are presented in Chapter 4.

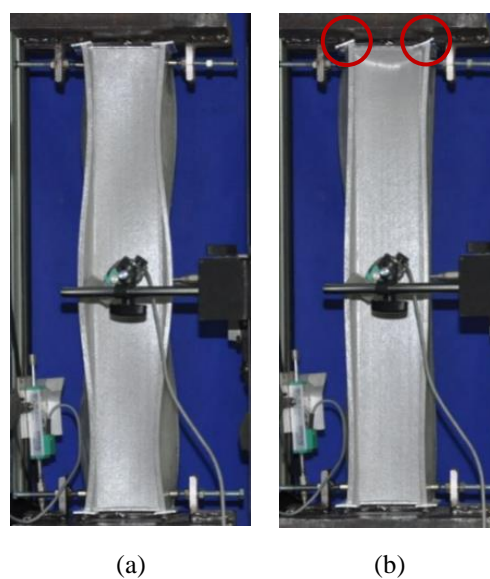


Figure 3.44 – Slippage of long columns off the rollers: (a) Before; (b) After

The I_3 column sizes were measured with a digital caliper and their average are indicated in Table 3.31, as well as their calculated cross-sectional areas and lengths. The ratios of the average measured dimensions (MD) and nominal dimensions (ND) are presented in Table 3.32.

Table 3.31 - Average dimensions and cross-sectional area of simply supported stubs

<i>Stub</i>	<i>L</i> (mm)	<i>b_f</i> (mm)	<i>t_f</i> (mm)	<i>d</i> (mm)	<i>t_w</i> (mm)	<i>b_w</i> (mm)	<i>b_f/d</i> (mm)	<i>A</i> (mm ²)
<i>I_{3.01}</i>	300	101.20	6.20	101.20	6.45	95.00	1.00	1827.64
<i>I_{3.02}</i>	300	101.27	6.22	101.30	6.47	95.08	1.00	1834.72
<i>I_{3.03}</i>	300	101.21	6.29	101.10	6.49	94.81	1.00	1847.72
<i>I_{3.04}</i>	550	101.31	6.36	101.25	6.50	94.89	1.00	1864.11
<i>I_{3.05}</i>	550	101.30	6.28	101.30	6.53	95.02	1.00	1851.80
<i>I_{3.06}</i>	550	101.10	6.23	101.20	6.50	94.98	1.00	1835.57

Table 3.32 - Ratio of average measured dimensions and nominal dimensions

	<i>MD</i> (mm)	<i>ND</i> (mm)	<i>MD/ND</i> (mm)
<i>b_f</i>	101.20	101.60	0.996
<i>t_f</i>	6.20	6.40	0.969
<i>d</i>	101.20	101.60	0.996
<i>t_w</i>	6.45	6.40	1.008

3.3.2. Columns Directly in Contact with Base Plates

In order to compare the local buckling behavior observed in the present work for columns with controlled end conditions with those reported in literature, a third boundary condition was analyzed. Four I_3 stubs were tested with their plates simply in contact with the base plates, as shown in Figure 3.45.

Average stubs dimensions are presented in Table 3.33, along with their calculated cross-sectional areas and lengths. The ratios of the average measured dimensions (MD) and nominal dimensions (ND) are presented in Table 3.34.



Figure 3.45 – Plates simply in contact with base plate

Table 3.33 – Average stubs dimensions, cross-sectional areas and lengths

<i>Stub</i>	<i>L</i> (mm)	<i>b_f</i> (mm)	<i>t_f</i> (mm)	<i>d</i> (mm)	<i>t_w</i> (mm)	<i>b_w</i> (mm)	<i>b_f/d</i> (mm)	<i>A</i> (mm ²)
<i>I_{3.01}</i>	300	101.32	6.43	101.15	6.60	94.73	1.00	1884.74
<i>I_{3.02}</i>	300	101.35	6.33	101.50	6.65	95.18	1.00	1872.93
<i>I_{3.03}</i>	550	101.25	6.40	101.20	6.60	94.80	1.00	1879.44
<i>I_{3.04}</i>	550	101.35	6.45	101.10	6.50	94.65	1.00	1880.72

Table 3.34 - Ratio of average measured dimensions and nominal dimensions

	<i>MD</i> (mm)	<i>ND</i> (mm)	<i>MD/ND</i> (mm)
<i>b_f</i>	101.32	101.60	1.00
<i>t_f</i>	6.40	6.40	1.00
<i>d</i>	101.24	101.60	1.00
<i>t_w</i>	6.59	6.40	1.03

4. Results Analyzes

4.1. Overview

In this Chapter, the stub column tests results are reported and discussed. All experimental critical loads were determined by the Southwell plot (SOUTHWELL, 1932). Figure 4.1 illustrates a representative Southwell plot of one tested I₃-section stub. As can be noticed, Southwell plot is clearly nonlinear and fitting a straight line is not an easy task. In fact, the critical loads change according to the interval considered and, in this work, an attempt was made to consider an ‘initial slope’, therefore avoiding the strong influence of nonlinear stress distribution in the moderate to large deflections range. Unfortunately, each column has a particular behavior and a fixed interval cannot be set for all the tests. The plots for the twenty-eight tested stubs are shown in Appendix A and a discussion of the results is presented in the following paragraphs. The plots for the twenty-ninth column (particularly instrumented with strain gages) is presented in the following sections.

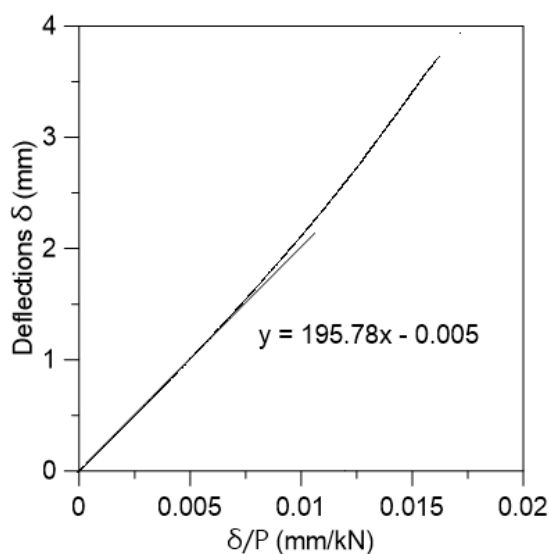


Figure 4.1 - Representative Southwell plot of I3.ES.04.550

4.2. Columns with Clamped Edges

The overviews of the shorter tested stubs (250-300 mm) are shown in Figure 4.2, whereas Figures 4.3 to 4.5 present a photo sequence of the longer tested columns (550-600 mm). It can be observed that specimens having $b_f/d = 1.0$ exhibited large deflections, whereas negligible motions could be observed for columns having $b_f/d = 0.5$. Stub columns having 0.75 constituted an intermediate case. The number of half-waves formed were also in accordance with prediction.

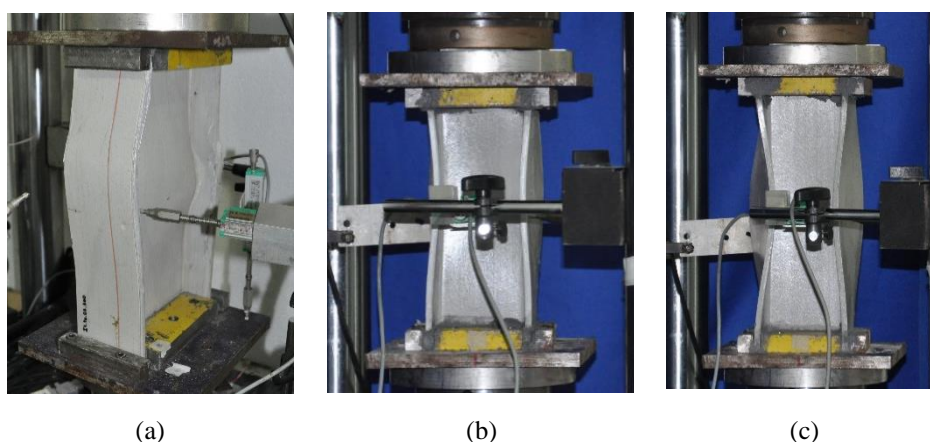


Figure 4.2 - Overviews of the shorter tested stubs: (a) Failure of I1.03.300 ($b_f/d=0.5$); (b) I2.ES.03.250 ($b_f/d=0.75$); (c) I3.ES.01.300 ($b_f/d=1.0$)

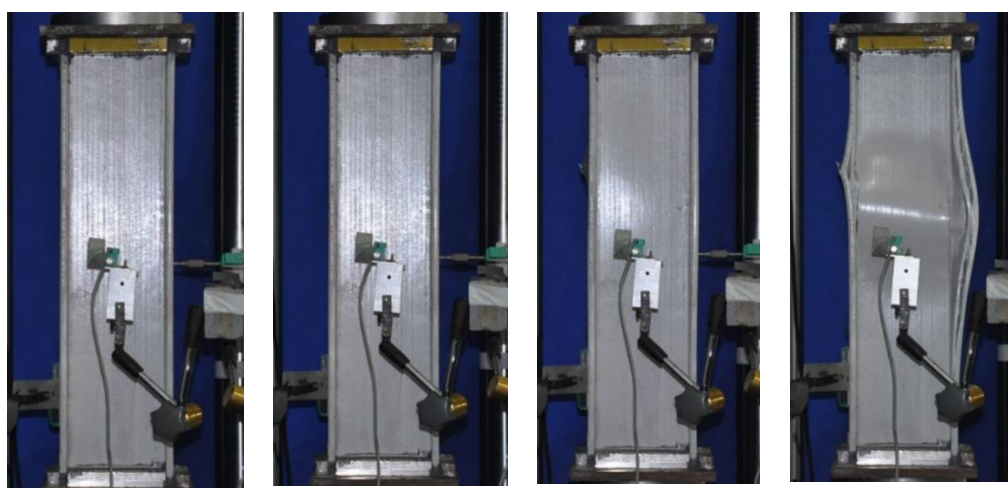


Figure 4.3 - Displacement growth of the tested stub I1.PO.06.600 ($b_f/d=0.5$)

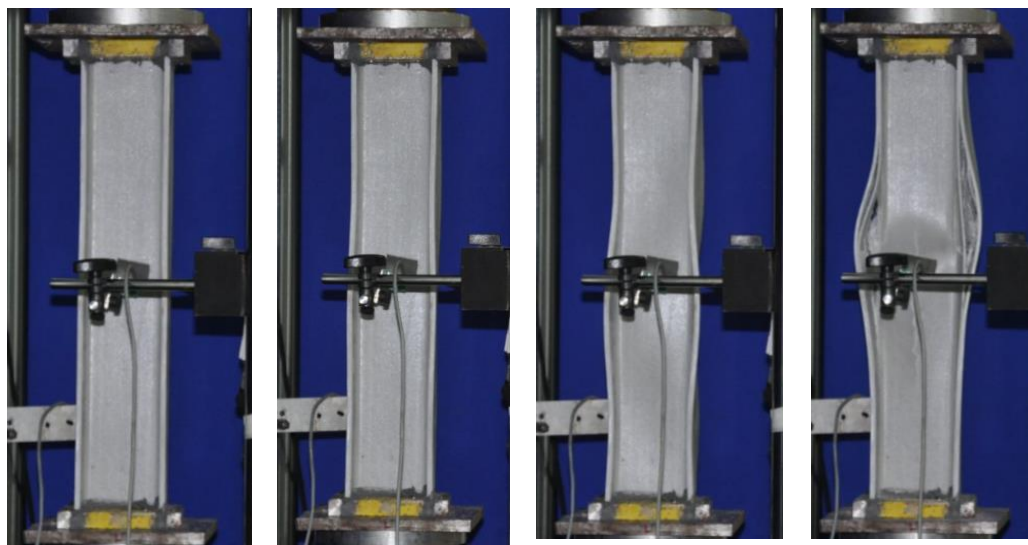


Figure 4.4 – Displacement growth of the tested stub I2.ES.06.550 ($bf/d=0.75$)

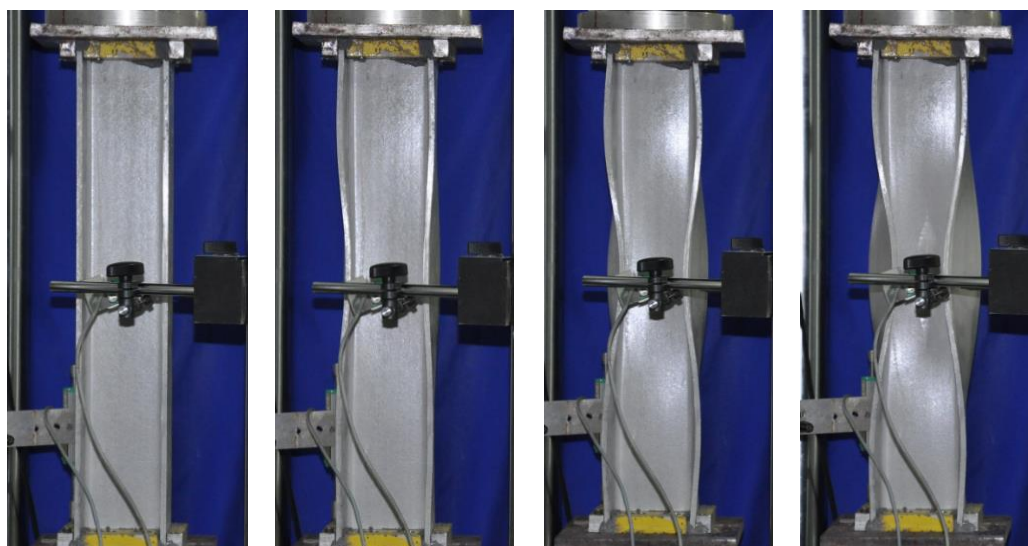
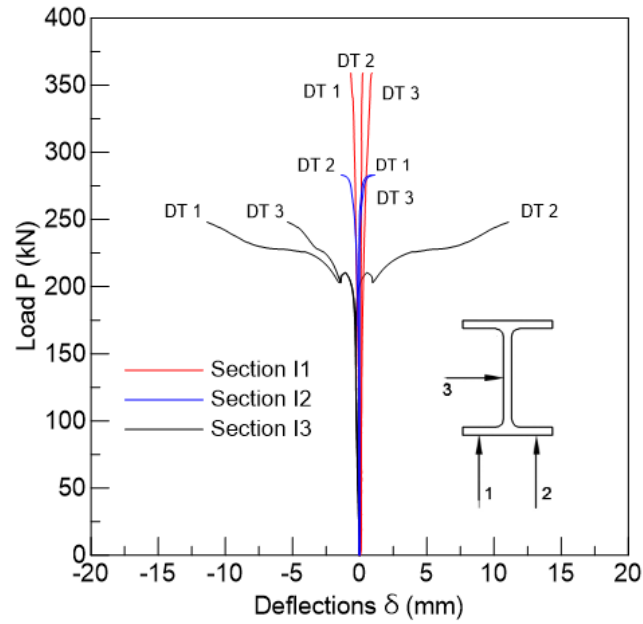


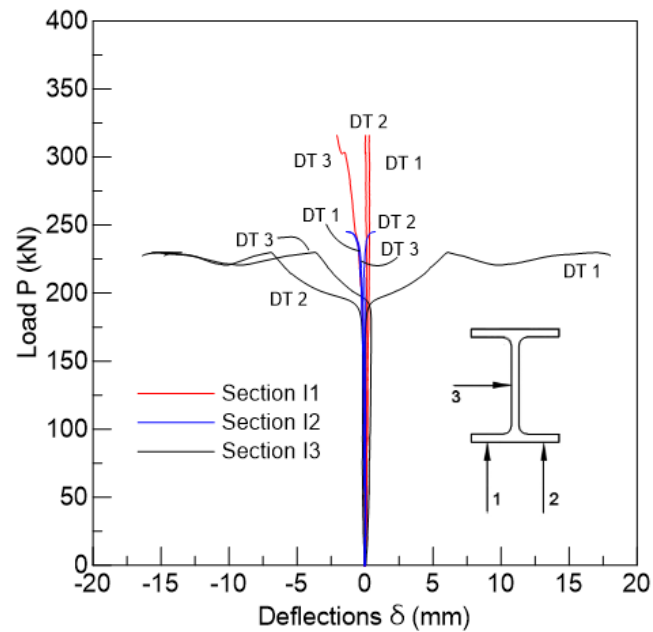
Figure 4.5 - Displacement growth of the tested stub I3.ES.06.550 ($bf/d=1.00$)

All stubs presented an ultimate failure occurred typically at the web-flange junctions and some along the centerline of the web, which are weaker regions of pGFRP wide flange columns (TURVEY and ZHANG, 2006).

Figure 4.6 a and b present the experimental curves for applied compression force, P , versus out-of-plane deflections, δ for shorter (250-300 mm) and longer (550-600 mm) columns with clamped plates. The graphs show a comparison of deflections measured with displacement transducers (DT) located at web and flange for representative studied sections.



(a) Shorter stubs



(b) Longer stubs

Figure 4.6 - P versus δ curves: (a) for shorter stubs: I1.PO.03.300, I2.ES.03.300, I3.ES.03.300; (b) for longer stubs: I1.PO.04.600, I2.ES.05.550, I3.ES.04.550

From Figure 4.6, it can be noted that shorter columns exhibited greater strengths and lower lateral deflections. The I_1 columns ($b_f/d=0.5$) experienced very little out of plane deflections and reached higher strengths, without exhibiting a clear post critical path. Extremely brittle failure was observed, which may be explained by an interaction between crushing and local buckling, explained in

section 2.6.2. In other words, the limit values for these individual modes are very close and, in the presence of geometric imperfections, an interaction occurs, leading to premature failure with no noticeable buckling.

The I_3 stubs ($b_f/d=1.0$), on the other hand, presented the largest displacements, a well-marked post critical behavior and a notable post-buckling reserve of strength. I_2 stubs ($b_f/d=0.75$) constituted an intermediate case, with little deflections and no pronounced post-critical path. Additionally, it is important to observe that the mechanical properties of the matrices have influence on the compressive strength of the columns, as previously mentioned. Profiles with vinyl ester resins (I_2 and I_3) presented greater compressive strengths when compared to the ones constituted of polyester resins (I_1). Therefore, this is consistent with the larger deflections observed for I_2 and I_3 profiles, once their critical loads are much lower than the material strength.

The comparisons between experimental critical loads obtained from Southwell plots and the theoretical predictions using GBTul are presented in Table 4.1 and plotted in Figure 4.7 in a signature curve format.

Table 4.1 - Ratio of theoretical predictions and experimental results

	<i>Stubs</i>	<i>Experimental Pcr (Pcr.exp)</i>	<i>Theoretical Pcr (Pcr. theo)</i>	<i>Pcr.exp/Pcr.theo</i>
<i>I₁ Section</i>	I ₁ .PO.01.300	386.61		0.81
	I ₁ .PO.02.300	399.95	476.40	0.84
	I ₁ .PO.03.300	486.11		1.02
	I ₁ .PO.04.600	369.47		0.93
	I ₁ .PO.05.600	374.39	395.30	0.95
	I ₁ .PO.06.600	411.42		1.04
<i>I₂ Section</i>	I ₂ .ES.01.250	271.00		1.04
	I ₂ .ES.02.250	264.40	261.00	1.01
	I ₂ .ES.03.250	271.05		1.04
	I ₂ .ES.04.550	239.22		1.09
	I ₂ .ES.05.550	254.68	218.95	1.16
	I ₂ .ES.06.550	258.57		1.18
<i>I₃ Section</i>	I ₃ .ES.01.300	213.27		1.01
	I ₃ .ES.02.300	222.74	210.20	1.01
	I ₃ .ES.03.300	227.56		1.08
	I ₃ .ES.04.550	195.78		1.10
	I ₃ .ES.05.550	204.58	178.30	1.15
	I ₃ .ES.06.550	202.22		1.13

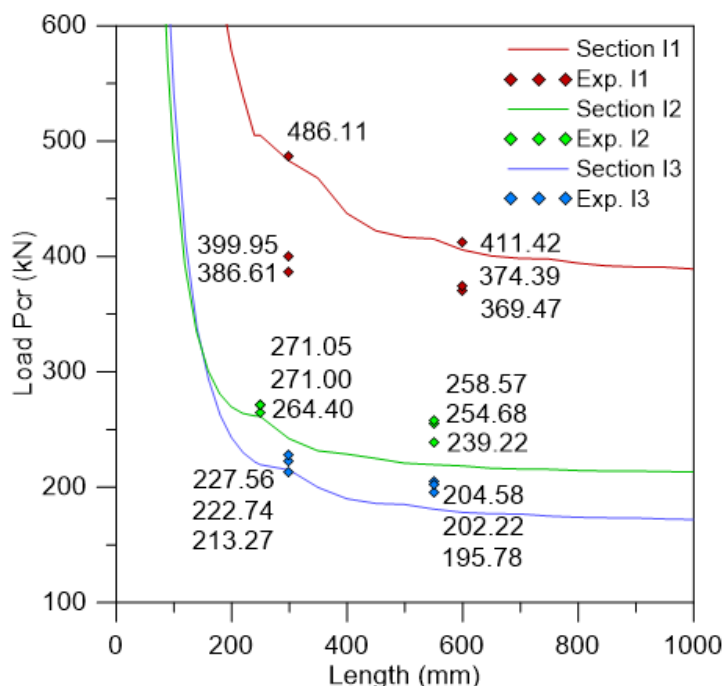


Figure 4.7 – Comparison between theoretical signature curve and experimental results

As can be observed, most of experimental critical loads of I_1 stubs were lower than theoretical ones, reaching a difference up to 19%. This difference has been observed in previous works (CARDOSO *et al.*, 2015) and may be explained by the small deflections captured by the transducers, which causes a lack of precision on Southwell plot. For I_2 and I_3 stubs, all results were greater than the theoretical prediction, being less than 4% for shorter I_2 stubs and less than 8% for shorter I_3 ones. The differences between theoretical and experimental values for longer columns were up to 18% and 15% for I_2 and I_3 stubs, respectively. The greater differences observed may be explained by the ‘stiffening’ effect provided by redistribution of stresses throughout cross-section, which seems to be more pronounced in longer columns. This effect was discussed by BARBERO and TROVILLION (1998), as previously mentioned.

This stiffening effect and the non-linear distribution of strains is clearly evident when analyzing the results of the stub column test instrumented with twelve strain gages. The photo sequence of this test is presented in Figure 4.8. As can be noted, the strain gages could not capture the maximum strains. This may be due to the fact that the chosen length is near the transition point of buckling modes with two and three wavelengths. However, according to TOMBLIN and BARBERO

(1994), “the critical load can be obtained regardless of the gauge position with respect to the wavelength”.

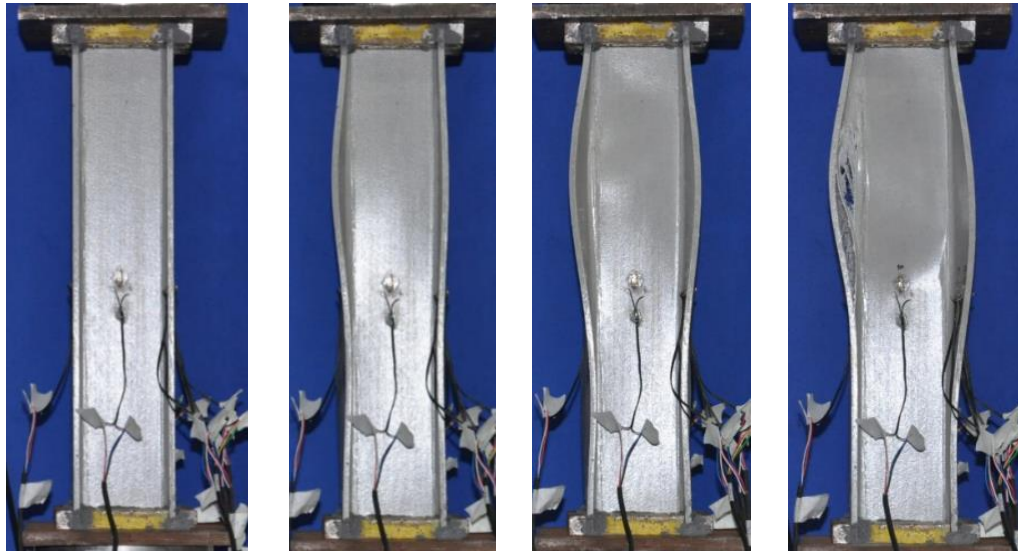


Figure 4.8 - Displacement growth of the tested stub I3.ES.07.495

Figure 4.9 presents the average strain captured by each pair of back-to-back strain gages positioned at the flange section – *i.e.* averages of strains measured for gages 1 and 12; 2 and 11; 4 and 7; 5 and 6 – and by the gage 3 positioned in the mid-point of the flange for each load level. As can be noted, a major redistribution of strains throughout the cross-section occurred for loads greater than 200 kN, (theoretical critical load is 186.98 kN). The strains for the gages located closer to flange tips presented a precipitous drop whereas the inner ones presented higher values, clearly showing the non-linear strain distribution that stiffens the system in the post-critical path.

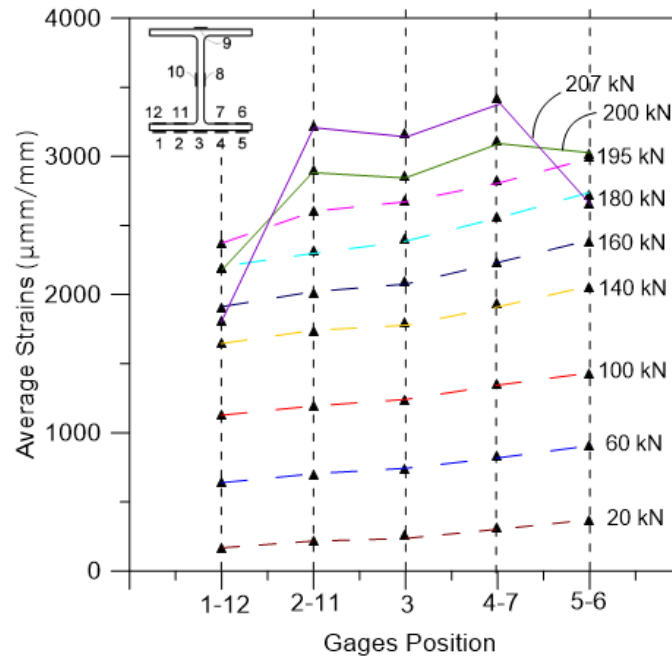


Figure 4.9 – Non-linear strain distribution across flange according to load level

Figure 4.10 shows a plot of the applied compressive force, P , versus curvature $1/r$ for each pair of strain gage. As can be observed, the stub presented a visible post-buckling reserve of strength and a decrease in curvature. This decrement may be explained by the fact that the strain gages ended up located very close to the inflection point, thus capturing little curvatures and being very sensitive to any change in the position of the inflection point during the test.

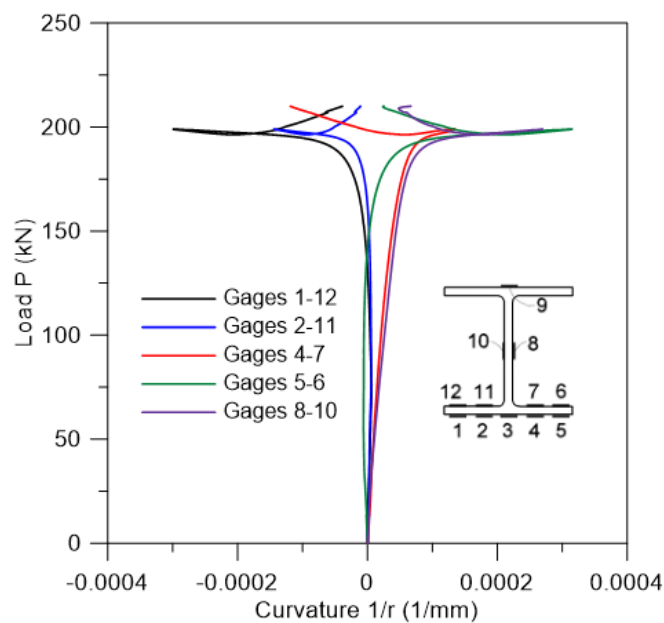


Figure 4.10 - Load P versus curvature $1/r$

The theoretical critical load predicted with the aid of GBTUL was 186.98 kN, whereas the experimental one obtained from Southwell plot shown in Figure 4.11 was 199.19 kN, leading to a difference of 6.5%. Therefore, it can be concluded that the ‘stiffening’ effect described results in apparently greater critical loads, although not very significant in this case.

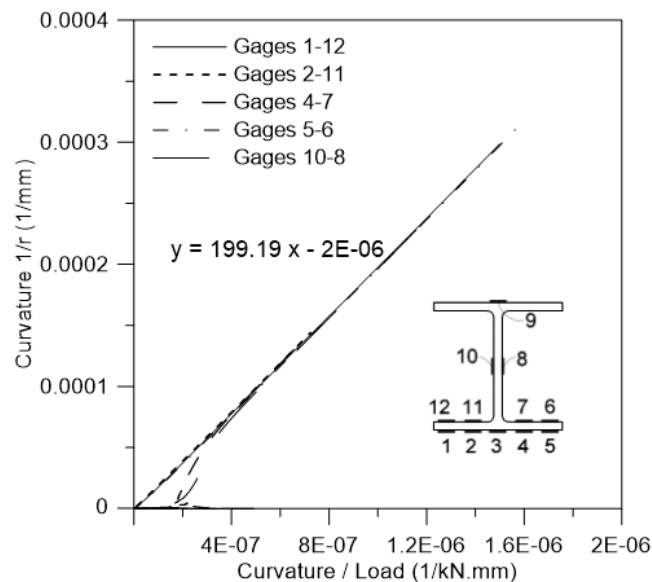


Figure 4.11 - Southwell Plot

4.3. Simply-supported Plates

Figures 4.12 and 4.13 present photo sequences of shorter (300-mm) and longer (550-mm) tested stubs. The number of half-waves formed for longer columns were in accordance with prediction. However, the shorter ones presented only a single half-wave, whereas two were expected. Only the stubs I_{3.02} and I_{3.03} were tested until failure, once the others slid off the roller after buckling.

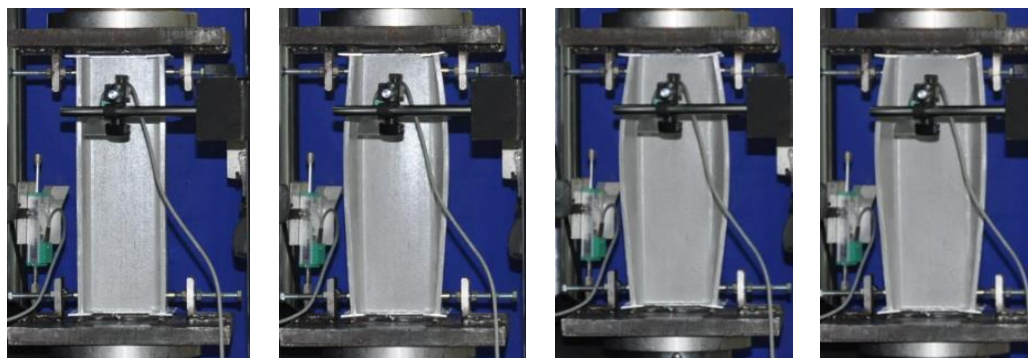


Figure 4.12 – Displacement growth of the tested stub I3.ES.01.300 ($bf/d=1.00$)

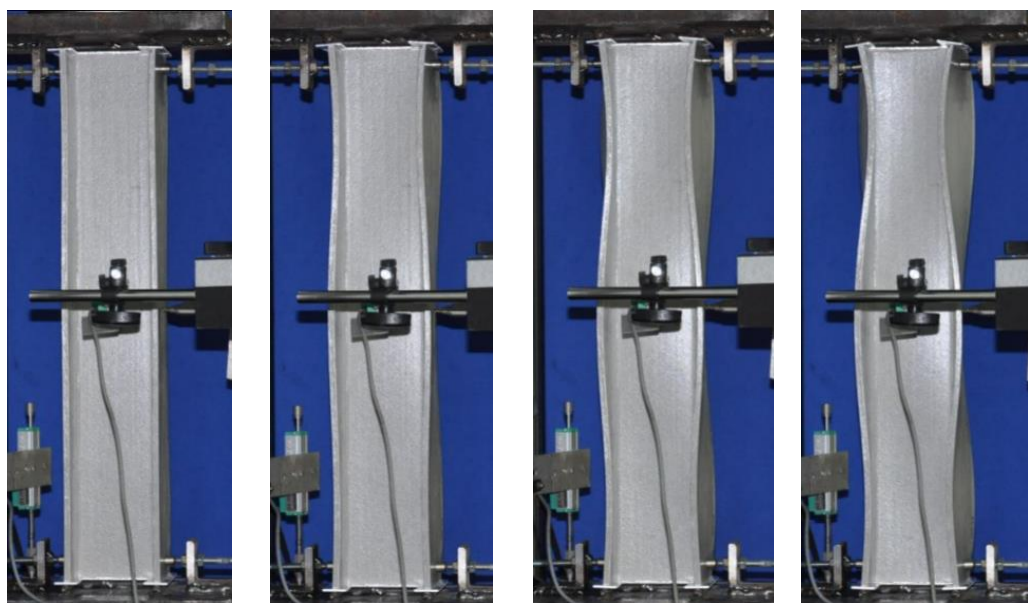


Figure 4.13 – Displacement growth of the tested stub I3.ES.05.550 ($bf/d=1.00$)

In an attempt to adopt the same test fixture to the other I-sections, four I_2 stubs were tested. However, they all exhibited end crushing associated with greater loading necessary for buckling, as shown in Figure 4.14. I_1 -section stubs were not tested because they would certainly experience a similar failure due to their narrower flange and much greater critical loads. This failure may be explained by a nonlinear stress distribution through thickness in the region in contact with the steel sheet, illustrated in Figure 4.15. A ticker plate could have softened this effect, but it would result in much greater torsional stiffness (GJ), affecting significantly the results. Therefore, simply supported end conditions were not considered for I_1 and I_2 profiles.



Figure 4.14 – End crushing of I_2 sections profiles

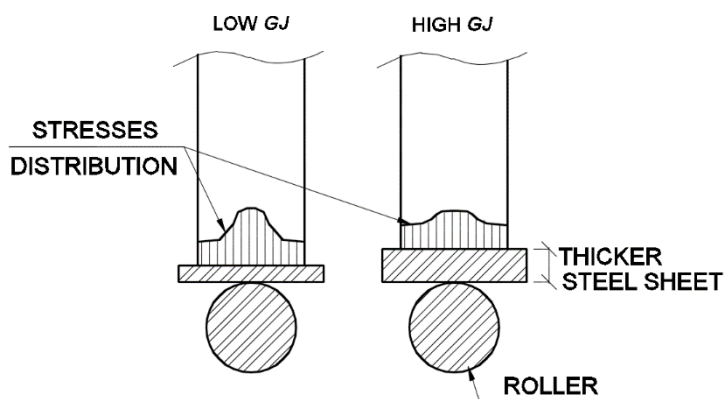


Figure 4.15 - Stresses distribution through the thickness in the loading region

Figure 4.16 presents representative experimental curves for applied compressive force, P , versus out-of-plane deflections, δ for shorter (300 mm) and longer (550 mm) columns.

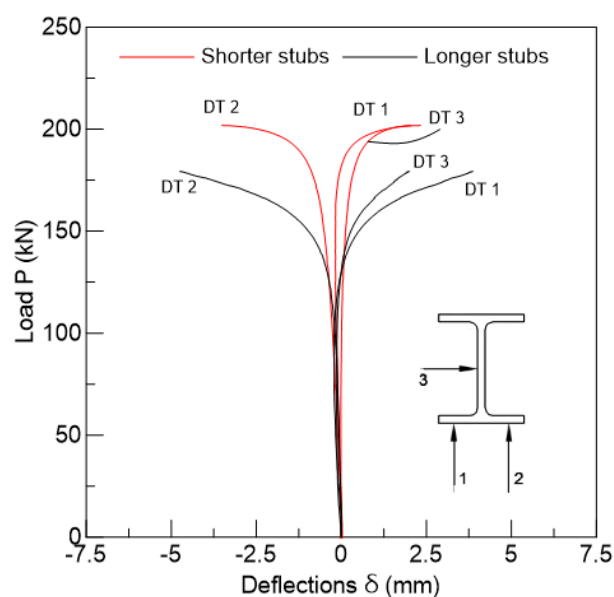


Figure 4.16 - P versus δ curves of shorter and longer stubs: I3.ES.02.300; I3.ES.05.550

As expected, the experimental critical loads obtained for shorter stubs were greater if compared with the longer ones. The comparisons between experimental results and theoretical predictions are presented in Table 4.2.

Table 4.2 - Ratio of experimental results and theoretical predictions

	<i>Stubs</i>	<i>Experimental</i>	<i>Theoretical</i>	<i>P_{cr.exp}/P_{cr.theo}</i>
		<i>P_{cr} (P_{cr.exp})</i>	<i>P_{cr} (P_{cr. theo})</i>	
<i>I₃ Section</i>	I ₃ .ES.01.300	191.78		1.11
	I ₃ .ES.02.300	202.07	172.02	1.17
	I ₃ .ES.03.300	202.56		1.18
	I ₃ .ES.04.550	180.81		1.07
	I ₃ .ES.05.550	171.63	168.51	1.02
	I ₃ .ES.06.550	181.50		1.08

As can be noted, all experimental results were greater than theoretical predictions, obtained using GBTul. The average differences registered were 15.3 % for shorter columns and 5.6 % for longer ones. The greater differences observed may be due to the torsional stiffness provided by the steel plate used in the test-fixture, which seems to be more pronounced in the shorter columns. Figure 4.17 shows the theoretical signature curve for stubs with simply supported plates, as well as the experimental critical loads.

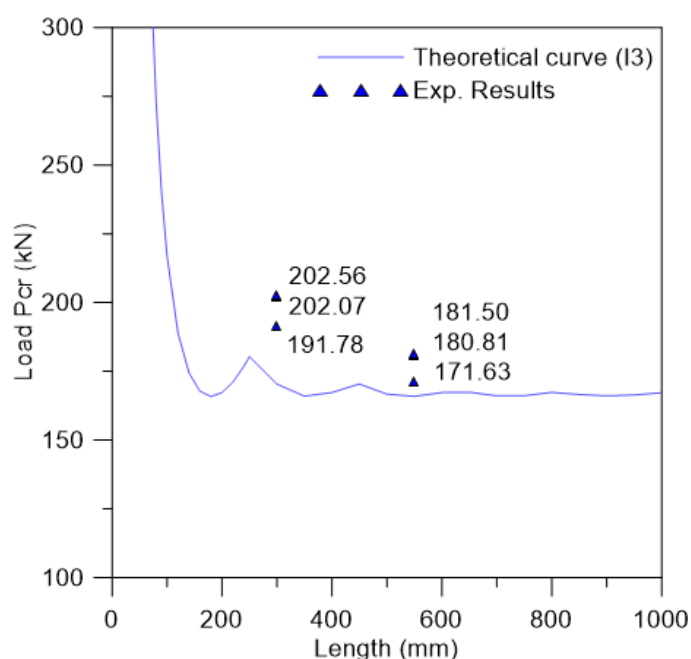


Figure 4.17 - Theoretical signature curve and experimental results

4.4. Simply in contact with base plate

The lateral deflections growth of shorter (300-mm) and longer (550-mm) columns are shown in Figure 4.18 and Figure 4.19. The shorter columns presented only a single half-wave, although two were expected, whereas the longer ones presented three half-waves, as predicted by GBTUL.

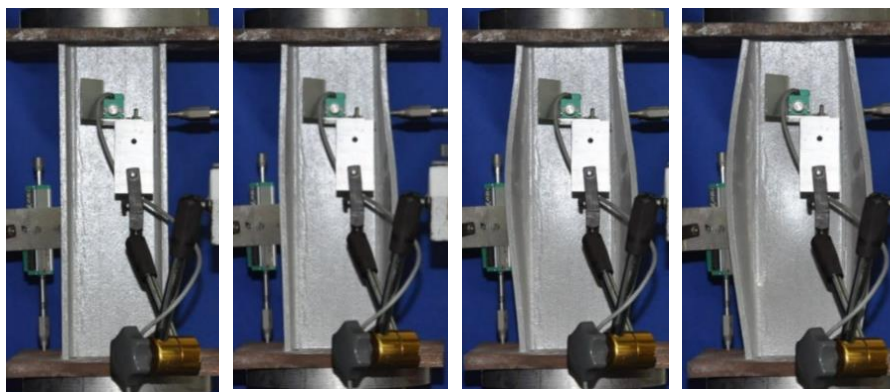


Figure 4.18 – Displacement growth of the tested stub I3.ES.01.300 ($bf/d=1.00$)

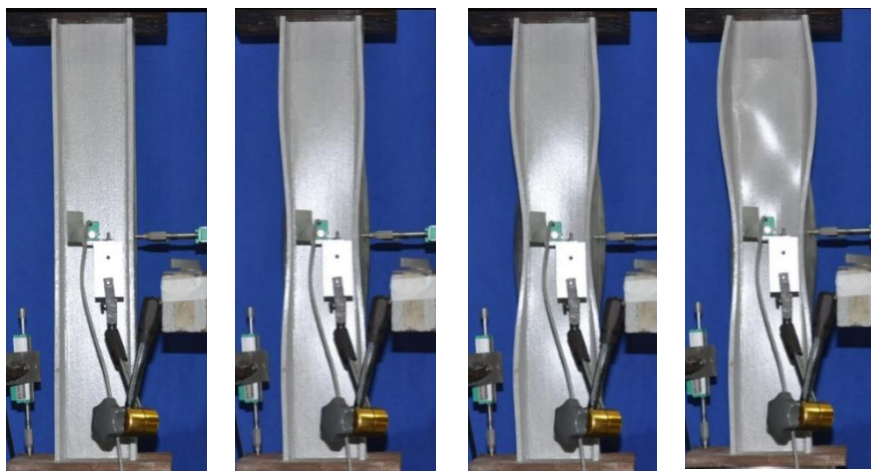


Figure 4.19 – Displacement growth of the tested stub I3.ES.04.550 ($bf/d=1.00$)

In these conducted tests, it was evident that the base plates restrained the rotation of the plates, as shown in Figure 4.20. It can be noted that there is a loss of contact between a part of the plate edge and the base plate of the machine. As previously mentioned, this leads to a shift in the reaction force that causes a restoring eccentricity that reduces the deflections, thus increasing the experimental critical loads, as observed by CARDOSO *et al.* (2015).

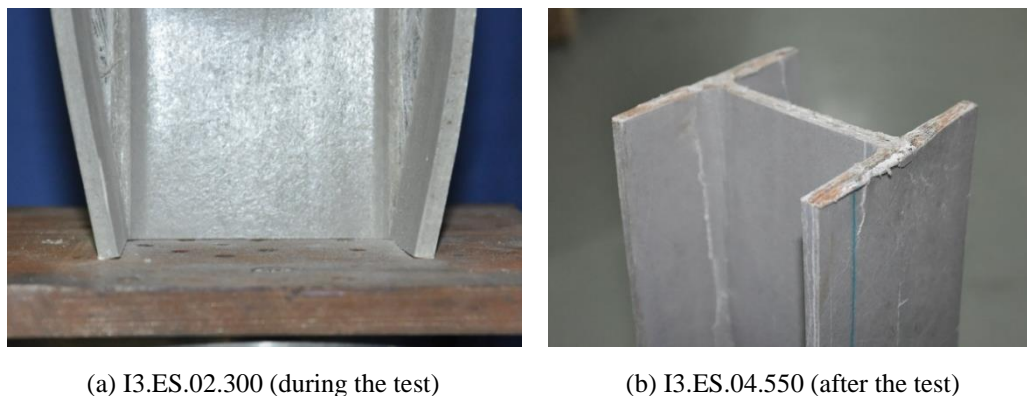


Figure 4.20 – End of an I3 stub tested on a direct contact condition

Four I_2 stubs were also tested in the same conditions, but it was not possible to achieve good results because the columns experienced premature failure by end crushing, as shown in Figure 4.21. This may be explained by the combination of non-linear stress distribution through thickness with the discontinuity of fibers that reduces locally the strength. In the same way, it was not possible to conduct this test on I_1 -sections stubs, once it would require greater loads to be applied during buckling test, being more susceptible to this effect.

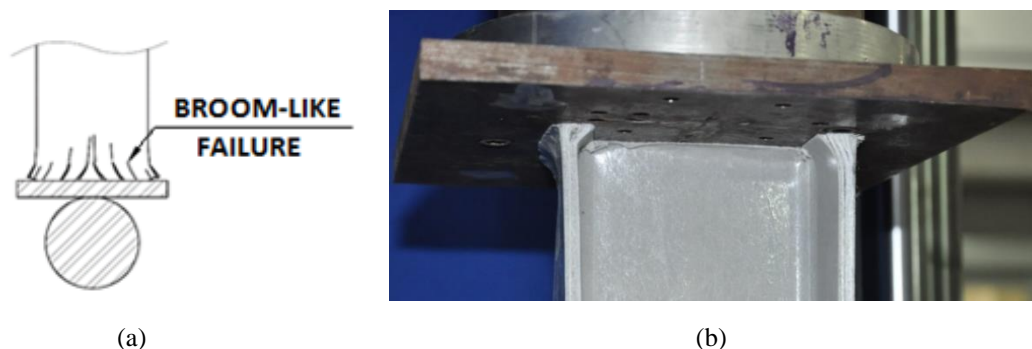


Figure 4.21 – End crushing of the tested stub I2.ES.06.550: (a) broom-like failure illustration; (b) stub wall's end

4.4.1. Comparison between the three boundary conditions

In order to compare the results presented in this section, Figure 4.22 presents the ratios between experimental and theoretical critical loads for columns having clamped and simply supported plates.

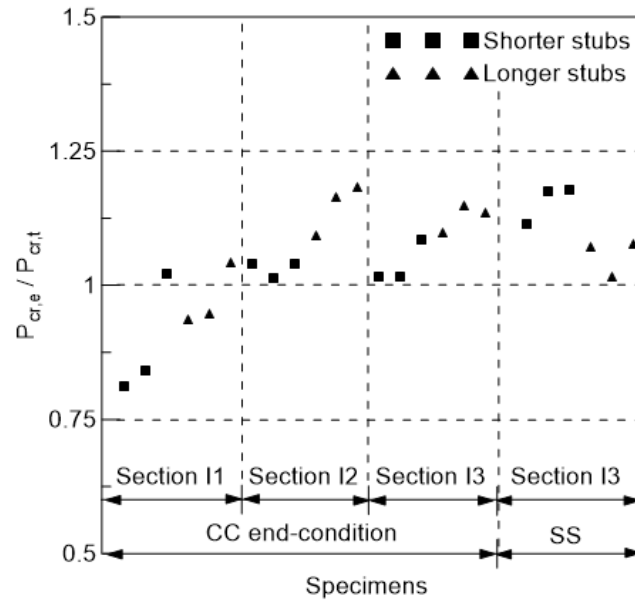
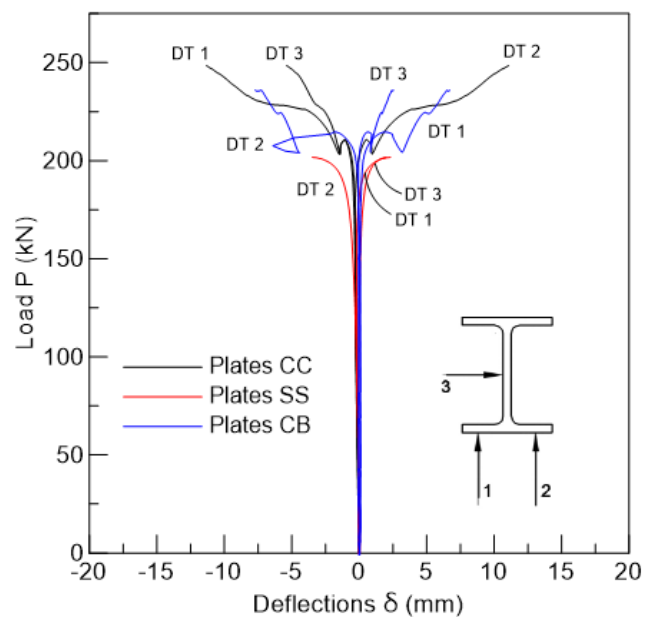
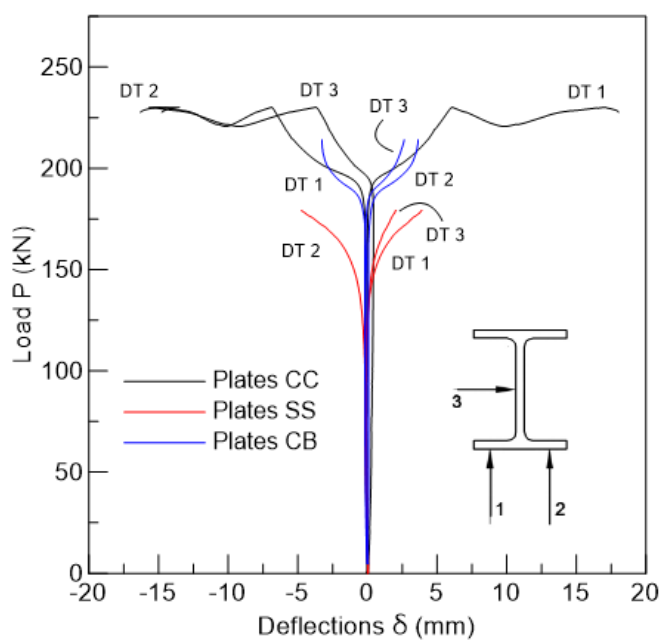


Figure 4.22 - Ratio of experimental results and theoretical predictions

Figure 4.23 presents the applied load P versus deflections δ plot for I_3 stubs ($b_t/d = 1.0$) with different boundary conditions: columns with clamped (CC) and simply supported (SS) plates, as well as the ones simply in contact with the base plates (CB). It can be noticed that the behavior of tested stubs directly supported on the base plates (CB) is in between those observed for columns with clamped (CC) and simply-supported plates, thus constituting an intermediate case both for shorter (300-mm) and longer (550-mm) columns. Table 4.3 presents the experimental critical loads obtained for I_3 stubs with plates simply in contact with base plates.



(a) Shorter stubs



(b) Longer stubs

Figure 4.23 - Load P versus deflections δ plots: (a) shorter stubs: I3.03 (CC), I3.02 (SS), I3.02 (CB); (b) longer stubs: I3.04 (CC), I3.05 (SS), I3.03 (CB)

Table 4.3 - Experimental critical load for CB columns

<i>Stubs</i>	<i>Experimental Pcr (Pcr.CB)</i>
<i>I₃.ES.01.300</i>	218.42
<i>I₃.ES.02.300</i>	215.67
<i>I₃.ES.03.550</i>	203.60
<i>I₃.ES.04.550</i>	191.58

Table 4.4 shows the ratio of the experimental critical loads for CB condition and the average experimental critical loads obtained for columns with CC and SS plates. Additionally, Table 4.5 presents the ratio of experimental results for CB columns and theoretical predictions for both clamped (CC) and simply-supported (SS) columns.

Table 4.4 - Ratio of experimental CB and CC/SS critical loads

<i>Stubs</i>	<i>Pcr.CC⁽¹⁾</i>	<i>Pcr.SS⁽²⁾</i>	<i>Pcr.CB/Pcr.CC</i>	<i>Pcr.CB/Pcr.SS</i>
Shorter	221.19	198.80	0.99	1.10
			0.98	1.16
Longer	200.86	177.98	0.92	1.14
			0.95	1.08

(1) Average experimental critical loads obtained for clamped stubs

(2) Average experimental critical loads obtained for simply-supported columns

Table 4.5 – Ratio of experimental CB and theoretical CC/SS critical loads

<i>Stubs</i>	<i>Pcr.CC.theo⁽¹⁾</i>	<i>Pcr.SS.theo⁽²⁾</i>	<i>Pcr.CB/ Pcr.CC.theo</i>	<i>Pcr.CB/ Pcr.SS.theo</i>
Shorter	210.20	172.02	1.04	1.27
			1.03	1.25
Longer	178.30	168.51	1.14	1.21
			1.07	1.14

(1) Theoretical critical loads predicted for clamped stubs

(2) Theoretical critical loads predicted for simply-supported columns

As mentioned previously, it can be observed from Tables 4.4 and 4.5 that the obtained experimental critical loads for plates directly supported on the base plate constitute an intermediary case between CC and SS columns. However, most results are apparently closer to those expected for columns with clamped plates. The differences between experimental results were lower than 2% for shorter CC

columns and up to 10% for shorter SS columns. For longer columns, these differences reached 8% for CC stubs and 14% for SS ones. Further, the ratio of experimental results of CB columns and theoretical predictions for CC columns were lower than 4% for shorter stubs and 14% for longer ones. On the other hand, differences of 27% were found for theoretical predictions of shorter SS columns and 21% for longer ones.

Figure 4.24 illustrates these comparisons, presenting the theoretical signature curves for clamped and simply supported columns, as well as the experimental results for the three studied boundary conditions. The experimental critical loads for CB columns are shown in the graph. It can be noted that all of them are above the theoretical curve for clamped plates, being farther from both theoretical SS curve and experimental loads obtained from SS stubs tested. It can be also concluded, from Figure 4.24 and from Tables 4.4 and 4.5, that the differences with respect to the simply-supported condition reduces with length, showing that the end-conditions lose their influence as number of half-waves increases.

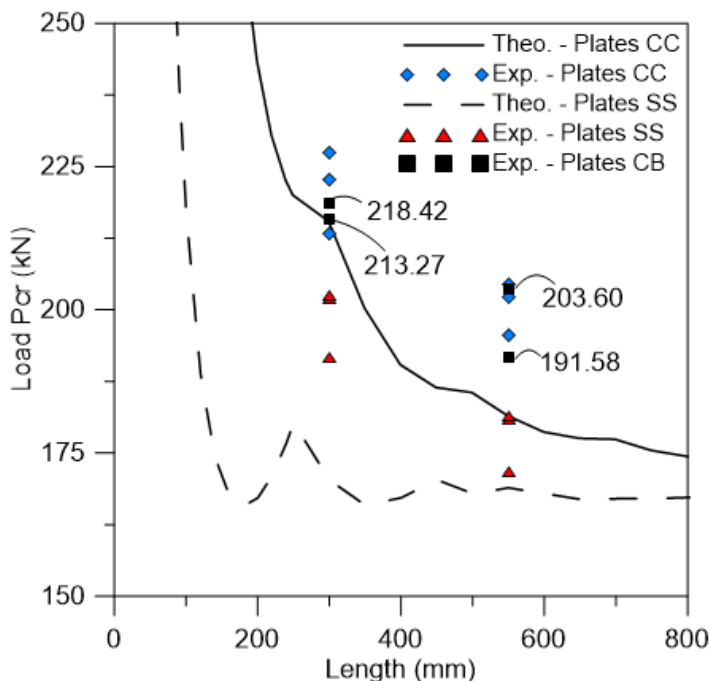
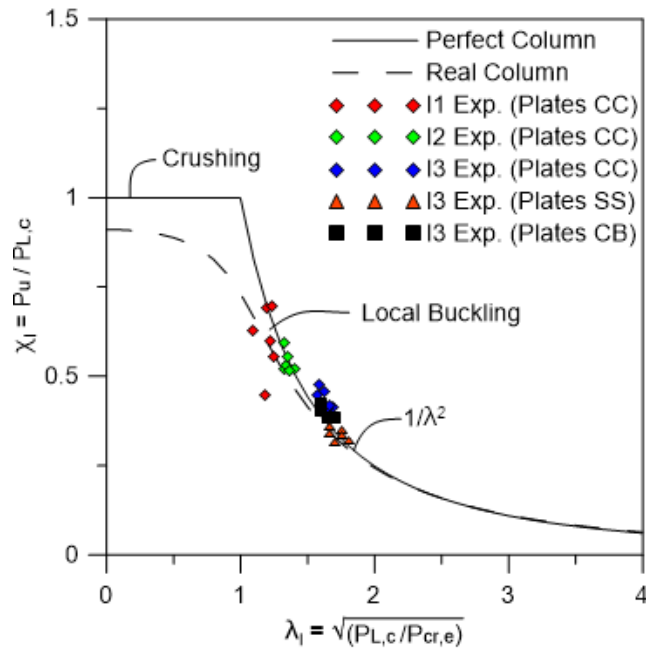


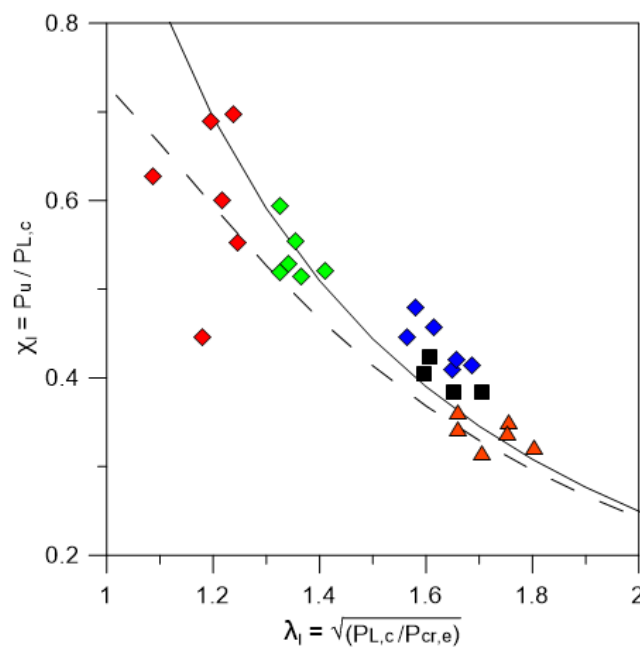
Figure 4.24 - Theoretical signature curves and experimental results for I_3 stubs

4.5. Strength curve and Slenderness map

Figure 4.25 shows a normalized compressive strength curve for GFRP columns. The experimental results for all analyzed twenty-eight stubs are plotted in the graph.



(a)



(b)

Figure 4.25 – (a) Strength curve; (b) zoom in the experimental points

It can be noted that I_1 stubs have their slenderness closer to $\lambda_l=1$, which marks a transition point between crushing and local buckling and, therefore, an interaction between these modes occur, in consistency with the described failure mode in section 4.2. The same conclusion can be taken analyzing the local *versus* global slenderness map shown in Figure 4.26. The combinations of slenderness studied in previous works are also plotted in the graph.

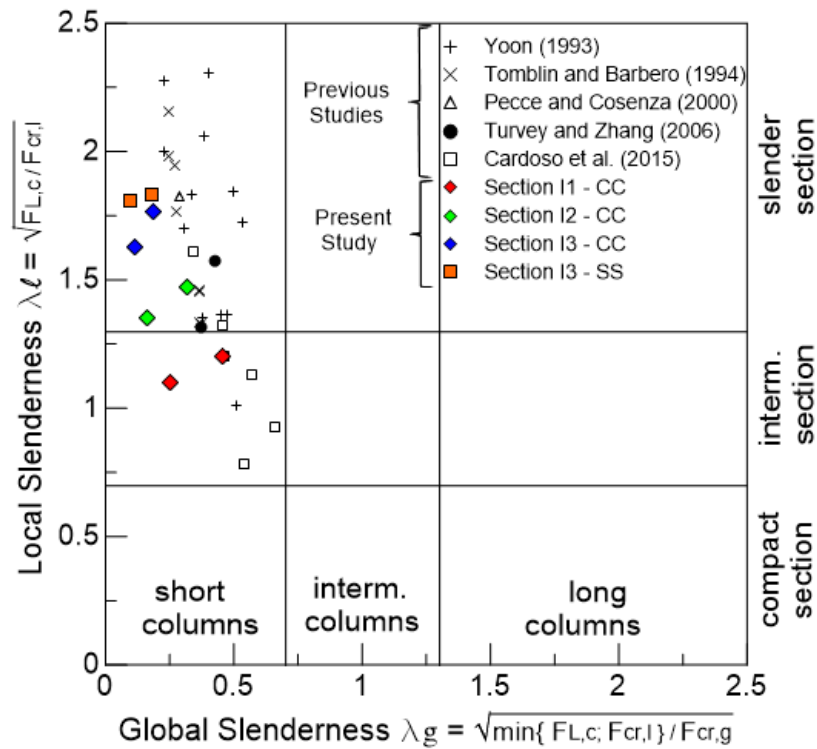


Figure 4.26 - local *versus* global slenderness map

On the other hand, both strength curve and slenderness map show that I_3 and I_2 sections are governed by local buckling failure for all boundary conditions, which is in agreement with the results observed in the experiments. It can also be noticed that experimental results are greater than the theoretical strength curve, being more evident for I_3 stubs with clamped plates. This may be explained by their pronounced post-critical reserve of strength, discussed in section 4.2. Therefore, the experimental results seem to be consistent, showing good agreement with theory.

4.6. Guidelines Recommendations

In order to fill in the lack of consensus concerning to GFRP local buckling tests, guideline recommendations are proposed for a reliable experimental investigation:

1. Determine the most relevant mechanical properties experimentally;
2. Consider the *columns* base restrained about minor and major axis, at both ends, decreasing the possibility of interaction between buckling modes. In order to have better controlled end-conditions and less possibility of end-crushing, clamped *plates* are recommended.
3. By using the signature curve, determine the ideal columns length;
4. The local buckling tests must be conducted in the range of short columns with slender sections, avoiding interaction with crushing and global buckling.
5. Instrument the columns with strain gages or displacements transducers on the point where maximum deflections are expected, in order to increase the accuracy of results. To accomplish this task, predict the number expected of half-waves with the aid of the signature curve;
6. Determine the experimental critical loads by using alternative methods that account the stiffening ‘effect’ due to the plates post-critical path (*e.g.* BARBERO and TROVILLON, 1998, SPENCER and WALKER, 1975).

5. Conclusions

5.1. Final Considerations

In this study, the performance and strength of pultruded GFRP stub columns subject to short term concentric loads were studied. A literature review was presented and parameters affecting local buckling experimental analysis were identified. An experimental program was conducted in order to investigate GFRP columns local buckling behavior, in which stubs with different flange width-to-section depth ratios (b_f/d), end-conditions and overall lengths were tested. The following conclusions are drawn from this study:

- a. the mechanical properties experimentally obtained through standard and non-standard tests were compared with theoretical predictions and the prediction by the Rule of Mixtures (ROM) showed to be closer to experimental data.
- b. the signature curve and the local *versus* global slenderness map were presented as important tools in order to conduct a successful buckling test, providing theoretical critical loads and expected failure modes. It is important to point out that the signature curve must be obtained using adequate materials properties and, in experimental programs, experimentally determined properties must be used.
- c. in agreement with theory, it was observed that members with greater local slenderness presented greater out-of-plane deflections and lower critical loads;
- d. the observed failure modes were all consistent with theoretical predictions;
- e. the test set-up for clamped plates worked well, with negligible rotation at the ends. Interaction between global and local buckling modes was observed in I_1 sections ($b_f/d=0.5$), which experienced very little

deflections followed by very sudden failure. On the other hand, the slender sections I_3 ($b_f/d=1.0$) presented notable post-buckling reserve of strength and greater deflections, resulting on a stiffening of the system that may explain the greater differences observed between experimental and theoretical critical loads. Further, the adopted method to determine the experimental critical loads (Southwell plot) is not perfectly linear, leading to a possible range of different results.

- f. Although the difficulties in reproducing simply-supported plates end-conditions, good results were achieved. The experimental critical loads obtained were closer from theoretical predictions when compared to the columns with the plates edges simply in contact with base plates. The set-up apparently worked well, allowing plates rotation, although a torsional stiffening provided by the steel plates might have resulted in higher experimental critical loads.

5.2. Future Works

In order to fill in the still existing gaps concerning to GFRP columns local buckling behavior, suggestions for future works are presented:

- Investigate the non-linear strains distributions throughout the cross section to augment available data on the understanding of the previously mentioned ‘stiffening effect’;
- Develop non-linear numerical analyzes and conduct an experimental program on columns with longer lengths;
- Determine the experimental critical loads by alternative methods proposed by SPENCER and WALKER (1975) and by BARBERO and TROVILLION (1998);
- Test the proposed set-up for simply supported plates on other sections geometry.

6. References

ACI Committee. “Guide for the design and construction of concrete reinforced with FRP bars.” American Concrete Institute, 2001.

Adams, Donald F., Carlsson, Leif A., & Pipes, R. Byron. “*Experimental characterization of advanced composite materials.*” CRC press, 2013.

American Edge (2017). Available at: <http://www.ameredge.com/technology.html>. Accessed in June, 15th, 2017.

ASCE. “Pre-Standard for Load and Resistance Factor Design (LRFD) of Pultruded Fiber Reinforced Polymer (FRP) Structures (Final)”. ASCE, Reston, VA, 2010

Ascione, L., Caron, J. F., Godonou, P., van IJselmuiden, K., Knippers, J., Mottram, T., ... & Tromp, L. *Prospect for new guidance in the design of FRP: Support to the implementation, harmonization and further development of the Eurocodes.* Publications Office of the European Union, 2016.

Associação Brasileira de Normas Técnicas NBR 15708: Indústrias do petróleo e gás natural – Perfis pultrudados. Parte 1: Materiais, métodos de ensaio e tolerâncias dimensionais. Rio de Janeiro, 2011.

ASTM Standard D3410/D3410M-16 (2016), “Compressive properties of polymer matrix composite materials with unsupported gage section by shear loading”, ASTM International, West Conshohocken, PA.

ASTM Standard D5379/D5379M-12 (2012), “Test method for shear properties of composite materials by the V-notched beam method”, ASTM International, West Conshohocken, PA.

ASTM Standard D6272-10 (2010), “Test method for flexural properties of unreinforced and reinforced plastics and electrical insulating materials by four-point bending”, ASTM International, West Conshohocken, PA.

ASTM Standard D6641/D6641M-16 (2016), “Determining the compressive properties of polymer matrix composite laminates using a combined loading compression (CLC) test fixture”, ASTM International, West Conshohocken, PA.

ASTM Standard D695-15 (2015), “Compressive properties of rigid plastics”, ASTM International, West Conshohocken, PA.

ASTM Standard D790-15 (2015), “Test methods for flexural properties of unreinforced and reinforced plastics and electrical insulating materials”, ASTM International, West Conshohocken, PA.

Bakis, C. E., Bank, L. C., Brown, V., Cosenza, E., Davalos, J. F., Lesko, J. J., ... & Triantafillou, T. C. “Fiber-reinforced polymer composites for construction—State-of-the-art review.” *Journal of composites for construction*, 6.2 (2002): 73-87.

Bank, Lawrence C. “Progressive failure and ductility of FRP composites for construction.” *Journal of Composites for Construction* 17.3 (2013): 406-419.

Bank, Lawrence C. “Shear properties of pultruded glass FRP materials.” *Journal of Materials in Civil Engineering* 2.2 (1990): 118-122.

Bank, Lawrence C. *Composites for construction: structural design with FRP materials*. John Wiley & Sons, 2006.

Bank, Lawrence C., T. Russell Gentry, & Aaron Barkatt. Accelerated test methods to determine the long-term behavior of FRP composite structures: environmental effects. *Journal of Reinforced Plastics and Composites* 14.6 (1995): 559-587.

Barbero, Ever J. *Introduction to composite materials design*. CRC press, 2010.

Barbero, Ever J., & Trovillion, J. “Prediction and measurement of the post-critical behavior of fiber-reinforced composite columns.” *Composites science and technology* 58.8 (1998): 1335-1341.

Barbero, E. J., & DeVivo, L. "Beam-column design equations for wide-flange pultruded structural shapes." *Journal of Composites for Construction* 3.4 (1999): 185-191.

Barbero, Ever, & Tomblin, J. "Euler buckling of thin-walled composite columns." *Thin-walled structures* 17.4 (1993): 237-258.

Barbero, E. J. & Raftoyiannis, I. G., "Buckling analysis of pultruded composite columns." In *Impact and Buckling of Structures*, ed. D. Hui & I. Elishakoff, ASME, AD-Vol. 20, AMD-Vol. 114, 1990,47-52.

Bazant, Z. P., & Cedolin, L. "*Stability of structures: elastic, inelastic, fracture and damage theories.*" *World Scientific, Sigapore* (2010).

Bazant, Z. P. "Shear buckling of sandwich, fiber composite and lattice columns, bearings, and helical springs: Paradox resolved." *Transactions-American Society of Mechanical Engineers Journal of Applied Mechanics* 70.1 (2003): 75-83.

Bennett, Evan A. *Influence of creep on the stability of pultruded E-glass/polyester composite columns at elevated service temperatures*. Diss. Georgia Institute of Technology, 2005.

Cardoso, Daniel C.T., Harries, Kent A. & Batista, E. M. "Compressive strength equation for GFRP square tube columns." *Composites Part B: Engineering* 59 (2014): 1-11.

Cardoso, D. *Compressive strength of pultruded glass-fiber reinforced polymer (GFRP) columns*. Diss. Thesis. Rio de Janeiro: Universidade Federal do Rio de Janeiro, 2014.

Cardoso, Daniel C. T., Harries, Kent A. & Batista, E. M. "Compressive local buckling of pultruded GFRP I-sections: development and numerical/experimental evaluation of an explicit equation." *Journal of Composites for Construction* 19.2 (2015): 04014042.

Clarke, J. L. "EUROCOMP design code and handbook: Structural design of polymer composites." *E & FN Spon, London* (1996).

CNR, National Research Council of Italy, "CNR-DT-205/2007 - Guide for the design and construction of structures made of thin FRP pultruded elements." Rome, 2008.

Cogumelo (2017). Available at: http://www.cogumelo.com.br/images/linha-industrial/downloads/Catalogo_Geral_Produtos.pdf. Accessed in June 16th, 2017.

Correia, J. R., Bai, Y., & Keller, T. "A review of the fire behaviour of pultruded GFRP structural profiles for civil engineering applications." *Composite Structures* 127 (2015): 267-287.

Davalos, J. F., Salim, H. A., Qiao, P., Lopez-Anido, R., & Barbero, E. J. "Analysis and design of pultruded FRP shapes under bending." *Composites Part B: Engineering* 27.3-4 (1996): 295-305.

Di Tommaso, A., & Russo, S. "Shape influence in buckling of GFRP pultruded columns." *Mechanics of composite materials* 39.4 (2003): 329-340.

Engesser, F., 1889, "Die Knickfestigkeit gerader Stäbe," Zentralblatt des Bauverwaltungs., 11, p. 483–486

ESDEP (2017). Available at: <http://fgg-web.fgg.uni-lj.si/~pmoze/esdep/master/toc.htm>, Accessed at July, 22th, 2017.

Fiberline Composites (2017). Available at: <https://fiberline.com/pontresina-bridge>. Accessed in June, 15th, 2017.

Fiberline Composites (2017a). Available at: <https://fiberline.com/fiberline-bridge>. Accessed in June, 15th, 2017.

Gray, E. F., Browne, H. C., Burkhardt, W., Fowler, T. J., Lizzio, A., & McDermott, J. F. I. "Structural plastics design manual." *Manuals and Reports on Engineering Practice, American Society of Civil Engineers* 63 (1984).

Hashin, Z., & Rosen, B. W. "The elastic moduli of fiber-reinforced materials." *Journal of applied mechanics* 31.2 (1965): 223-232.

HBM Operating Manual (2005). Available at: www.rcmt.cvut.cz/soubor/f-at/70d22ce0.../4/catman_pro-software-manual-eng.pdf. Accessed in July, 28th, 2017.

Hermans, J. J. "Elastic Properties of Fiber Reinforced Materials When Fibers Are Aligned." *Koninklijke Nederlandse Akademie Van Wetenschappen-Proceedings Series B-Physical Sciences* 70.1 (1967): 1.

Hill, R1. "A self-consistent mechanics of composite materials." *Journal of the Mechanics and Physics of Solids* 13.4 (1965): 213-222.

Hull, Derek, & T. W. Clyne. *An introduction to composite materials*. Cambridge university press, 1996.

Instron (2017). Available at: <http://www.instron.us/en-us/testing-solutions/by-test-type/flexure/astm-d6272>. Accessed in June, 16th, 2017.

ISO (International Organization for Standardization). ISO 1172: Textile-glass reinforced plastics – Prepregs, moulding compounds and laminates – Determination of the textile-glass and mineral-filler content – Calcination methods. Geneva, Switzerland, 1996.

ISO (International Organization for Standardization). ISO 14125: Fiber-reinforced plastic composites – Determination of flexural properties. Geneva, Switzerland, 1998.

J. M. Whitney, *Elastic Moduli of Unidirectional Composites with Anisotropic Filaments*

Jones, Robert M. "Mechanics of Composite Materials. Taylor and Francis." *Inc., Philadelphia, PA* (1999).

Kang, Jin Ook. "Fiber-reinforced polymeric pultruded members subjected to sustained loads." (2002): 2842-2842.

Keller, T., Theodorou, N. A., Vassilopoulos, A. P., & De Castro, J. "Effect of Natural Weathering on Durability of Pultruded Glass Fiber-Reinforced Bridge and

Building Structures." *Journal of Composites for Construction* 20.1 (2015): 04015025.

Keller, Thomas. "Influences of advanced composite materials on structural concepts for bridges and buildings." *The 3rd International Conference on Composites in Infrastructure ICCI'02, San Francisco, USA*. No. CCLAB-CONF-2002-003. 2002.

Landesmann, A., Seruti, C. and Batista, E. M. "Mechanical Properties of Glass Fiber Reinforced Polymers Members for Structural Applications." *Materials Research* 18.6 (2015): 1372-1383.

Lau, Saijod TW, M. R. Said, and Yaakob, M. Y. "On the effect of geometrical designs and failure modes in composite axial crushing: A literature review." *Composite Structures* 94.3 (2012): 803-812.

Leissa, Arthur W. *Buckling of laminated composite plates and shell panels*. No. OSURF-762513/713464. Ohio State Univ Research Foundation Columbus, 1985.

Lekhnitskii, S. G. (1968). *Anisotropic plates* (No. FTD-HT-23-608-67). Foreign Technology Div Wright-Patterson Afb Oh.

Li, Z., and Benjamin W. Schafer. "Buckling analysis of cold-formed steel members with general boundary conditions using CUFSM conventional and constrained finite strip methods." (2010).

Mallick, P. K., ed. *Composites engineering handbook*. CRC Press, 1997.

Mallick, P. K. *Fiber-reinforced composites: materials, manufacturing, and design*. CRC press, 2007.

McCarthy, M. J., & L. C. Bank. "Sensitivity studies on local flange buckling equations for pultruded beams and columns." *Advances in FRP Composites in Civil Engineering*. Springer, Berlin, Heidelberg, 2011. 115-118.

Mottram, J. T. "Determination of critical load for flange buckling in concentrically loaded pultruded columns." *Composites Part B: Engineering* 35.1 (2004): 35-47.

Naughton, B. P., F. Panhuizen, & A. C. Vermeulen. "The elastic properties of chopped strand mat and woven roving in gr laminae." *Journal of reinforced plastics and composites* 4.2 (1985): 195-204.

Nielsen, L. E., & Chen, P. E. (1968). Young's modulus of composites filled with randomly oriented fibers. *Journal Materials*.

Pecce, M., and Cosenza, E. "Local buckling curves for the design of FRP profiles." *Thin-walled structures* 37.3 (2000): 207-222.

Pindera, M. J., P. Ifju, & D. Post. "Iosipescu shear characterization of polymeric and metal matrix composites." *Experimental Mechanics* 30.1 (1989): 101-108.

Puente, I., A. Insausti, & M. Azkune. "Buckling of GFRP columns: An empirical approach to design." *Journal of Composites for Construction* 10.6 (2006): 529-537.

Pultrusão do Brasil (2017). Available at: <http://www.pultrusao.com.br>. Accessed in June, 16th, 2017.

Pultrusions, Creative. "The Pultex Pultrusion Design Manual of Standard and Custom Fiber Reinforced Polymer Structural Profiles", vol.5. Alum Bank, PA (2017).

Reis, A., and Camotim, D. *Estabilidade estrutural*. 2001. (In Portuguese).

Riley, M. B., and J. M. Whitney. "Elastic properties of fiber reinforced composite materials." *Aiaa Journal* 4.9 (1966): 1537-1542.

Schardt, R. "Generalized beam theory - an adequate method for coupled stability problems." *Thin-Walled Structures* 19.2-4 (1994): 161-180.

Seangatith, Sittichai, and Weerapun Sriboonlue. "Axially Loaded Glass-Fiber Reinforced Plastic Composite Columns." *Proc. 7th East Asia-Pacific Conf. on Structural Engineering & Construction, Kochi, Japan*. Vol. 2. 1999.

Seruti, C. A. *Caracterização mecânica e desempenho estrutural de Elementos Pultrudados*. Diss M.Sc., COPPE – Universidade Federal do Rio de Janeiro, Rio de Janeiro, Brasil, 2013. (In Portuguese).

Sonti, S. S., and E. J. Barbero. "Material characterization of pultruded laminates and shapes." *Journal of reinforced plastics and composites* 15.7 (1996): 701-717.

Southwell, Richard V. "On the analysis of experimental observations in problems of elastic stability." *Proceedings of the Royal Society of London A: Mathematical, Physical and Engineering Sciences*. Vol. 135. No. 828. The Royal Society, 1932.

Souza Almeida, S. P. *Avaliação das propriedades mecânicas de compósitos pultrudados de matriz polimérica com reforço de fibra de vidro*. Diss. Tese de Doutorado, Universidade Federal do Rio de Janeiro, Brasil, 2004. (In Portuguese).

Spencer, H. H., and A. C. Walker. "Critique of Southwell plots with proposals for alternative methods." *Experimental Mechanics* 15.8 (1975): 303-310.

Strongwell (2017). Available at: <http://www.strongwell.com/wp-content/uploads/2013/04/Custom-Pultrusions-Brochure.pdf>. Accessed in June 16th, 2017.

Strongwell (2017a). Available at: http://www.sdplastics.com/strongwell_new.html. Accessed in July, 28th, 2017.

Timoshenko, S. P., and Gere, J. M. "Theory of elastic stability. 1961." *McGrawHill-Kogakusha Ltd, Tokyo* (1961): 9-16.

Togashi, Bárbara S. *Desempenho e Resistência à Compressão de Cantoeiras Pultrudadas Curtas de Polímero Reforçado com Fibra de Vidro (PRFV)*. Diss. PUC-Rio, 2017. (In Portuguese).

Tomblin, J., & Barbero, E.. "Local buckling experiments on FRP columns." *Thin-Walled Structures* 18.2 (1994): 97-116.

Turvey, G. J. "Torsion tests on pultruded GRP sheet." *Composites science and technology* 58.8 (1998): 1343-1351.

Turvey, G. J., and Zhang, Y. "A computational and experimental analysis of the buckling, postbuckling and initial failure of pultruded GRP columns." *Computers & structures* 84.22 (2006): 1527-1537.

Yoon, S. J. *Local buckling of pultruded I-shape columns*. Diss. Georgia Institute of Technology, 1993.

Ziemian, Ronald D., ed. *Guide to stability design criteria for metal structures*. John Wiley & Sons, 2010.

Zureick, A., and Scott, D. "Short-term behavior and design of fiber-reinforced polymeric slender members under axial compression." *Journal of Composites for Construction* 1.4 (1997): 140-149.

Zureick, A., and Steffen, R. "Behavior and design of concentrically loaded pultruded angle struts." *Journal of structural engineering* 126.3 (2000): 406-416.

7. Appendix A – Column Tests Reports

7.1. Clamped Plates

I1.PO.01.300



Date: January/2017

P_{cr} : 386.61 kN

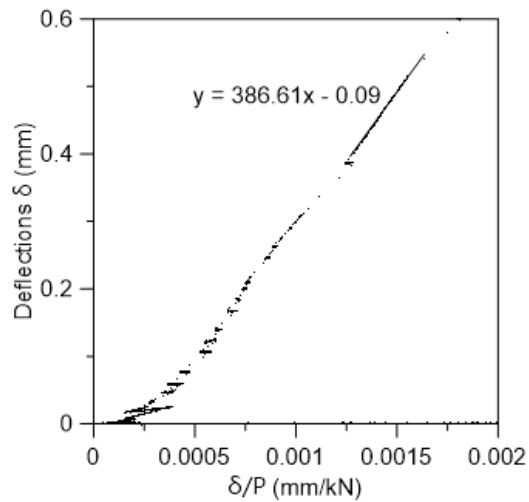
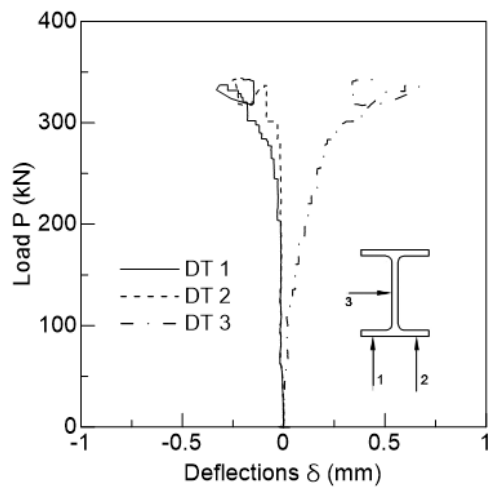
P_u : 343.67 kN

Visual observations:

No local or global

buckling observed

Failure: Crushing at web-
flange junctions



I1.PO.02.300



Date: January/2017

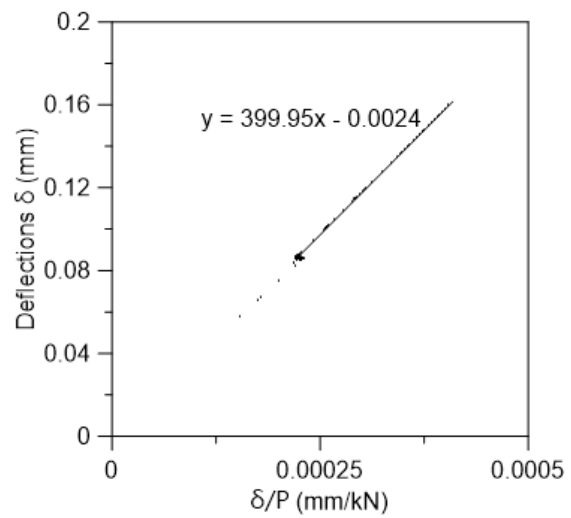
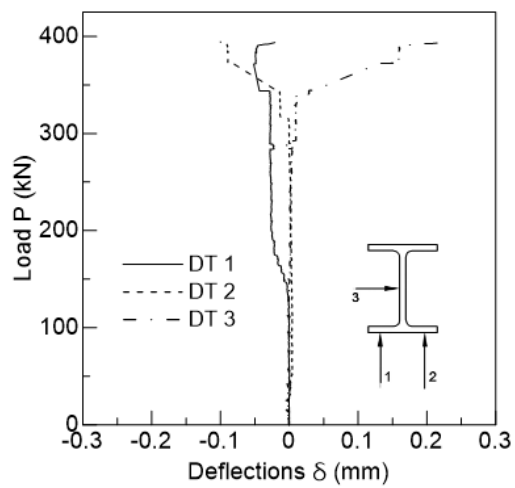
P_{cr} : 399.95 kN

P_u : 394.27 kN

Visual observations:

No local or global buckling
observed

Failure: Crushing at web-
flange junctions



I1.PO.03.300



Date: January/2017

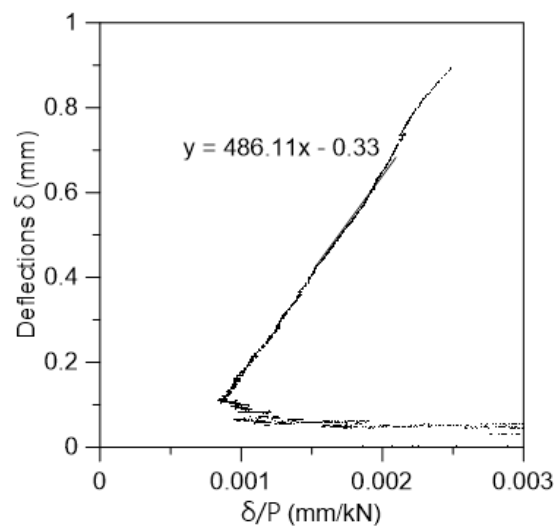
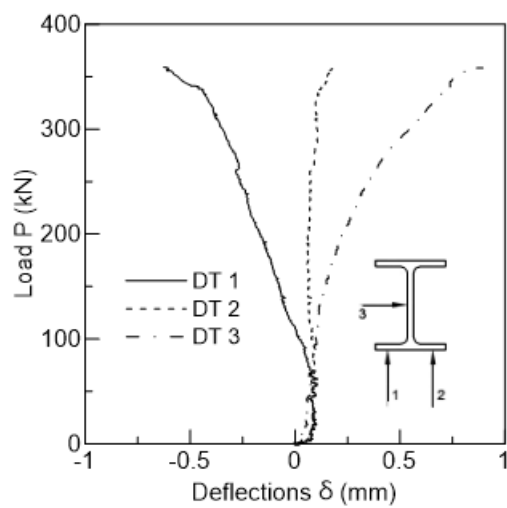
P_{cr} : 486.11 kN

P_u : 358.95 kN

Visual observations:

No local or global buckling
observed

Failure: Crushing at web-
flange junctions



I1.PO.04.600



Date: January/2017

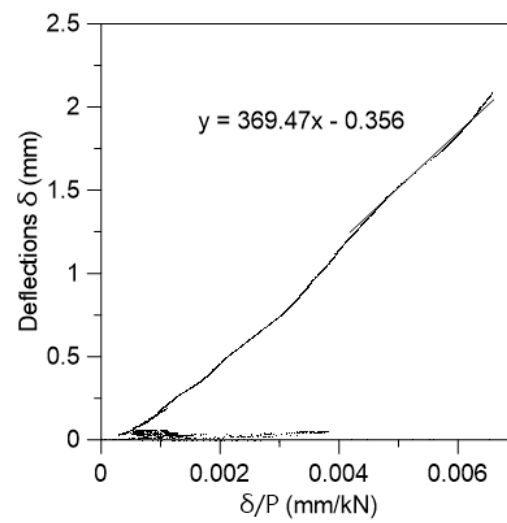
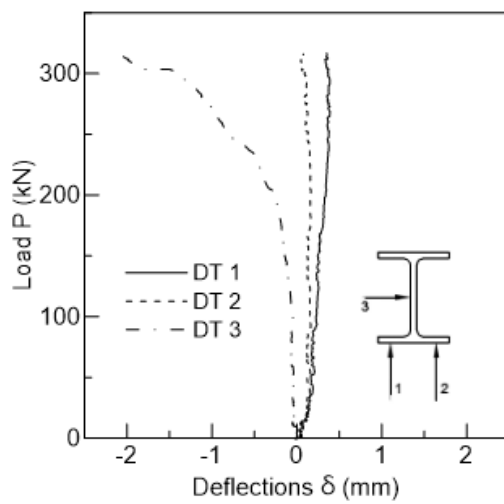
P_{cr} : 369.47 kN

P_u : 316.43 kN

Visual observations:

No local or global buckling
observed

Failure: Crushing at web-flange
junctions



I1.PO.05.600



Date: January/2017

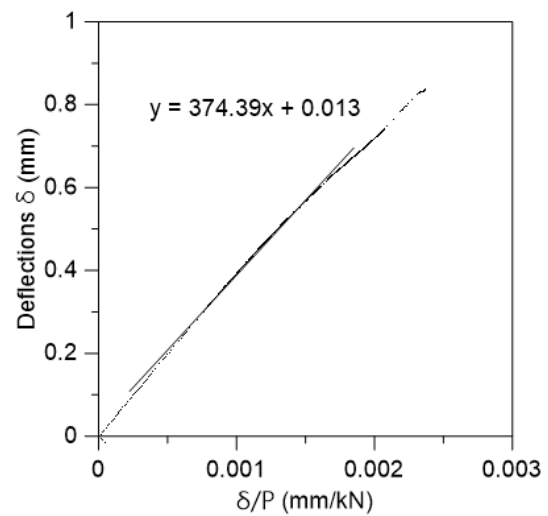
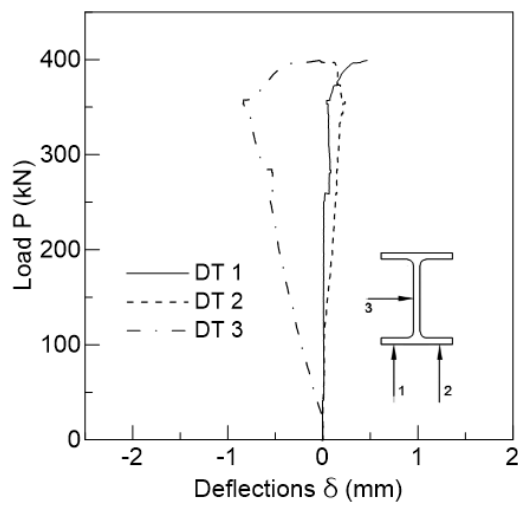
P_{cr} : 374.39 kN

P_u : 399.57 kN

Visual observations:

No local or global
buckling observed

Failure: Crushing at web-
flange junctions



I1.PO.06.600



Date: January/2017

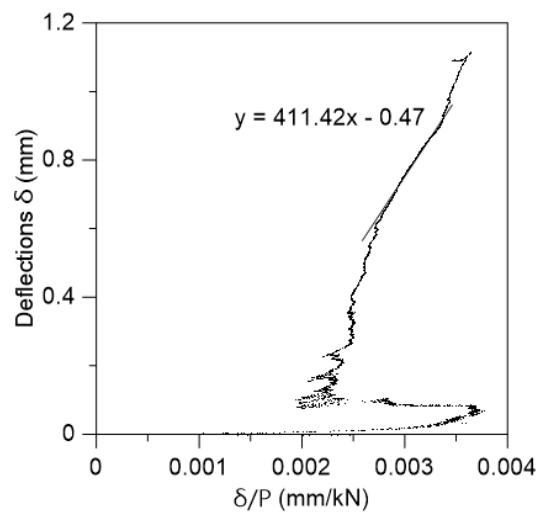
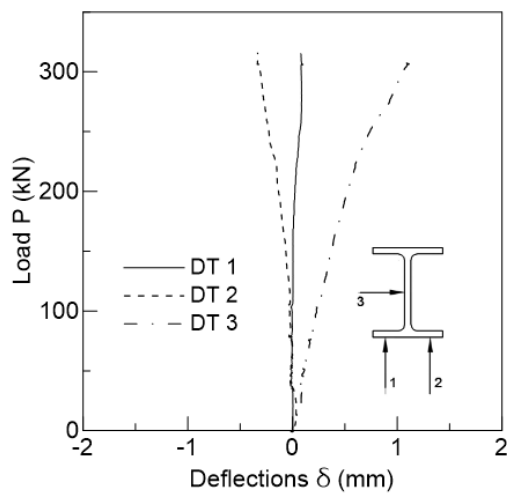
P_{cr} : 411.42 kN

P_u : 315.25 kN

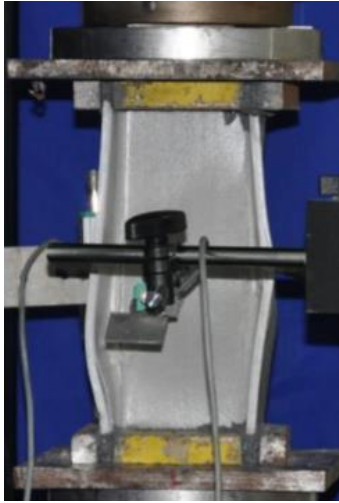
Visual observations:

Local buckling observed

Failure: Crushing at web-flange
junctions



I2.ES.01.250



Date: January/2017

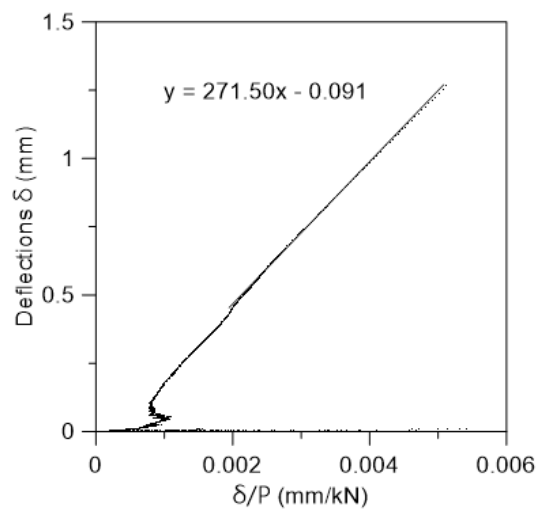
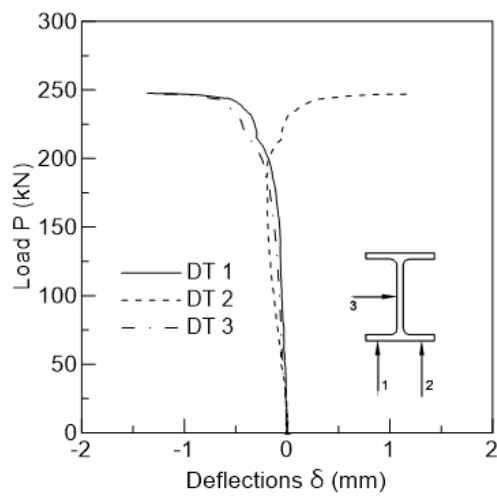
P_{cr} : 271.50 kN

P_u : 247.46 kN

Visual observations:

Local buckling observed

Failure: Crushing at web-flange
junctions



I2.ES.02.250



Date: January/2017

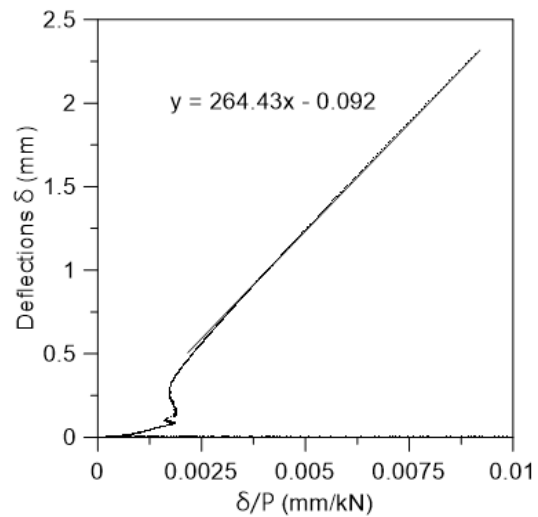
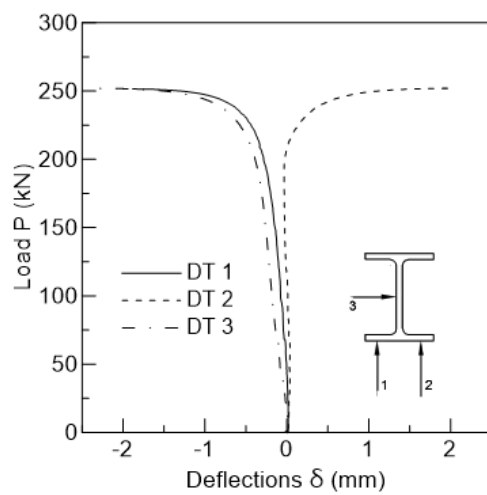
P_{cr} : 264.43 kN

P_u : 251.80 kN

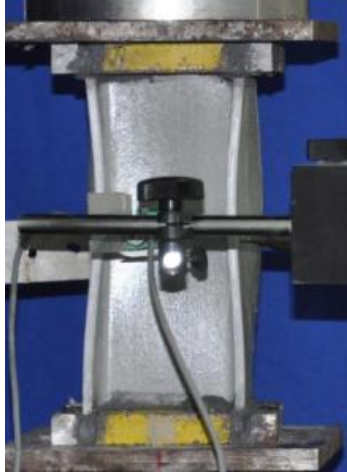
Visual observations:

Local buckling observed

Failure: Crushing at web-flange junctions and at the centerline of the web



I2.ES.03.250



Date: January/2017

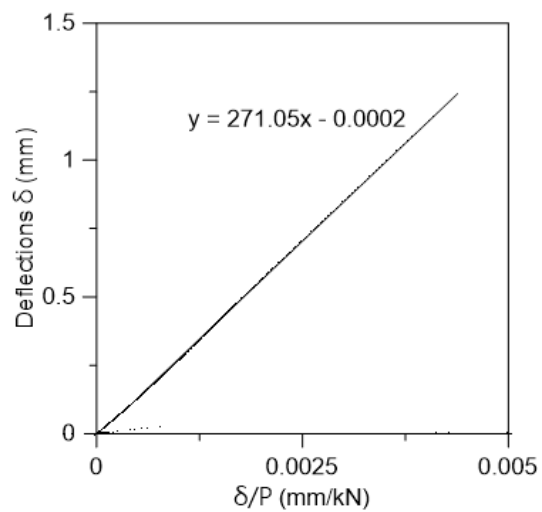
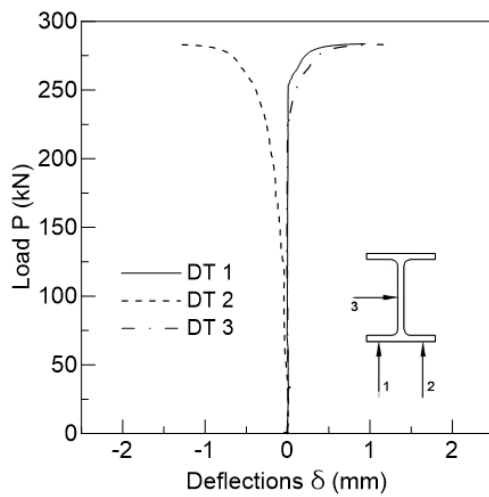
P_{cr} : 271.05 kN

P_u : 283.19 kN

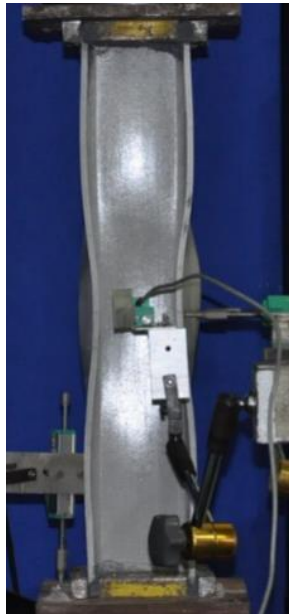
Visual observations:

Local buckling observed

Failure: Crushing at web-flange
junctions



I2.ES.04.550



Date: January/2017

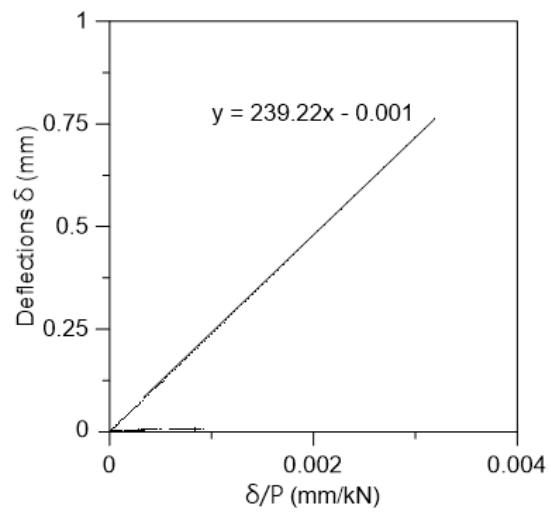
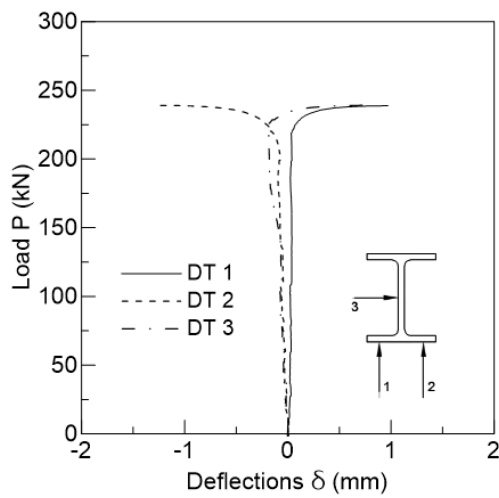
P_{cr} : 239.22 kN

P_u : 239.04 kN

Visual observations:

Local buckling observed

Failure: Crushing at web-flange
junctions



I2.ES.05.550

Date: January/2017

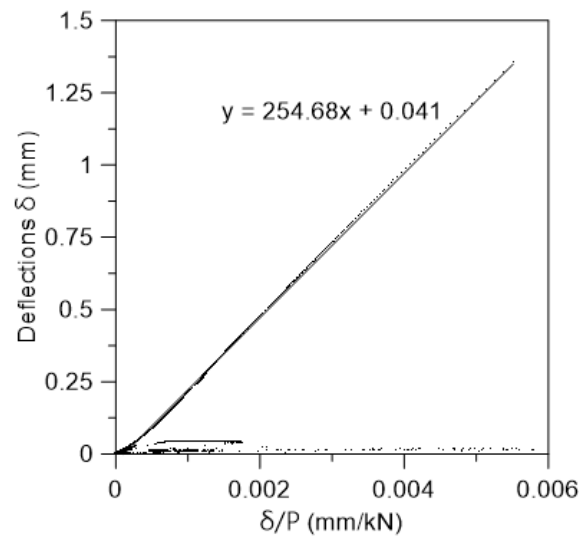
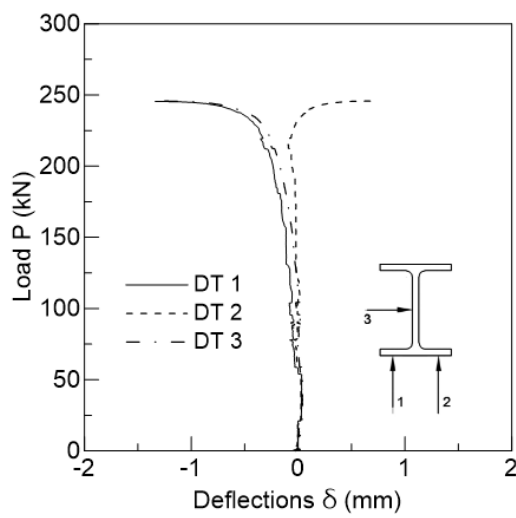
P_{cr} : 254.68 kN

P_u : 245.32 kN

Visual observations:

Local buckling observed

Failure: Crushing at web-flange
junctions



I2.ES.06.550

Date: January/2017

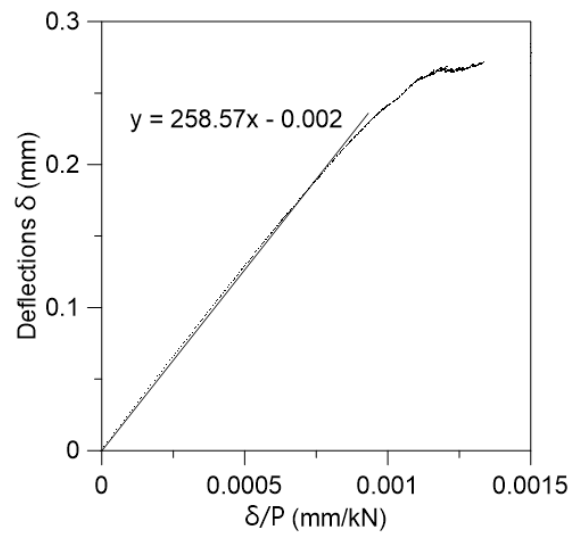
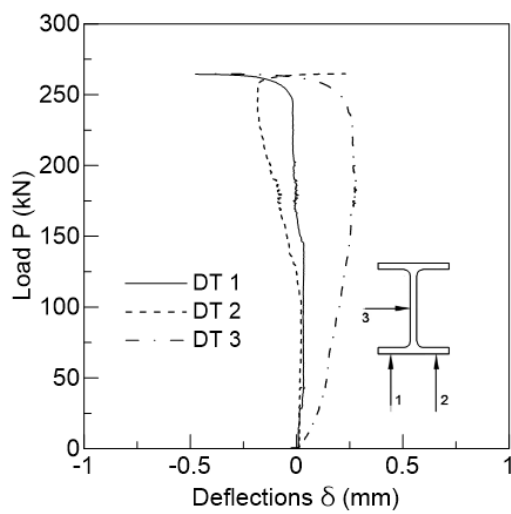
P_{cr} : 258.57 kN

P_u : 264.29 kN

Visual observations:

Local buckling observed

Failure: Crushing at web-flange
junctions



I3.ES.01.300



Date: January/2017

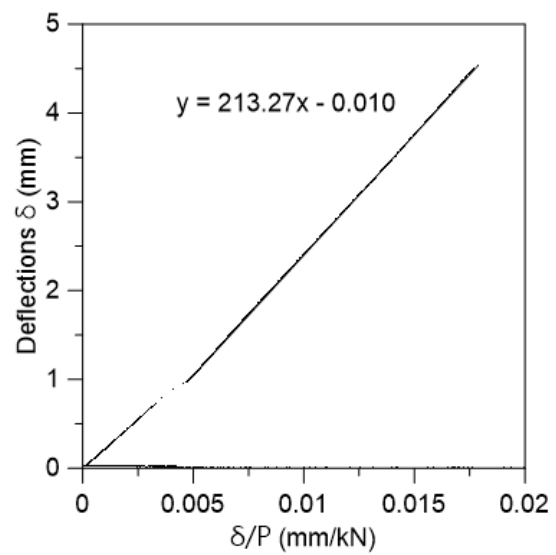
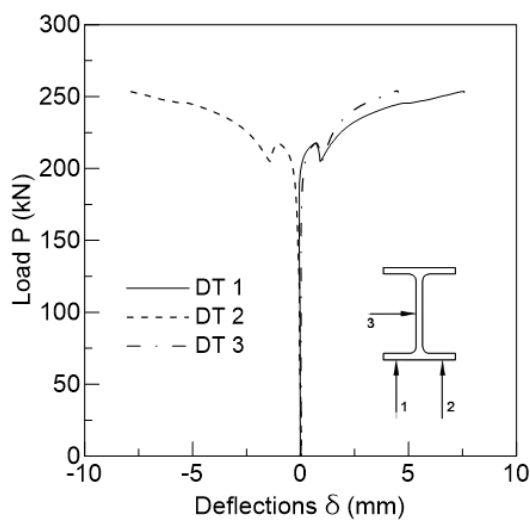
P_{cr} : 213.27 kN

P_u : 253.61 kN

Visual observations:

Local buckling observed

Failure: Crushing at web-flange
junctions



I3.ES.02.300



Date: February/2017

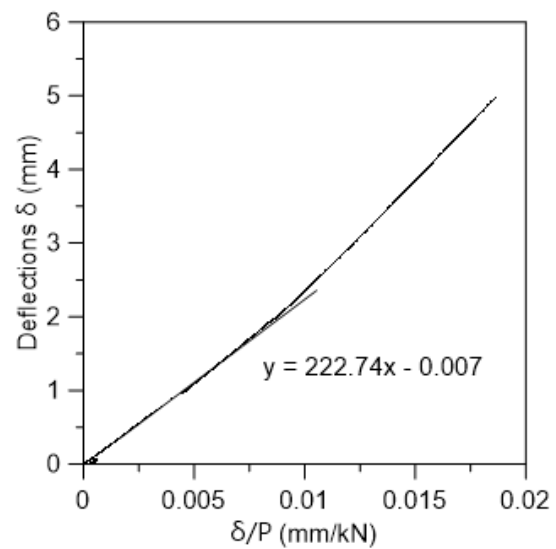
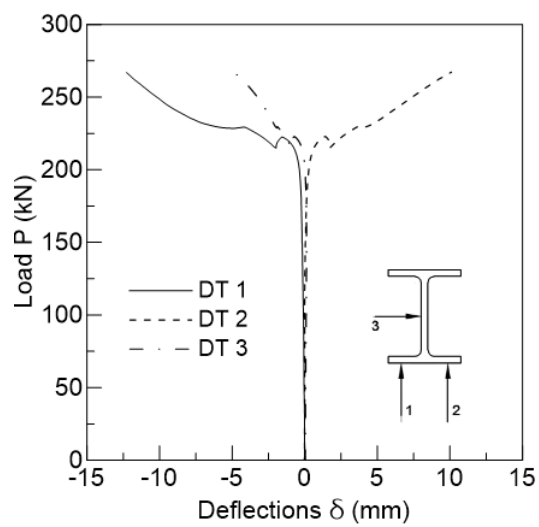
P_{cr} : 222.74 kN

P_u : 266.86 kN

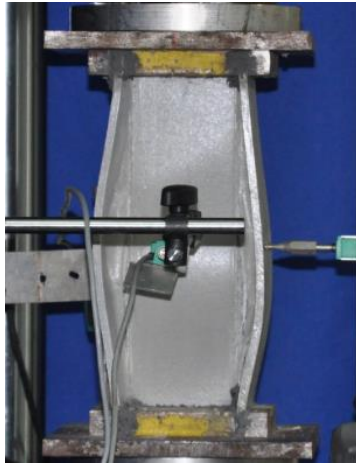
Visual observations:

Local buckling observed

Failure: Crushing at web-flange
junctions



I3.ES.03.300



Date: February/2017

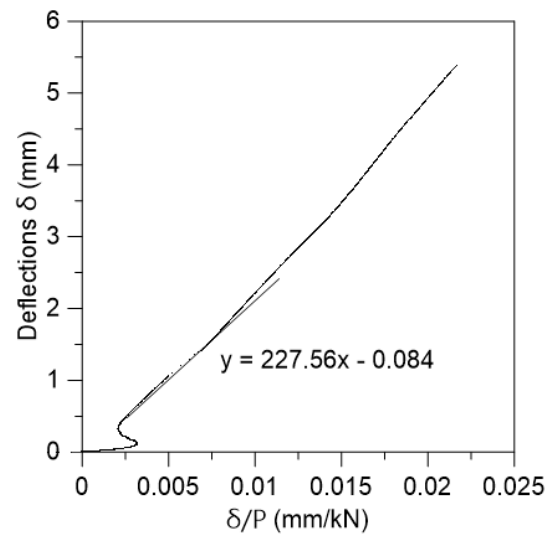
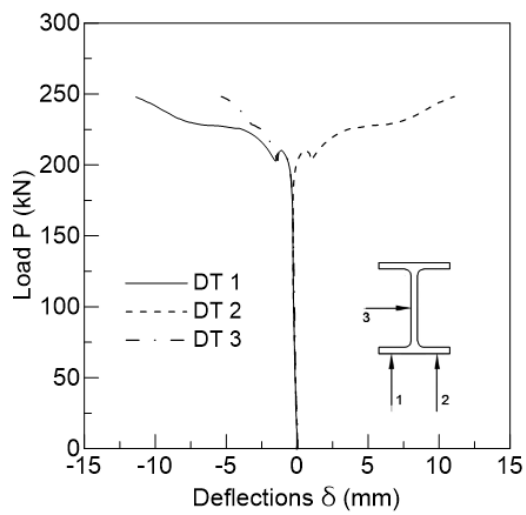
P_{cr} : 227.56 kN

P_u : 248.14 kN

Visual observations:

Local buckling observed

Failure: Crushing at web-flange
junctions



I3.E5.04.550



Date: February/2017

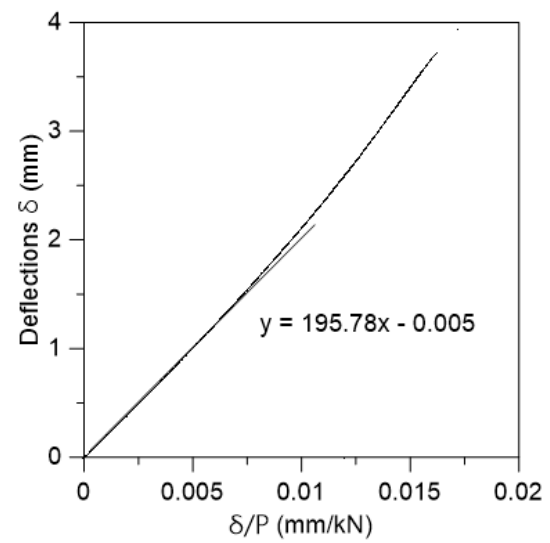
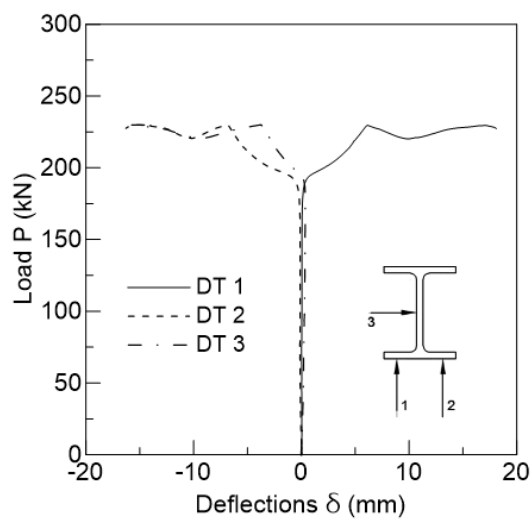
P_{cr} : 195.78 kN

P_u : 229.87 kN

Visual observations:

Local buckling observed

Failure: Crushing at the centerline
of the web



I3.E5.05.550



Date: February/2017

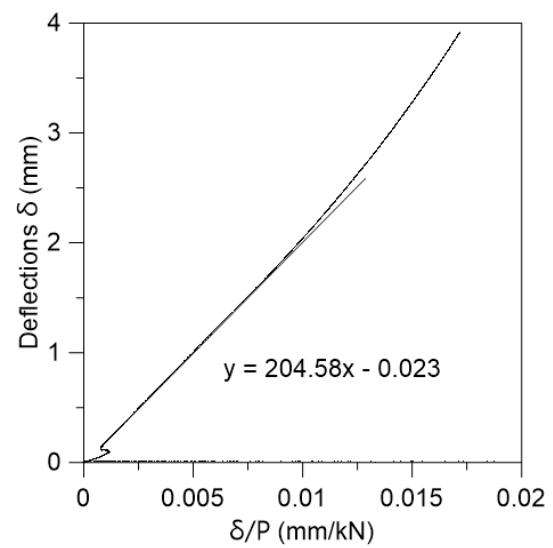
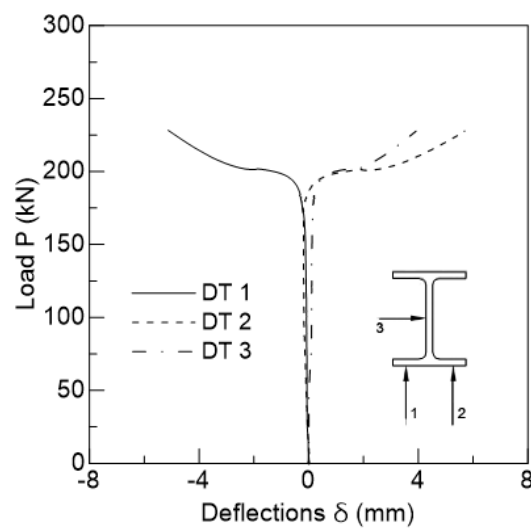
P_{cr} : 204.58 kN

P_u : 227.87 kN

Visual observations:

Local buckling observed

Failure: Crushing at web-flange
junctions



13.ES.06.550



Date: February/2017

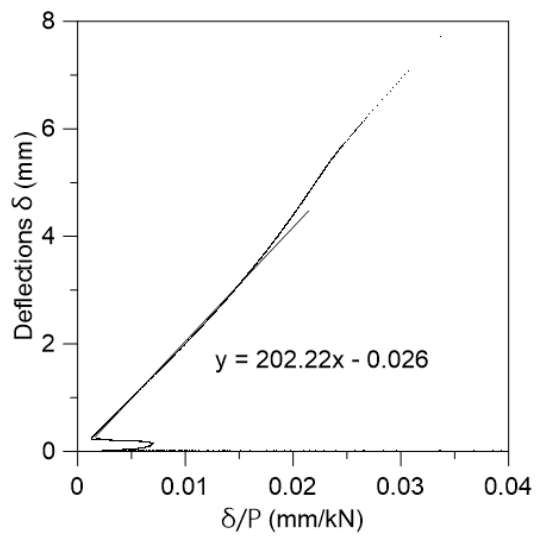
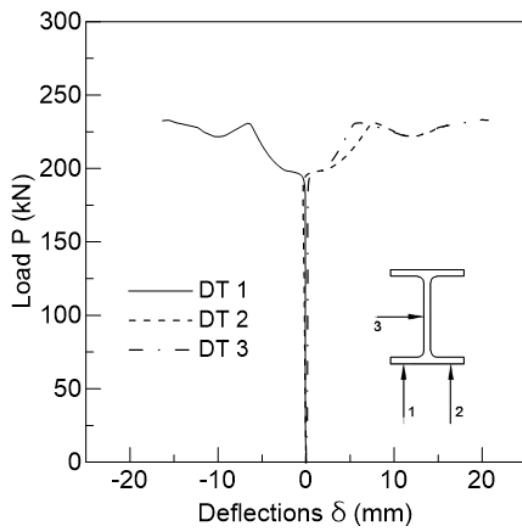
P_{cr} : 202.22 kN

P_u : 233.28 kN

Visual observations:

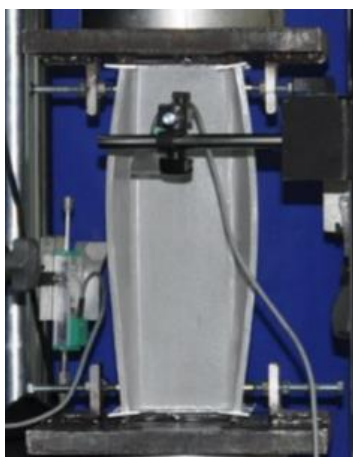
Local buckling observed

Failure: Crushing at the centerline
of the web



7.2. Simply-supported Plates

I3.ES.01.300



Date: April/2017

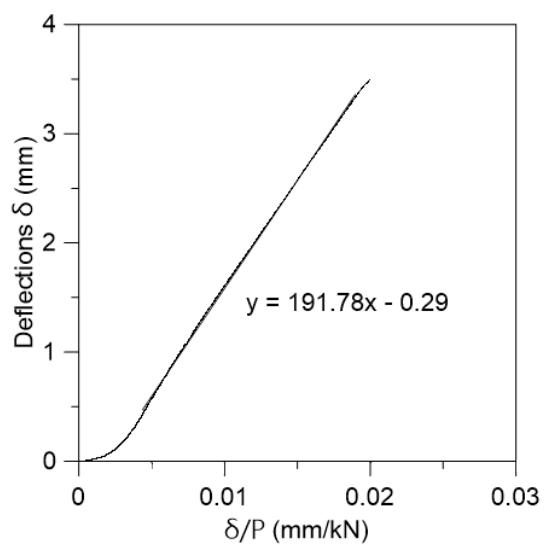
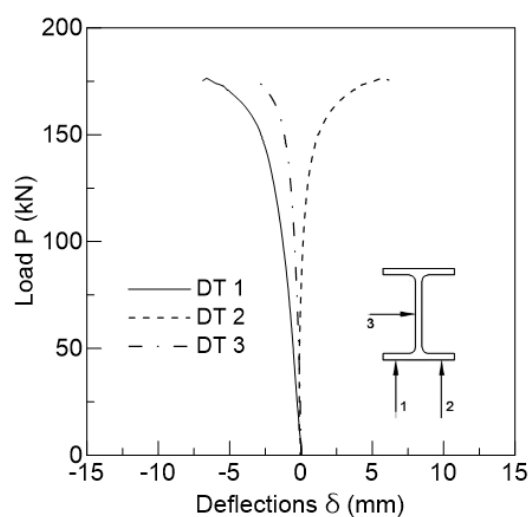
P_{cr} : 191.78 kN

P_u : 176.31 kN

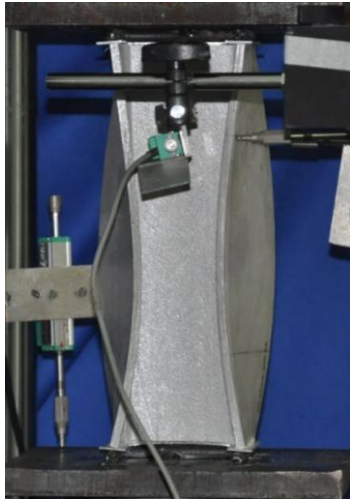
Visual observations:

Local buckling observed

The specimen slipped off the roller
axis



I3.ES.02.300



Date: March/2017

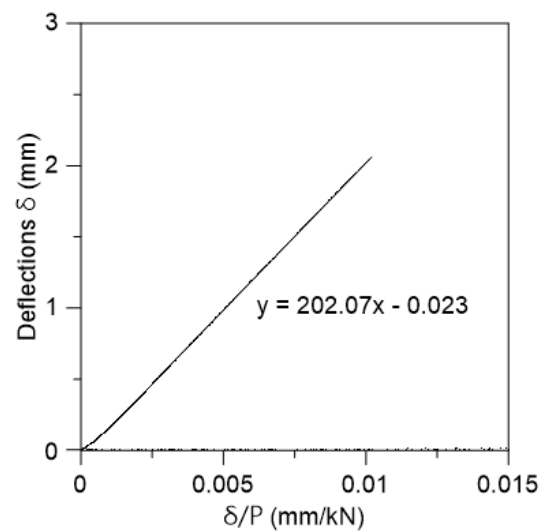
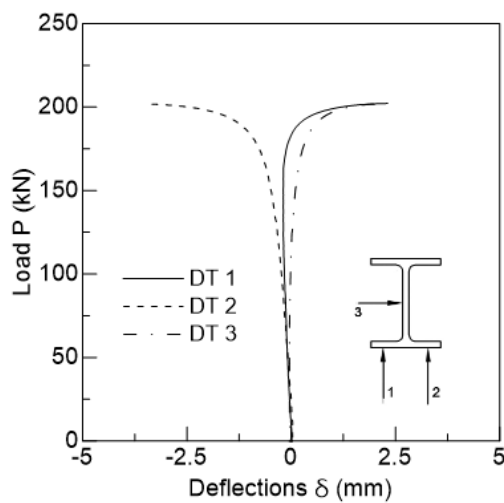
P_{cr} : 202.07 kN

P_u : 201.99 kN

Visual observations:

Local buckling observed

Failure: Crushing at web-flange
junctions



I3.ES.03.300



Date: March/2017

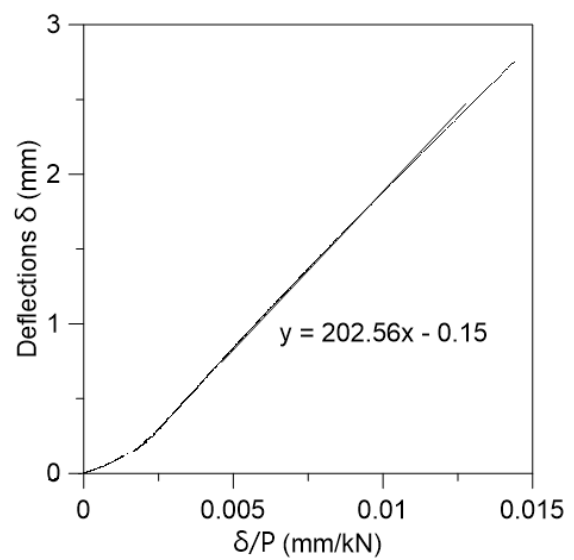
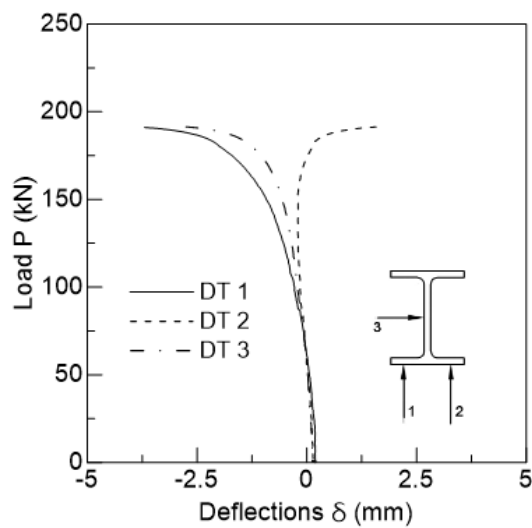
P_{cr} : 202.56 kN

P_u : 191.11 kN

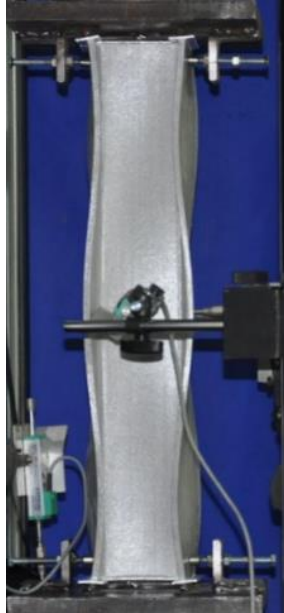
Visual observations:

Local buckling observed

Failure: Crushing at web-flange
junctions



I3.ES.04.550



Date: April/2017

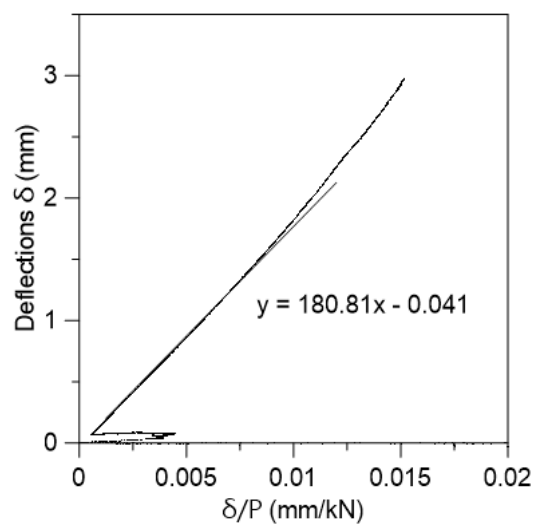
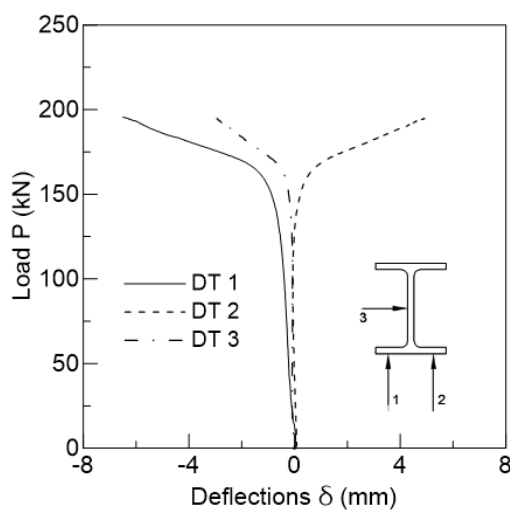
P_{cr} : 180.81 kN

P_u : 195.65 kN

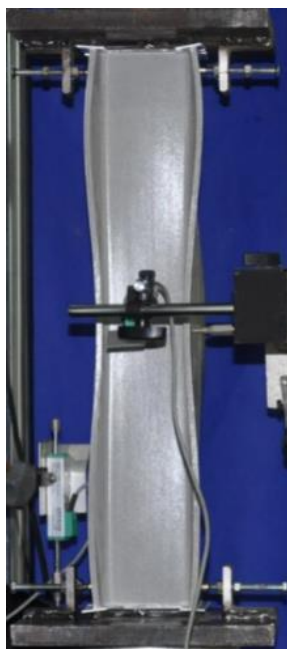
Visual observations:

Local buckling observed

The specimen slipped of the roller
axis



I3.ES.05.550



Date: April/2017

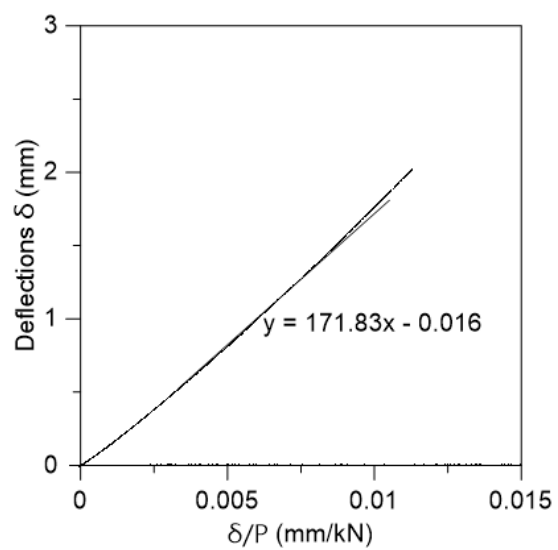
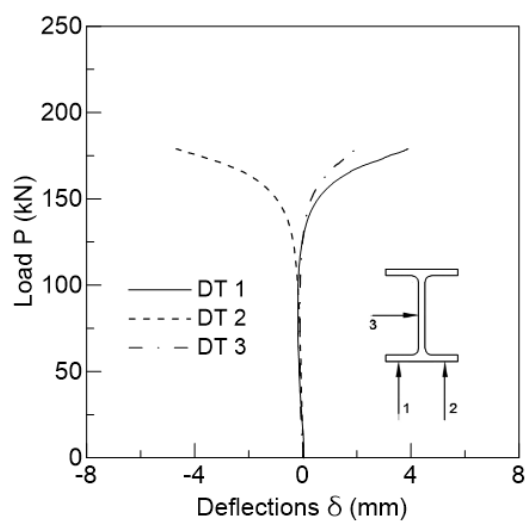
P_{cr} : 171.63 kN

P_u : 179.07 kN

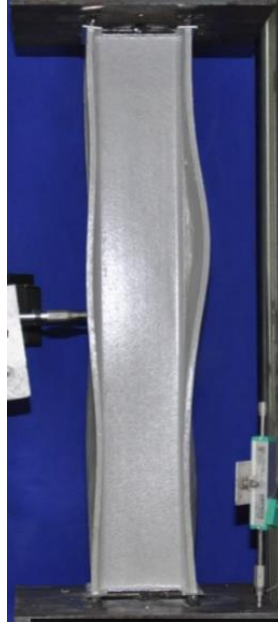
Visual observations:

Local buckling observed

The specimen slipped of the roller
axis



I3.ES.06.550



Date: April/2017

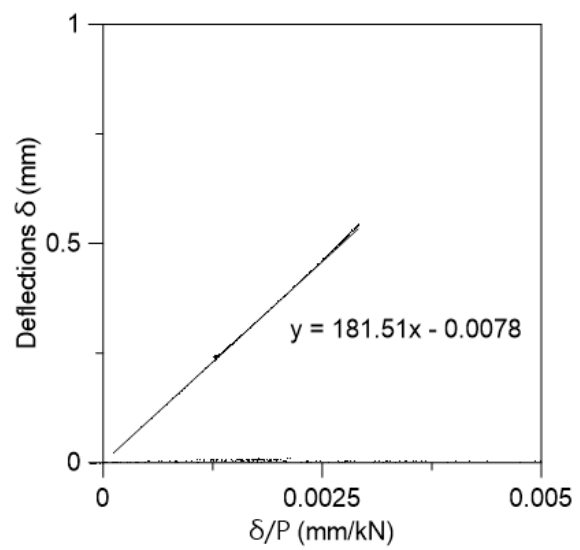
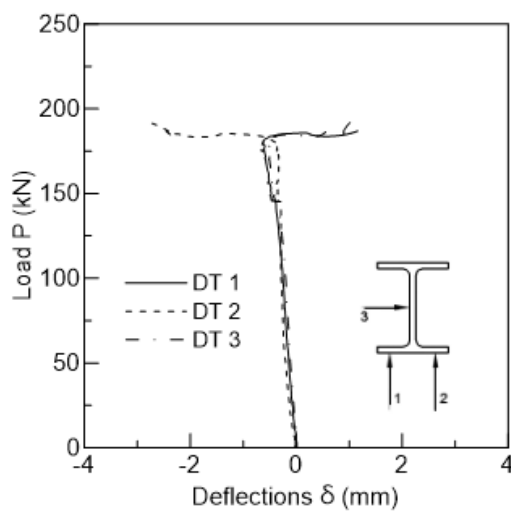
P_{cr} : 181.51 kN

P_u : 188.62 kN

Visual observations:

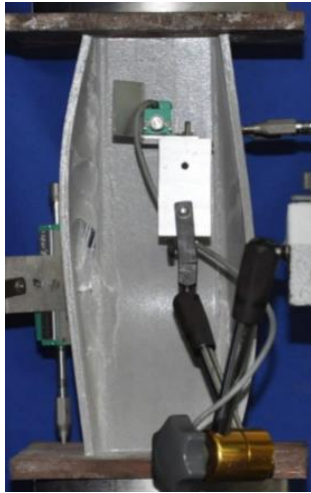
Local buckling observed

Failure: Crushing at web-flange
junctions



7.3. Plates simply in contact with base plates

I3.ES.01.300



Date: June/2017

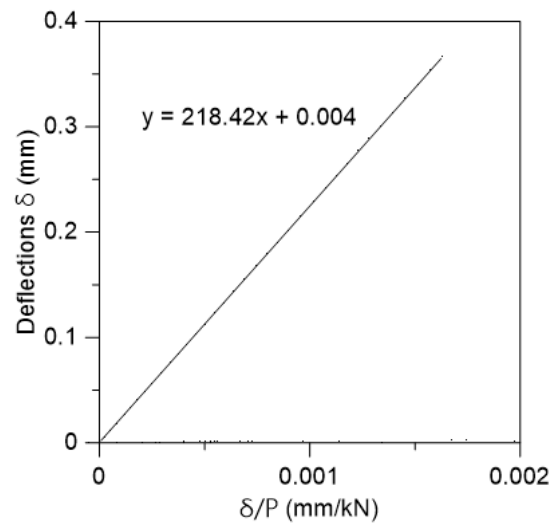
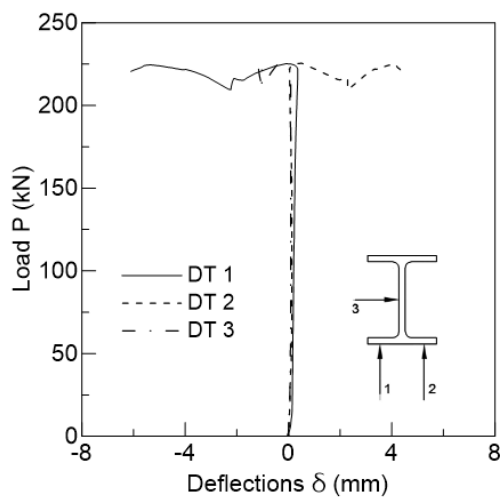
P_{cr} : 218.42 kN

P_u : 225.12 kN

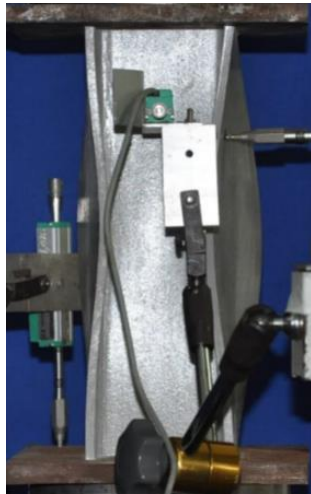
Visual observations:

Local buckling observed

Failure: Crushing at web-flange
junctions



I3.ES.02.300



Date: June/2017

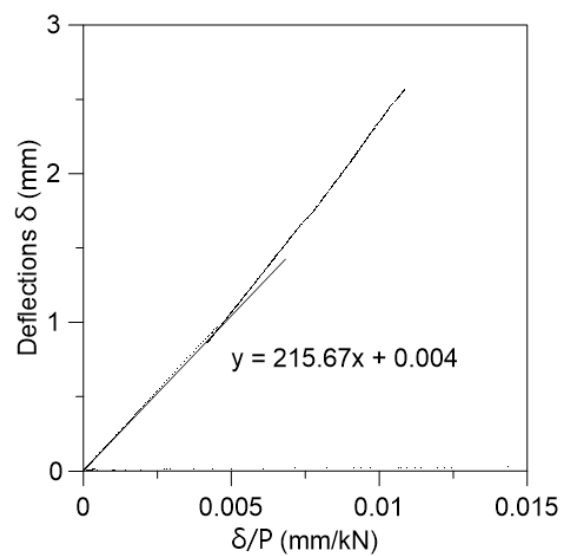
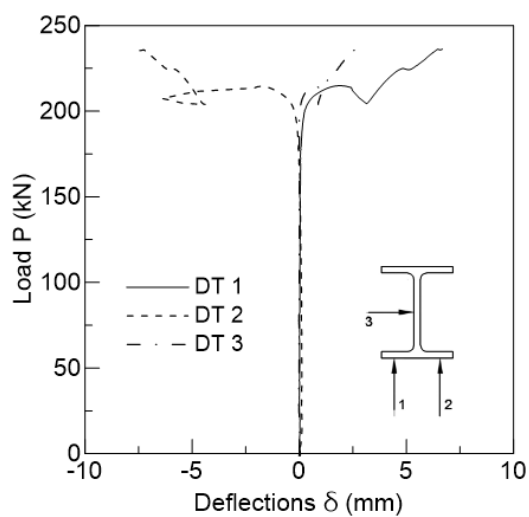
P_{cr} : 215.67 kN

P_u : 236.14 kN

Visual observations:

Local buckling observed

Failure: Crushing at web-flange
junctions



I3.ES.03.550



Date: June/2017

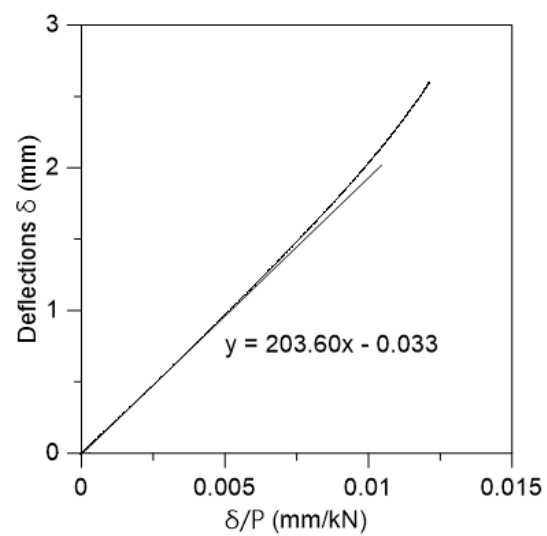
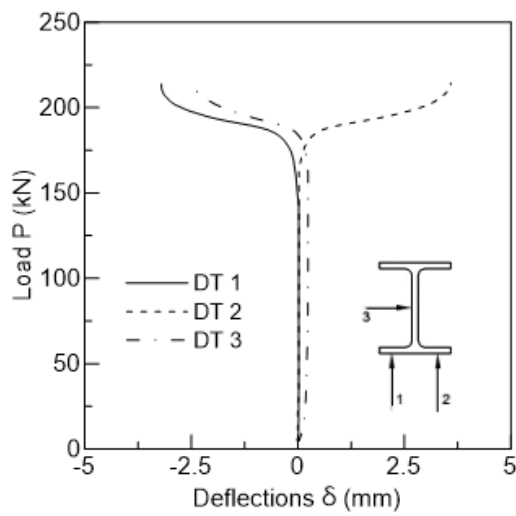
P_{cr} : 203.60 kN

P_u : 214.27 kN

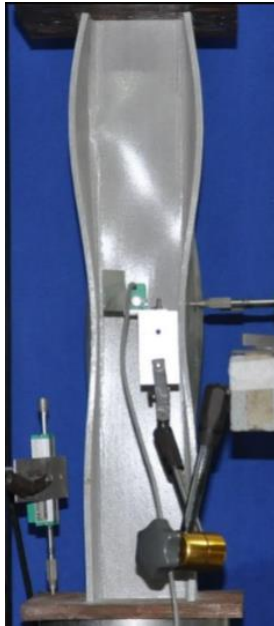
Visual observations:

Local buckling observed

Failure: Crushing at the web-flange
junction and at the web



I3.ES.04.550



Date: June/2017

P_{cr} : 191.58 kN

P_u : 214.14 kN

Visual observations:

Local buckling observed

Failure: Crushing at web-flange
junctions

